

**Subnanosecond Time-Resolved Electron Diffraction Studies
of
Short-Pulse Laser Heating in Thin Gold Films**

by
Hsiu-Cheng Chen

Submitted in Partial Fulfillment
of the
Requirements for the Degree
DOCTOR OF PHILOSOPHY

Supervised By Professor Gerard Mourou
The Institute of Optics and Laboratory for Laser Energetics
and Professor Robert Knox
Department of Physics and Astronomy and Laboratory for Laser Energetics

University of Rochester
Rochester, New York
1989

CURRICULUM VITAE

Hsiu-Cheng Chen was born in Taiwan, Republic of China in 1957. She entered National Taiwan Normal University in 1975 and began study at the Department of Physics. In 1979 she received the B.S. degree in physics. She began graduate study in the Department of Physics and Astronomy, University of Rochester, toward the Ph.D. degree in 1981. During much of her residence, she has studied under Professors Gerard Mourou and Robert Knox, who have supervised her thesis research. Her research was carried out at the Laboratory for Laser Energetics, University of Rochester, as a member of the Ultrafast Research Group. As such, she has pursued research in the ultrafast electron diffraction technique and thin metal films studies.

She received a teaching assistantship in the Department of Physics and Astronomy for the 1981-1983 academic years. From 1983 through 1989, she was a Laser Energetics Fellow. She is a member of American Physical Society.

ACKNOWLEDGEMENTS

I am greatly indebted to my thesis supervisor Dr. Gerard Mourou. His expert advice was a key element for developing my skill in ultrafast electron diffraction technology. I am also deeply grateful to Dr. Robert Knox, my departmental advisor, for his invaluable guidance and encouragement. His constant support and interest in my work has helped me a great deal in finishing my thesis and in becoming a scientist.

I would like to thank Dr. James Li in the UR Department of Mechanical Engineering, not only for his advice but also as a co-supervisor of a research grant from the Office of Naval Research which sponsored part of my thesis project.

I would also like to thank Steve Williamson for my first introduction to the ultrafast electron diffraction technique and also for being such a good colleague to work with. Thanks also go to William Donaldson, Eric Lincke, and Charlie Bamber for their valuable help in the use of ASYST; Terry Kessler, Nitin Sampat, Steve Swales, and William Castle for their helpful discussions on image analysis; and the other members of Ultrafast Research Group for many good times. A special thanks goes to James Sue for his invaluable help in every way.

I wish to thank the UR Department of Physics & Astronomy and the Laboratory for Laser Energetics for providing the necessary support, both financially and technically, and for a stimulating atmosphere and the facilities for learning. The author also would like to acknowledge financial support from a grant by the Office of Naval Research, and the University Research Initiative grant supported by the Air Force Office of Scientific Research.

ABSTRACT

An ultrafast high energy electron diffraction technique has been developed for quantitative studies. We believe that this technique has great potential in the studies of lattice dynamics, pulsed laser heating of materials, phase transitions, and surface phenomena. The electron pulse has up to 20-ps resolution permitting it to probe many transient phenomena. This technique has been applied in this thesis to investigate pulsed laser heating of 25-nm thick polycrystalline and single-crystal gold films. The time resolution of the electron probe was 100 ps in the experiment. The diffraction intensity measurement is related to the laser-induced lattice temperature via the Debye-Waller effect whereby the diffraction maxima intensities decrease because of the random thermal motion of the atoms. An initial decay observed in the measured time-resolved electron diffraction intensity indicated a temperature rise due to laser pulse heating. The temperatures obtained are in reasonably good agreement with the values calculated using a thermal diffusion model. However, the temperature profile extracted from the experimental data shows a rise time longer than that predicted by the thermal diffusion model, as well as oscillations which are wholly unexpected. We postulate that the oscillatory behavior of the scattered electron intensity is due to laser-induced surface expansion and its subsequent relaxation. We surmise that the surface expansion is associated with the generation of surface plasmons. The surface plasmon lifetime is thus found to be about 3 ns.

TABLE OF CONTENTS

	page
CURRICULUM VITAE _____	ii
ACKNOWLEDGEMENTS _____	iii
ABSTRACT _____	v
TABLE OF CONTENTS _____	vi
LIST OF FIGURES _____	x
LIST OF TABLES _____	xiii

CHAPTER

1. INTRODUCTION

1.1 Background _____	1
1.2 Transient Measurements _____	2
(a) Reflectivity, Absorption, and Transmission _____	3
(b) Raman Scattering _____	4
(c) Second Harmonic Generation _____	5
(d) Electrical Conductivity and Resistivity Measurements _____	6
(e) X-rays _____	7
(f) Electron Diffraction _____	7
1.3 The Ultrafast Electron Diffraction Probe _____	9
1.4 Comparison of Electron and X-ray Diffraction _____	16

1.5 Outline of The Thesis	19
2. EXPERIMENTS AND RESULTS	
2.1 Overview	23
2.2 The Ultrafast Electron Apparatus	24
(a) The REGEN Laser System	26
(b) The Electron Diffraction System	35
(c) Synchronization of Pump and Probe Beams	38
2.3 Steady-State Debye-Waller Effect in Thin Aluminum Films	43
2.4 Time Resolved Electron Diffraction Intensity Measurements	49
(a) Introduction	49
(b) Experimental Consideration	50
(c) Photographic Imaging Technique	53
(d) Sorting/averaging Technique	73
2.5 Summary	86
3. DISCUSSION AND INTERPRETATION	
3.1 Background Correction	88
3.2 Mechanisms of Oscillations	92
(a) Shock Waves	92

(b) Normal Mode Vibrations	93
(c) Temperature Gradients	94
(d) Surface Expansion	95
3.3 Thermal Diffusion Model	96
(a) Pulsed Laser Heating	96
(b) Temperature Conversion	104
(c) Time-Resolved Temperature Results	106
(d) The Temperature-Gradient Effect	110
3.4 Surface Expansion Model	114
3.5 Conclusion	124
References for Chapter 1	125
References for Chapter 2	133
References for Chapter 3	135

APPENDICES

A. Thin Film Preparation	137
A.1 Vacuum Evaporation Method	138
A.2 Polycrystalline Thin Films	140
A.3 Single-crystal Thin Films	141
B. Temperature Effects in Electron Diffraction	144

References for Appendix A	151
References for Appendix B	153

LIST OF FIGURES

	page
1.1 Pump-probe schematic for electron probe_____	10
1.2 Schematic representation of the temperature effect on diffraction intensities_____	14
2.1 Ultrafast electron diffraction apparatus_____	25
2.2 Wavelength range and temperature dependence of harmonic-generation crystals_____	27
2.3 Regenerative (REGEN) laser system_____	28
2.4 Beam radius dependence on the YAG-rod position_____	30
2.5 Streak-camera trace of the REGEN output pulse_____	32
2.6 Q-switched mode-locked pulse (V-curve) of REGEN laser _____	34
2.7 Yield spectrum of gold film_____	36
2.8 Response of microchannel plates_____	39
2.9 Spectral response of P-47 phosphor_____	40
2.10 Synchronization of electron probe by electron beam deflection _____	42
2.11 Steady state Debye-Waller experimental setup_____	44
2.12 Chart recorder output of steady state Debye-Waller experiment_____	46
2.13 Temperature dependence of electron diffraction intensities of polycrystalline Al_____	48
2.14 Block diagram of digital image analysis_____	54
2.15 D - log I calibration curve_____	57
2.16 Digitized electron diffraction ring patterns_____	59
2.17 Circularly averaged electron diffraction ring patterns_____	61

2.18	Comparison of lineouts with and without digital signal processing.....	63
2.19	Electron diffraction maxima intensity change under pulsed laser irradiation.....	65
2.20	Electron diffraction image of a single-crystal Au film.....	67
2.21	Lineouts of a single-crystal Au film with and without laser heating.....	68
2.22	Time-resolved electron diffraction intensity of Au(220) using image analysis.....	70
2.23	Time-resolved electron diffraction intensity of Au(331) using image analysis.....	71
2.24	Time-resolved electron diffraction intensity of Au(331) using image analysis for a different sample.....	72
2.25	A histogram of the REGEN output energy.....	76
2.26	Intensity relationship of REGEN pulse and its frequency-quadrupled UV pulse.....	77
2.27	Relationship of REGEN pulse intensities and corresponding electron diffraction signals.....	78,79
2.28	Experimental arrangement using sorting/averaging.....	81
2.29	Flow chart of computer data acquisition procedure.....	83
2.30	Time-resolved electron diffraction intensity of Au(220).....	84
3.1	Lineout used for background correction.....	90
3.2	Background-corrected results of those in Fig. 2.30.....	91
3.3	Computer simulation of laser-induced temperature profiles.....	102
3.4	Computer simulation of temperature gradient.....	103

3.5	Temperature profile obtained from the electron diffraction intensity measurements for heating irradiance P_1 _____	107
3.6	Temperature profile obtained from the electron diffraction intensity measurements for heating irradiance P_2 _____	108
3.7	Temperature profile obtained from the electron diffraction intensity measurements for heating irradiance P_3 _____	109
3.8	Computer simulation of electron diffraction intensity in the presence of temperature gradients_____	113
3.9	Comparison of calculated and experimental electron diffraction intensity _____	115
3.10	Computer simulation of oscillations in electron diffraction intensity with surface expansion model for heating irradiance P_1 _____	120
3.11	Computer simulation of oscillations in electron diffraction intensity with surface expansion model for heating irradiance P_2 _____	121
3.12	Computer simulation of oscillations in electron diffraction intensity with surface expansion model for heating irradiance P_3 _____	122

CHAPTER 1

INTRODUCTION

1.1 BACKGROUND

The gradual transition of materials research from an almost purely technological basis to a combination of basic science and applied materials research has been accelerated by recent developments in experimental research tools and techniques. Because of developments in devices and techniques for materials studies, such as the optical microscope, X-ray and neutron diffraction, the electron microscope and, more recently, the high energy pulsed laser and the scanning electron microscope, fundamentals concerning thermodynamics, solid-state physics, and quantum mechanics of materials are now accessible to study and have become increasingly interesting to physicists, chemists and materials scientists. In recent years, laser technology has been one of the driving forces behind this basic transition, and future developments in lasers are expected to continue this trend. Because of the unique spatial and temporal properties of the laser, laser processing of materials has been an important and active research area since the beginning. Some topics of current interest are laser annealing¹⁻⁴ and quenching,⁵⁻⁶ laser surface processing⁷⁻⁸ of materials, such as

martensitic hardening,⁹ melting/recrystallization,¹⁰⁻¹¹ alloying,¹²⁻¹⁴ and cladding.¹⁵ A more fundamental note, interest in the dynamics of laser-material coupling has prompted intense studies¹⁶⁻²¹ regarding the mechanisms involved in materials processing with lasers. This interaction results in changes in the optical and thermodynamic properties of the materials. From optical reflectance²²⁻²⁷ and transmittance²⁸⁻²⁹ measurements under laser irradiation, the nature of energy transfer processes can be revealed, and measurements of laser-induced temperature rise can be used to determine the dominant effects in coupling mechanisms.

1.2 TRANSIENT MEASUREMENTS

Time-resolved experimental techniques have proved to be indispensable tools for the study of laser-material interactions. It is now possible to explore transient phenomena more thoroughly since the development of short pulsed lasers. The time-resolved probes developed are now so fast that fine detail in the fundamental mechanisms of laser-material interactions can be resolved and complex theoretical models can be devised. One of the main goals of the present work is to develop and demonstrate a new investigative tool based on a time-resolved transmission electron probe, which we believe has useful aspects which complement other time-resolved techniques. Before describing our method, it is worthwhile to discuss the more commonly-used time-resolved probes.

(a) Reflectivity, absorption and transmission

The sensitivity of the optical properties of materials to laser irradiation³⁰ makes an optical probe suitable for time-resolving the mechanisms of laser-material interactions. In metals, the transmissivity is relatively low due to its strong absorption coefficient and so reflectivity and absorptance measurements are more common. The change in optical properties is a window to processes induced by pulsed laser irradiation. Electron-phonon energy transfer processes in Si were investigated by using femtosecond reflectivity measurements²⁵ and a triple pulse scheme.²⁹ The metallic state of molten Si can be clearly distinguished in reflectance measurements since its absorptance and reflectance increase dramatically from those of crystalline Si. Anomalous surface transformations were observed³¹ under subpicosecond laser pulse irradiation by reflectivity measurements. The results indicate that melting occurred, followed by rapid resolidification forming an amorphous ring. This was an important investigation in surface morphology.³²⁻³⁵

Despite its wide use, there is one aspect of transient reflectivity measurements that is not well understood; the reflectivity curves do not converge for various laser power densities at long delay times.³⁷ Nevertheless, this probe is commonly used in time-resolved measurements because it reveals directly the energy transfer processes. Electron and/or lattice temperatures and melt depths, however, can be determined only indirectly, in contrast with the direct determination by other high-penetration

methods, such as X-ray³⁸⁻⁴⁰ and high energy electron diffraction.⁴¹⁻⁴²

Reflectivity measurements are not used in studies of crystalline structure.

(b) Raman scattering

Lattice temperatures can be determined from Raman spectra by measuring the position and the width of the optical-phonon line and the Stokes-to-anti-Stokes intensity ratio of Raman scattering.⁴³ The position and width of the optical-phonon line of a Raman spectrum undergoes a sharp shift which is dependent on lattice temperature. However, Raman scattering measurements have been controversial because of difficulties in intensity calibration. Consequently, earlier experimental work which conflicted with the generally accepted thermal diffusion model of laser-material interactions did not find full acceptance until Compaan⁴⁴ and Wartmann⁴⁵ reinterpreted the data in light of two significant points. First, the factor $C_R(T)$ of Stokes-to-anti-Stokes intensity ratio $S_R(T)$ was revised significantly where $S_R(T)$ can be expressed as

$$S_R(T) = C_R(T) \exp(\hbar \omega / k_B T) \quad 1.1$$

where \hbar and k_B are Planck's constant and Boltzmann's constant, respectively.

The value of the temperature dependent $C_R(T)$ was not well-known until recently.⁴⁴⁻⁴⁶ Wartmann et al.^{45,48} estimated the lattice temperature rise to

be as high as 1400 K which was in agreement with thermal diffusion model.

The second point is that the Raman scattering efficiency decreases strongly

with temperature so the lattice temperature could be underestimated unless a high time-resolution Raman probe were used.

This technique is particularly important in surface studies. Raman scattering can be enhanced due to laser-induced surface asymmetry as in the case of second-harmonic generation on the surface.⁴⁹ This optical probe is applied extensively in investigations of surface chemical processes. We note, however, that the Raman results can be complicated by other emission processes so extreme care needs to be taken in interpreting the results.

(c) Second-harmonic generation (SHG)

It has been demonstrated that SHG component in reflection signals⁵⁰ from media with inversion symmetry can be used to investigate the dynamics of structural changes. The orientation dependence of reflected SHG signals from Si⁵¹ and Ge⁵² was observed. SHG is a nonlinear probe which has been used to settle some ambiguous questions raised by linear optical probes on whether the thermal diffusion model or the plasma model correctly explains the laser annealing process. It was used to study the recrystallization process on the surface of gallium arsenide⁵³ following laser irradiation. A low SHG efficiency initially was observed, and it was suggested that the subsequent strong increase in SHG efficiency indicated recovery of the noncentrosymmetric lattice by liquid epitaxial growth following a melt. The conclusion was then reached that the thermal diffusion model correctly describes the annealing process. Like the Raman scattering process, SHG is

also used in surface studies.⁴⁹ A surface temperature measurement based on the SHG effect on a Ag(110) was monitored with a picosecond probe pulse. The second harmonic intensity for incident fundamental light (628 nm) decreased dramatically when the crystal temperature was raised. The transient temperature rise induced by the laser pulse, a nanosecond-duration infrared pulse, agreed with a thermal diffusion model simulation.

(d) Electrical conductivity and resistivity measurements

The electrical conductivity or resistivity undergoes changes when a phase transition occurs. Thus, melting and recrystallization kinetics can be studied in detail by monitoring the electrical resistivity as a function of laser fluence. Both metals and semiconductors are suitable targets of study by this technique, but metals show a far less dramatic response than semiconductors. A direct measurement of liquid/solid interface kinetics of Al⁵⁴ and Si⁵⁵ during melting has been reported by this transient probe. The electron temperature can be estimated from the electrical resistivity of a metal by applying simple Drude's electron theory. Results from using this technique indicated that the electron temperature can be raised to 10^6 K in near-solid density Al under irradiation by a 400 fs laser pulse.⁵⁶ Baglin et al.⁵⁷ have reported using conductivity measurements in amorphous Si to determine whether annealing produced by pulsed ion heating depends on high density electronic excitation. Using two different pulsed ion beams, energy was deposited principally to the lattice in one case and as electronic excitations in the other. The results for

melting time were the same, leading to the conclusion that equilibrium of electronic and vibrational states is fast compared to phase changes in the material and that electronic excitations are unimportant in annealing.

(e) X-ray

X-rays, in general, are a probe for bulk structural studies. Nanosecond-resolution time-resolved X-ray diffraction has been used to measure liquid-solid interface overheating and undercooling in Si³⁸ and in Ge³⁹ during pulsed laser irradiation. The temperature profile of the material can be determined from the measurement of the width and shape of the Bragg peaks. The rocking curves caused by thermal expansion is indicative of an increase in lattice parameters near the liquid-solid interface. Reflective steady-state X-ray diffraction of a surface, however, was used to investigate melting of a lead surface.⁵⁸ A much lower melting point for the lead surface was observed. Laser-induced strain and electronic structural change were monitored by X-ray absorption spectra.⁴⁰

X-ray probing is a direct measurement of structure and temperature. The temperature determination is based on the Debye-Waller effect wherein the diffraction intensity is reduced during a temperature rise according to an exponential Debye-Waller factor.

(f) Electron diffraction

The principle of the electron diffraction probe is similar to that of the

X-ray probe. Because of the availability of short wavelengths, the electron diffraction technique is capable of revealing structural information on an atomic scale. In addition, the short-time resolution enables the study of pulsed laser interaction with material on a nanosecond or picosecond time scale. Nanosecond low energy electron diffraction (LEED)⁵⁹ is an ideal probe for surface melting and heating because of its small extinction depth, but its low scattering efficiency is a disadvantage. However, a medium or high energy electron operating in reflective mode (RHEED)⁶⁰⁻⁶¹ can provide higher scattering efficiency than LEED. Although surface structure studies in molecular beam epitaxy (MBE) growth has been done, but to the author's knowledge, there is no time-resolved results reported using this method. With all electron diffraction techniques, the lattice temperature can be determined through intensity measurements by utilizing the Debye-Waller effect. A major difference between electron and X-ray diffraction is that electrons interact with atoms much more strongly than do photons. This makes electron diffraction better suited for thin film and surface studies. However, one should note that problems remain in the interpretation of electron diffraction images because of multiple scattering processes.

The use of time-resolved electron diffraction to study ultrafast dynamics is a fairly recent development. In 1982, a picosecond electron diffraction technique⁴¹ was reported for the first time. It showed that picosecond electron diffraction (using 25 keV electrons) can be used to time-resolve the laser-induced melting process⁴¹⁻⁴² in thin aluminum films. The time taken for

the disappearance of the electron diffraction patterns allowed the melting time to be inferred. This showed that it is possible to melt the aluminum in a time as short as 20 ps if sufficient laser fluence is applied. Other true structural probes, such as X-rays and LEED, thus far demonstrated are limited to a nanosecond time scale. A subpicosecond probe based on second harmonic generation,⁵¹ which is structure dependent, can give only indirect structural information. The time-resolved probes such as electrical conductivity,⁵⁶⁻⁵⁷ optical probes for transmission⁶²⁻⁶³ and reflection²⁴⁻²⁵ measurements, nonlinear optical probes based on Raman scattering,^{44,48} and time of flight mass spectrometry,⁶⁴ have time resolution as short as femoseconds in some cases; however, they do not provide structural information in general. It has been suggested⁴¹⁻⁴² that among the time-resolved structural probes, the ultrafast (picosecond to subpicosecond) electron probe can produce unambiguous structural information of thin metal films.

1.3 THE ULTRAFAST ELECTRON DIFFRACTION PROBE

We now briefly discuss the ultrafast electron probe and describe how the data obtained using this technique may be analyzed. The basic principle of the ultrafast electron probe is illustrated in Fig. 1.1. An optical pump pulse is directed at the sample, which is subsequently probed with an subnanosecond electron pulse synchronized with the pump pulse. In our experimental apparatus, the electron pulse is produced through the photoelectric effect by a synchronized UV laser pulse on a gold photocathode.

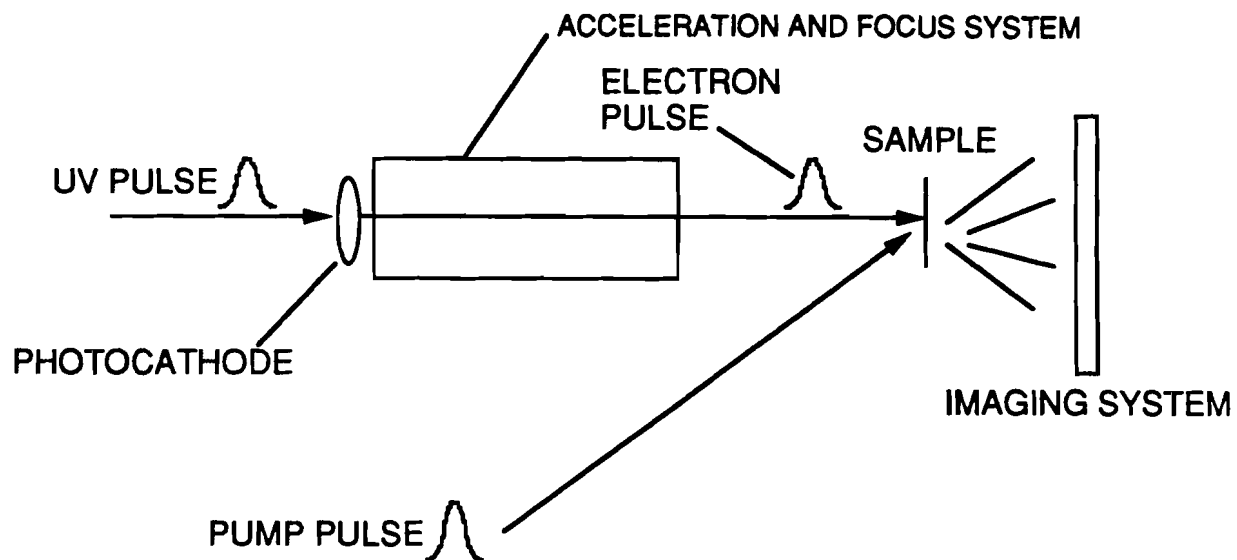


Fig. 1.1 Schematic of an ultrafast pump-probe experiment with an electron probe.

The time resolution of the electron pulse is limited to the duration of the laser pulse. The non-relativistic de Broglie wavelength of the electrons is 0.0768 Å, corresponding to an operating voltage of 25.5 kV. The relativistic correction is about 1%. The size of the focused electron beam is 250 to 400 μm in diameter. The diffraction pattern is amplified by two-stage microchannel plates and imaged onto a fast phosphor screen. Measurements of the diffraction intensities of a particular order may then be performed using any of several photodetectors. The phosphor had a relaxation time of several hundred nanoseconds. Note that the phosphor relaxation time has no connection with the resolution achieved by the electron probe pulse. With available pulsed lasers, picosecond resolution should be ultimately attainable for the electron probe. Quantitative ultrafast time-resolved measurements of diffraction intensities have not been performed previously.

The measured time-resolved electron diffraction intensities are directly correlated with the lattice dynamics of the sample. This allows us to observe laser-induced microstructural and temperature changes in the sample on a picosecond time scale by monitoring either the decrease in electron diffraction intensity (the Debye-Waller effect) or the contraction of diffraction maxima spacing due to expansion of the lattice with higher temperatures. We have found in practice that changes in the diffraction maxima intensities provide an easier and more sensitive measurement compared to changes in the diffraction maxima spacing. The relation between the temperature and the

diffraction intensity is given in a first approximation by the Debye-Waller theory.

According to Debye-Waller theory, a direct relationship between the lattice temperature of the sample and the electron diffraction maxima intensity can be established. The temperature factor was first derived by Debye⁶⁵ and the theory was later refined by Waller⁶⁶ and Faxen.⁶⁷ According to these theories, the intensity of the diffraction maxima decreases with the increasing lattice temperature as $\exp [-2M(T)]$, where

$$M = B (\sin^2 \theta_{hkl} / \lambda^2) \quad 1.2(a)$$

and

$$B = (6 h^2 / m k_B \Theta) [D(x) / x + 1/4] \quad 1.2(b)$$

Here Θ is Debye temperature, $x = \Theta/T$, m is the mass of the atom, h and k_B are Planck's constant and Boltzmann's constant, respectively, θ_{hkl} is the Bragg angle for each plane (hkl) , and λ is the wavelength of the electrons. The interplanar spacing d_{hkl} for the diffracting plane (hkl) of a cubic system can be written as

$$d_{hkl} = a / (h^2 + k^2 + l^2)^{1/2} \quad 1.3$$

where h , k , l are the Miller indices, and a is the lattice constant. $D(x)$ is the Debye function⁶⁸ given by the expression

$$D(x) = \frac{1}{x} \int_0^x \frac{x'}{\exp(x') - 1} dx' . \quad 1.4$$

As the lattice temperature is raised and the melting point of the material is approached the diffraction maxima become progressively broader and of lower intensity and finally merge with the background. The lattice temperature can be extracted from electron diffraction intensity measurements. The portion of the intensity of the diffraction maxima that is lost in the Debye-Waller effect shows up in the thermal diffuse background because of energy conservation. Figure 1.2 illustrates the features of the electron diffraction intensity that the theory predicts, including the background thermal diffuse scattering (TDS), as a function of scattering angle. The monotonic background is that predicted by the Debye theory. In experiment, the TDS is not uniform and is found to be stronger around the diffraction maxima. Later work by Faxen⁶⁷ predicted the shape of the TDS and did not change Debye's expression for the intensity of the diffraction maxima.

There have been a number of studies on the Debye-Waller factor in various materials. Lattice vibrations in aluminum single crystals⁶⁹ have been studied at various temperatures from 100 to 300 K, showing the temperature dependence of X-ray diffraction. By observing the (h 0 0) reflections of Al, they used the temperature derivative of the Debye-Waller factor dM/dT to determine the Debye characteristic temperature Θ . Various X-ray diffraction results⁶⁹⁻⁷⁵ in several metals were analyzed theoretically by Gupta⁷⁶ using an anharmonic correction to the Debye theory. Electron diffraction techniques has been used to study steady-state temperature-dependent dynamical theory

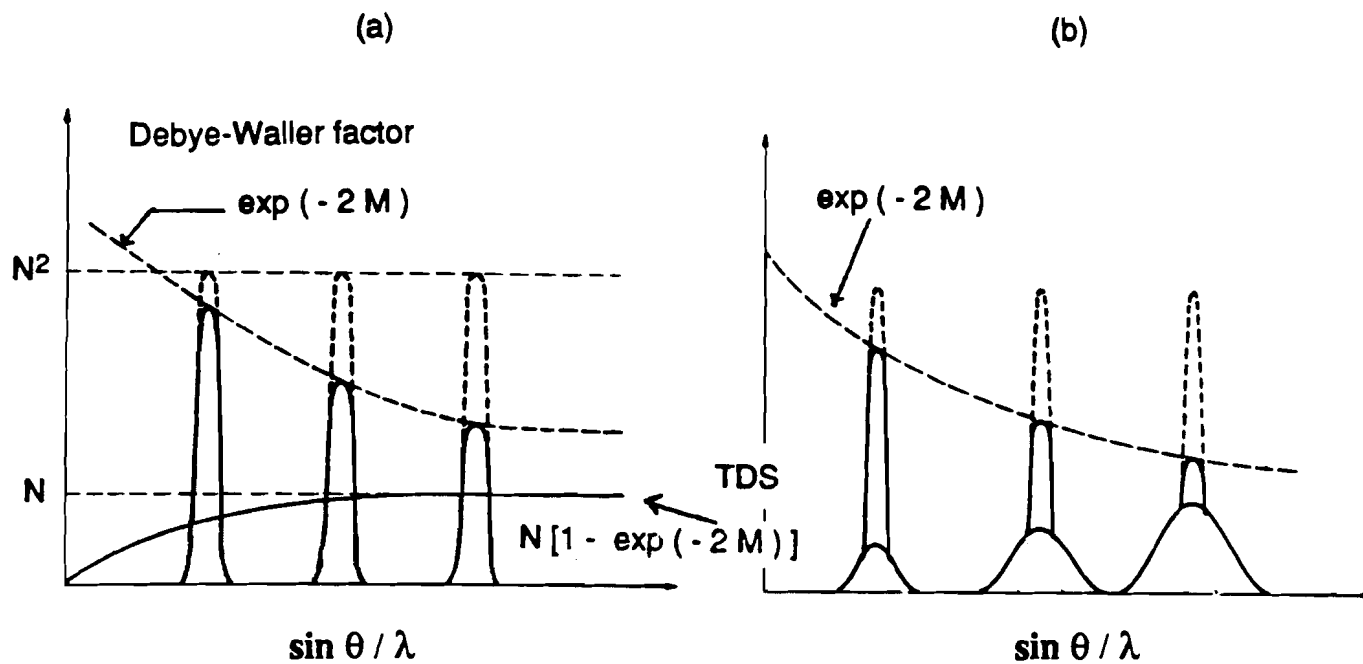


Fig. 1.2 Schematic representation of the temperature effect on the diffraction intensity according to (a) the simple Debye theory and (b) after Faxen's correction. (After L. Azaroff, Elements of X-ray Crystallography, McGraw-Hill, 1968.)

of diffraction in polycrystals⁷⁷⁻⁷⁹ and in the surface atoms of single crystals.⁸⁰ The temperature dependence of high energy electron diffraction intensities in metals has been investigated by several research groups. Some looked at the size effect,⁸¹⁻⁸⁴ that is, large surface vibrational amplitudes significantly alter the Debye-Waller effect in small particles. Anharmonicity⁸⁵ at very high temperature was also investigated by high energy (50 keV) electrons. A strong decrease in the intensity of the low-energy electron diffraction patterns from the surface of nickel⁸⁰ and gold⁸⁶ crystals as the temperature of the crystal increases has been observed. The strong temperature dependence corresponding to a large Debye-Waller effect arises from larger surface vibrational amplitudes.

The simple kinematic Debye-Waller theory holds only when the sample is thin enough to neglect interactions among the scattered waves. As the mean crystal size increases, dynamical considerations grow more important because of the multiple scattering processes caused by the relatively strong electron scattering by the atoms of the crystal. The dynamical effect is particularly significant in electron diffraction because of stronger coupling between the electrons and the material. The apparent absorption^{78,87-90} arising from such dynamical processes can alter the temperature dependence of diffraction intensity considerably. The steady-state high energy electron diffraction was used to study the strong temperature dependence in the intensities of the primary beam and low-order reflections for thick crystals, which can only be explained by the dynamical theory.⁹¹⁻⁹⁴

In time-resolved work, surface structural changes of a Ge(111) crystal during pulsed laser annealing have been measured using nanosecond time-resolved low energy electron diffraction (LEED).⁵⁹ LEED is both structure and surface (depth about 10 Å) sensitive. The results revealed a rapid liquid layer formation and subsequent surface recrystallization and cooling. In our work, we have investigated the laser-induced heating process of thin films on a subnanosecond time scale by transmission electron diffraction.

1.4 COMPARISON OF ELECTRON AND X-RAY DIFFRACTION

The ultrafast electron probe is basically a surface and structural probe with unique characteristics that should enable it to become a valuable investigative tool. The other common structural probe is X-ray, but there are major differences between the two in terms of pulse duration, wavelength, scattering probability, and absorption.

The fast electron beam can be produced on a picosecond time scale easily using a picosecond laser. The development of ultrafast pulsed lasers has made it possible to produce picosecond electrons via the photoelectric effect.⁹⁵⁻⁹⁶ The fastest pulsed X-ray source³⁸ developed to date is of nanosecond duration and was produced at the Cornell High Energy Synchrotron Source.

The range of electron wavelengths available is wider compared to that of X-rays (Duane-Hunt short-wavelength limit) for commonly used operating

voltages. It can be ten times shorter than that of X-rays given the same operating voltage. The major significance of shorter wavelength is greater resolving power. The expression with relativistic correction for the electron wavelength is

$$\lambda (\text{\AA}) = h / \sigma \sqrt{2m_0eV} \quad , \quad 1.5$$

where m_0 is the electron rest mass, e is the electron charge, h is Planck's constant, c is the speed of light, V is the operating voltage, and $\sigma = [1+(eV/2m_0c^2)]^{1/2}$ is the relativistic correction factor. For $V < 50$ kV, this can be approximated by the non-relativistic expression ($\sigma \approx 1$)

$$\lambda (\text{\AA}) = (150 / V)^{1/2}. \quad 1.6$$

There is a 2% relativistic correction in wavelength for $V = 50$ kV and 10% for $V = 200$ kV. The X-ray wavelength produced by a tube with operating voltage V is calculated using the relation

$$\lambda (\text{\AA}) = (hc / eV) = 12399 / V. \quad 1.7$$

For comparison, the wavelengths of electrons and X-rays are listed in Table 1.1 for various operating voltages.

Electrons are negatively charged and are sensitive to the electric fields belonging to both the nucleus and the atomic electrons and so the atomic scattering factor $f_e(\theta)$ is proportional to $[Z - f_x(\theta)]$, where Z is the atomic

Table 1.1 The wavelengths of electrons, calculated without and with relativistic corrections, and of X-rays for various operating voltages. The correction factor σ is defined on p. 17.

V (kV)	electron wavelength		σ (%)	X-ray wavelength (Å)
	nonrelativistic (Å)	relativistic (Å)		
1.0	0.3873	0.3871	0.05	12.4
5.0	0.1732	0.1728	0.24	2.48
10	0.1225	0.1219	0.48	1.24
15	0.1000	0.0993	0.72	0.83
20	0.0867	0.0859	0.96	0.62
25	0.0775	0.0766	1.2	0.50
30	0.0707	0.0697	1.4	0.41
40	0.0612	0.0601	1.9	0.31
50	0.0548	0.0535	2.4	0.25
60	0.0500	0.0486	2.8	0.21
70	0.0463	0.0448	3.2	0.18
80	0.0433	0.0418	3.7	0.16
90	0.0408	0.0391	4.1	0.14
100	0.0387	0.0370	4.6	0.12
125	0.0346	0.0327	5.6	0.10
150	0.0316	0.0295	6.6	0.08
175	0.0293	0.0271	7.6	0.07
200	0.0274	0.0250	8.5	0.06
300	0.0224	0.0197	12	0.04
500	0.0173	0.0142	19	0.03

number and $f_x(\theta)$ is the atomic X-ray scattering factor. $|f_e(\theta)|^2$ and $|f_x(\theta)|^2$ are the scattering cross sections at angle θ for electrons and X-rays, respectively. However, the scattering of X-rays is produced indirectly by atomic electrons accelerated through interactions with the incident field and so the scattering factor $f_x(\theta)$ depends only on the electron density distribution. The strong interaction of electrons with materials results in an electron atomic scattering factor that is much larger than that of X-rays, $f_e(\theta) \sim 10^4 f_x(\theta)$. This sometimes results in multiple electron scattering and increases the complexity of scattering processes, making the interpretation of electron diffraction patterns more difficult.

Electrons are absorbed much more readily than are X-rays. At very low voltages, electrons are adsorbed on the first monolayer on the crystal surface allowing the study of surface structure and dynamics. Finally on a more practical note, ultrafast electron pulses can be generated readily in a wide range of wavelengths using standard laboratory equipment. High energy (~ 10 MeV) short wavelength X-rays, by contrast, require large and expensive electron accelerators.

1.5 OUTLINE OF THE THESIS

In this thesis, the ultrafast electron diffraction technique is shown to be feasible and is established as a time-resolved structure probe. Through

careful signal-to-noise enhancement procedures for the electron diffraction intensity measurements, a quantitative study of laser-induced temperature rise in thin films was completed. A 100-ps, high-intensity, and high-repetition-rate regenerative Nd:YAG laser system was used in the ultrafast electron diffraction technique. An operating repetition rate of up to 1 kHz permitted us to use signal averaging, which is essential to the experiment.

In Chapter 2, the features and the operation of the ultrafast electron diffraction apparatus and the regenerative laser system are described and the procedure for the synchronization of the optical pump and electron probe pulses is explained. Experimental results obtained are then given. Steady-state temperature measurements by the electron diffraction technique to investigate the Debye-Waller effect in thin aluminum films are presented first. The time-resolved measurements consist of two parts in which different measurement techniques are used. In the first part, digital image analysis is applied to a photographic image of the diffraction pattern to enhance the signal-to-noise ratio and to extract information. Experimental results on both polycrystalline and single-crystal gold films are presented. In the second part, a technique using a boxcar averager that is interfaced to a personal computer is described. The computer is also used to control the experiment and computer sorting of the data allows the reduction of noise and error due to laser fluctuations. Extensive and detailed measurements of the time-resolved (220)-order diffraction intensity of single-crystal gold films are obtained. The two measurement techniques are complementary; the digital image analysis

method is better suited for the analysis of global features of the diffraction pattern whereas the boxcar technique is ideal for the observation of specific features. An unexpected finding of the experiment is an oscillatory behavior in time of the intensity of the diffraction maxima. The observed oscillations were superimposed on the monotonic Debye-Waller curve and are not predicted by theory. This behavior was observed with both measurement techniques.

The interpretation of our time-resolved experimental results and their implications are discussed in Chapter 3. A computer simulation of the lattice temperature rise based on the one-dimensional heat diffusion equation is described. The theoretical predictions of the thermal diffusion model are compared with experiment. There is good agreement, but the temperature rise in the experiment is slower than that predicted by the model. The thermal diffusion model is unable also to explain the oscillations in the diffraction intensity. Several possible mechanisms for this oscillatory behavior are then explored. As a result of our investigations, we propose a surface expansion model to explain the oscillations. The expansion of the surface is postulated to arise as a result of laser-induced surface plasmon generation. We surmise that the subsequent relaxation of the surface atoms to their equilibrium positions is responsible for the observed oscillations. We have done a computer simulation of the surface expansion model and have obtained reasonably good qualitative agreement.

Finally, in Appendix A, a detailed description of the preparation of the gold and aluminum samples is given. In Appendix B, some limitations and extensions of the Debye-Waller theory are discussed.

CHAPTER 2

EXPERIMENTS AND RESULTS

2.1 OVERVIEW

In this chapter, we describe in detail an ultrafast electron probe that we have developed and show some results obtained using this instrument in a pump-probe experiment. The quantitative investigation of lattice vibrations in thin metal films under stimulation by short intense laser pulse irradiation is a major goal in our work. We have investigated 25 nm thick single-crystal and polycrystalline Au films under pulsed laser irradiation and have obtained time-resolved measurements of the diffraction intensity with 100 picosecond resolution using this ultrafast time-resolved electron probe. To the author's knowledge, this is the first time such results have been obtained. The basic mechanism relating the diffraction intensity of the electron probe to the sample temperature is described by the Debye-Waller theory, which shows that the intensities of the diffraction maxima decrease with increasing lattice temperature.¹⁻² As the lattice temperature is raised and the atomic vibrational amplitudes increase, the intensity of the diffraction maxima decreases.

In Section 2.2 we describe the ultrafast electron diffraction apparatus and the pump-probe experimental arrangement. We present in Section 2.3

some time-resolved intensity measurements on Au film using two different techniques, a photographic imaging technique suited for studying global characteristics of diffraction patterns such as thermal diffuse scattering distributions, and a technique employing a personal computer interfaced with a boxcar that is best suited for investigating specific features of the diffraction pattern. In addition, computer control allows us to reduce certain sources of noise. We also include some steady-state measurements of the Debye-Waller effect in 25 nm thick polycrystalline Al film. Finally, in the last section we present some conclusions.

2.2 THE ULTRAFAST ELECTRON APPARATUS

The experimental setup for the ultrafast electron probe is illustrated in Fig. 2.1. A high repetition-rate regenerative laser system (REGEN)³⁻⁴ is used to generate both the infrared (IR) pump pulse and the electron probe pulse. The IR pulse of the REGEN laser was collimated and spatially filtered with a 100 μm pinhole. This attenuates the laser power by about 10 percent, but the spatial profile of the pulse is considerably improved by this procedure. The spatially filtered 1064-nm REGEN laser pulse entering from the bottom in Fig. 2.1 is frequency-doubled by a KDP (potassium dihydrogen phosphate) crystal and is then split by the dichroic mirror (DM) into two pulses. The SHG efficiency of KDP is approximately 25%. The dichroic mirror DM allows up to 98 percent of the frequency-doubled (2ω) pulse to be transmitted and 100

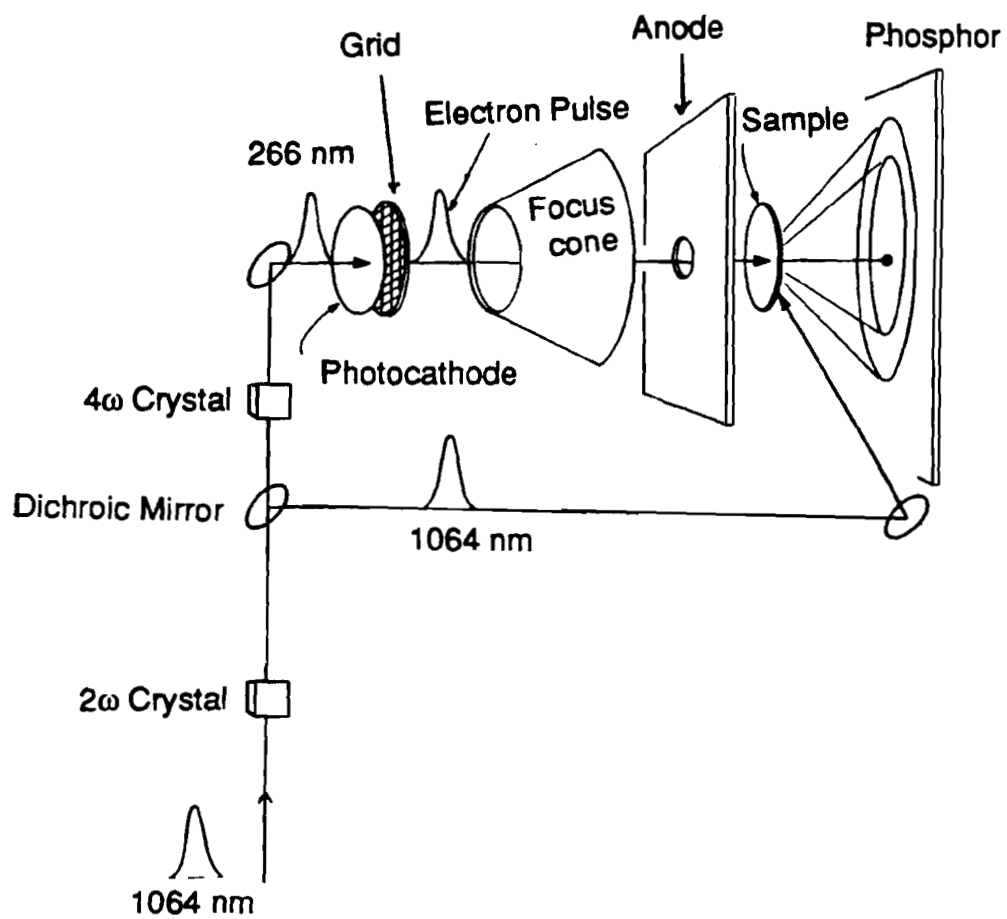


Fig. 2.1 Schematic of experimental apparatus for an ultrafast electron probe.

percent of the infrared pulse (ω) to be reflected. The reflected beam (ω) after passing through an adjustable optical delay line (not shown in diagram) is employed to heat the sample. The transmitted frequency-doubled pulse (2ω) is frequency-doubled again by a temperature-controlled ADP (ammonium dihydrogen phosphate) crystal to produce an ultraviolet 266 -nm optical pulse (4ω) in order to generate primary electrons through the photoelectric effect. The temperature of the ADP crystal was set at 50 C. The frequency conversion curve as a function of crystal temperature for the harmonic crystals is provided by the manufacturer and is shown in Fig. 2.2.

The two major components of the experimental apparatus are the REGEN laser system and the electron diffraction system. A small but important accessory component is a device specially constructed in order to synchronize the IR pump and electron probe beams. In the rest of this section, we describe these components and their operation in detail.

(a) The REGEN laser system

The REGEN³⁻⁴ laser system was recently developed at the Laboratory for Laser Energetics, University of Rochester. The high-repetition-rate (as high as 1.5 kHz), 1 mJ/pulse, and 100-ps REGEN laser was an essential part of the pump-probe experiment because of signal-averaging requirements. A schematic of the configuration of the laser is shown in Fig. 2.3. The laser system is comprised of two lasers, the CW mode-locked Nd:YAG oscillator

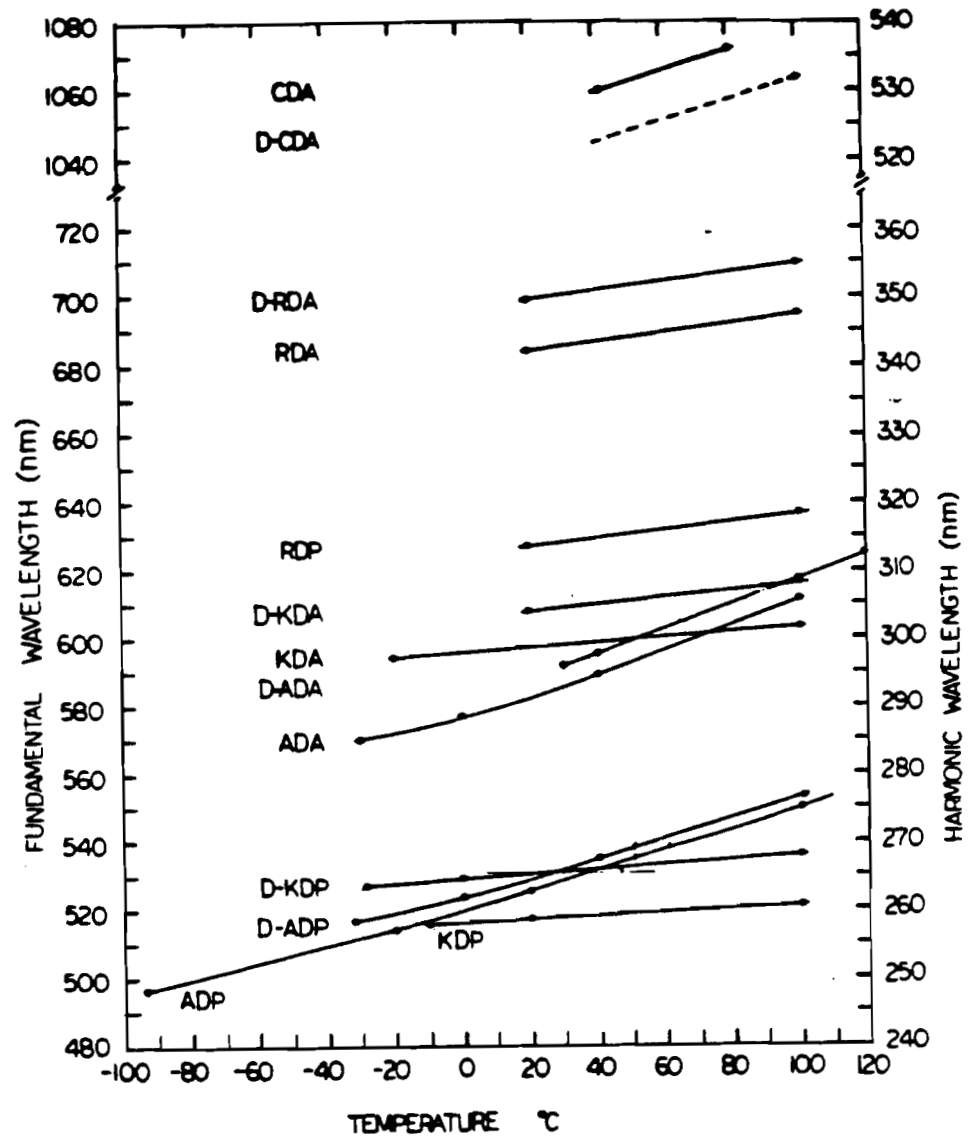


Fig. 2.2 Wavelength range and temperature dependence of various nonlinear crystals used in second harmonic generation. (After a data sheet from Quantum Technology, Inc.)

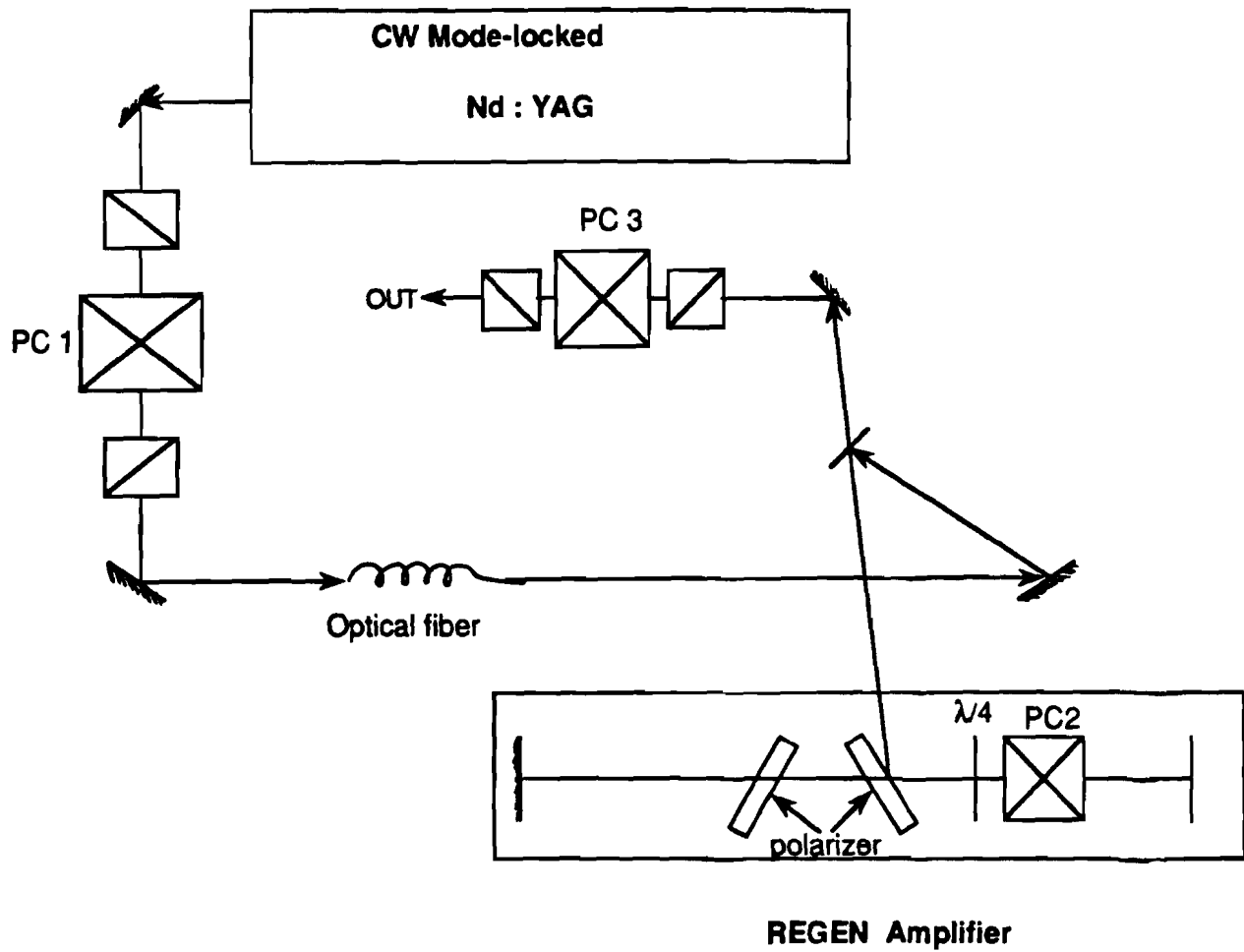


Fig. 2.3 Schematic the regenerative (REGEN) laser system. PC1 and PC3 are external switchouts, and PC2 is the REGEN cavity Pockels cell.

and the Nd:YAG regenerative amplifier. An optical fiber transports the output pulses from the oscillator to the amplifier. The use of a fiber not only decouples the alignment of the two lasers but also allows them to be in different locations without the need for long beam paths.

A CW, mode-locked Nd:YAG laser is used as the oscillator. The YAG rod, 40 mm in diameter, is placed at a distance of about 45 cm measured from its center to the 12% flat cavity mirror (output coupler). This distance is determined by the thermal lensing effect of the YAG rod for an operating current of about 34 amperes. A graph of gaussian beam radius vs. the distance for this rod is shown in Fig. 2.4. The gaussian radius of the optical beam is defined as the distance between 10% and 90% of measured beam intensity and is measured by scanning a razor blade across the beam. The acoustic-optic mode-locker is an anti-reflection coated quartz crystal. A frequency synthesizer supplies a 50 MHz signal with amplitude of 1 V peak-to-peak for both of the radio-frequency (RF) amplifier and the Pockels-cell drivers. The split signal for the RF amplifier, however, was attenuated in order to obtain the required output power for the mode-locker. Normally, an RF power of 4-6 W is used. If the cooling of mode-locker is sufficient, a maximum power of 8 W may be applied. The mode-locker should be adjusted to be at Bragg's angle so that the laser power is close to zero or at the minimum before the RF signal is applied to it. The RF frequency needs some adjustment in order to optimize the output power of the laser pulse. At this point, the reflection of RF power should be zero. The mode-locked pulse

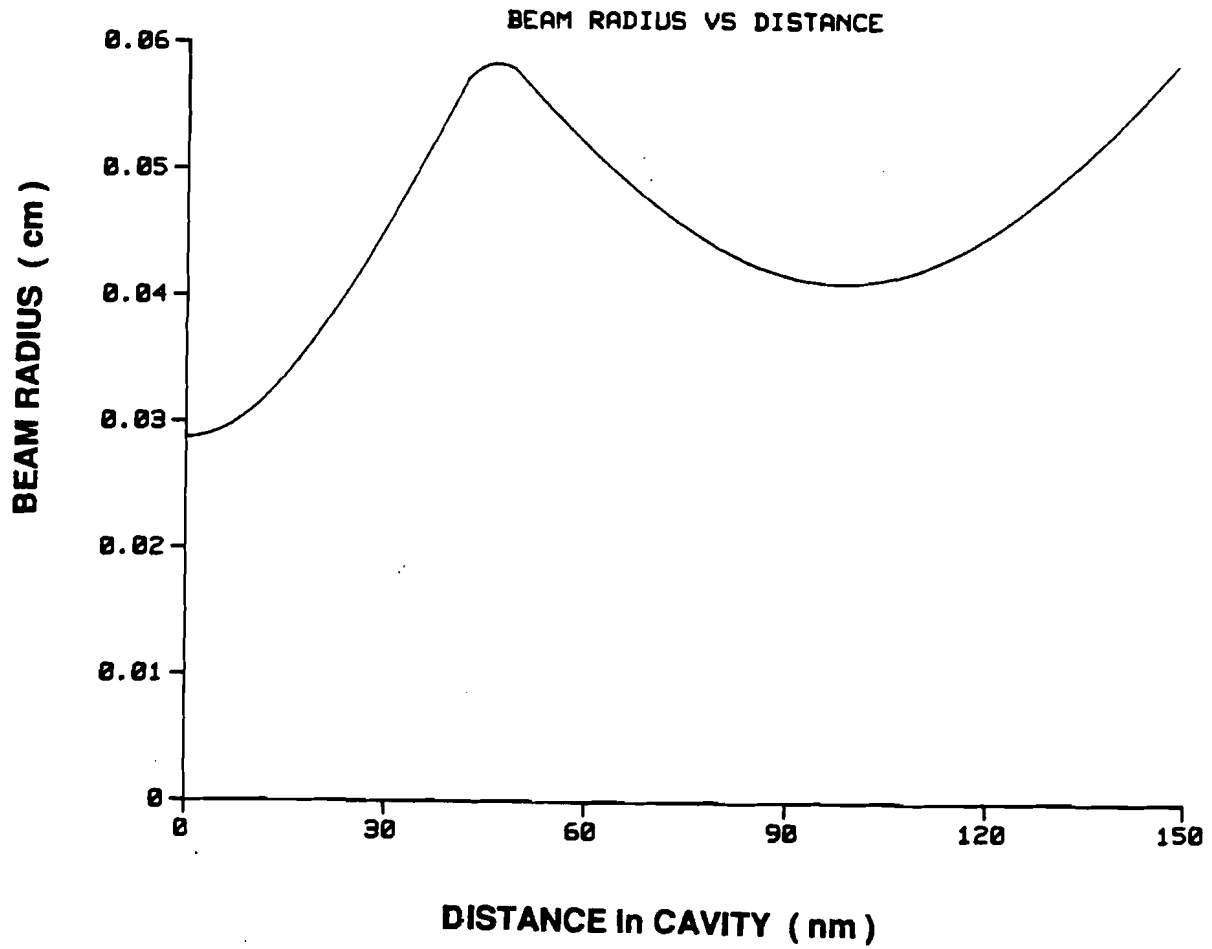


Fig. 2.4 Beam radius as a function of cavity distance. The center of the YAG rod is placed at the position where the maximum radius occurs (45 cm).

train can be monitored by a streak camera which is controlled by an optical multichannel analyzer (OMA). This procedure was used to determine the pulse width and to fine-tune the cavity in order to obtain the maximum laser power and yet retain stability. The physical cavity length was 145 cm, slightly less than the 150 cm optical cavity length. The normal CW laser output power was 5-10 W with a 12% output coupler. The output of the oscillator has a 100 ps pulse duration with a repetition rate of 100 MHz. A 4% reflector was used to pick up a portion of this mode-locked pulse train for injection into the fiber.

An optical switch-out (PC1), made of LiNbO₃ crystal, was used to preselect only one pulse from the CW mode-locked pulses for injection into the fiber. This significantly improved the Q-switching efficiency. In Fig. 2.5, the difference in the intensity of the REGEN output pulse, with and without using the switch-out, is shown. If the whole pulse train is injected, interference among the pulses can reduce the Q-switching efficiency greatly. The interference arises from the difference in the cavity lengths of the two lasers, the oscillator and amplifier. The injected pulse energy was about 10 pJ. The fiber was 9 μm in diameter and a few meters in length, although a longer fiber may be used if a shorter injection pulse (optical fiber pulse compression) is desired.

A second CW Nd:YAG laser was used as the amplifier and was tuned to have a CW lasing power of about 3-4 W measured with a 12 percent output

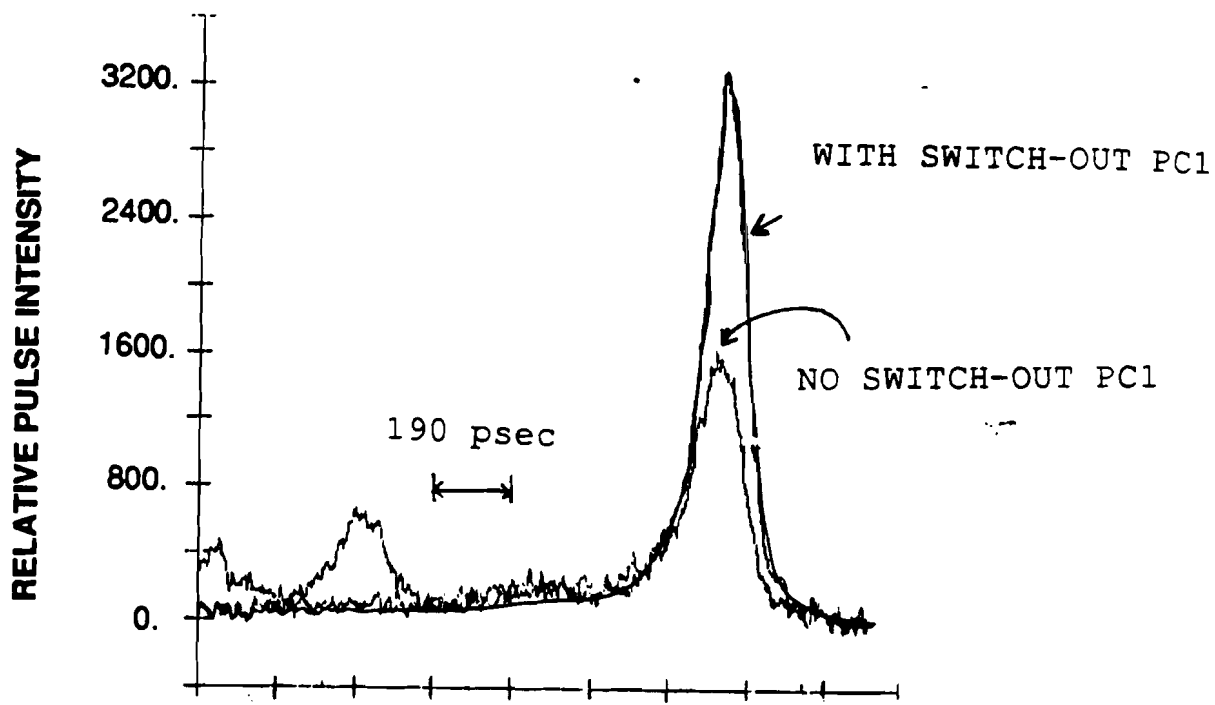


Fig. 2.5 Streak camera trace of the REGEN laser pulse with switch-out and without switch-out. The pulse width is about 120 ps. The pre-pulses are from the trace without the use of the switch-out.

coupler. A quarter-wave plate was placed in this laser cavity both to frustrate CW lasing and to reject the injected pulse after two round trips. A LiNbO_3 crystal was placed in the cavity to serve as the Q-switching and cavity-dumping Pockels cell PC2. The Pockels cell was driven by a driver supplying a fast two-step electrical pulse. The size of the first step is about 2.5 kV in order to produce a quarter-wave rotation to compensate for the quarter-wave plate in the cavity. The Pockels cell not only acts as a Q-switching device but also traps the injected pulse in the laser cavity. The pulse train is Q-switched and mode-locked as shown in the V-curve in Fig. 2.6. At approximately 500 ns (about 45 round-trip passes) later, the second electrical pulse triggers PC2 to cavity-dump the strongest pulse of the mode-locked giant pulse train (Q-switched). The optimum output of REGEN amplifier with a 100% reflector is a 100-ps duration pulse with an energy of 1 mJ. The REGEN amplifier can be triggered at any repetition rate up to 1.6 kHz which is a limitation due to the Pockels cell driver power supply. However, in our experiment the typical operating repetition rate was 1 kHz, the maximum rate at which the pulse energy remains constant since it was found that energy roll-off occurs at higher repetition rates.⁴ The output pulse of the REGEN laser was preceded by pre-pulses separated by about 1-2 ns which were not completely blocked by Q-switching. Therefore, a second switch-out PC3 (KDP) was placed after the ejection of the REGEN amplifier pulse to block such pre-pulses. It should be noted that some of the experiments in this work were performed with a longer pulse duration, about 250 ps, because of

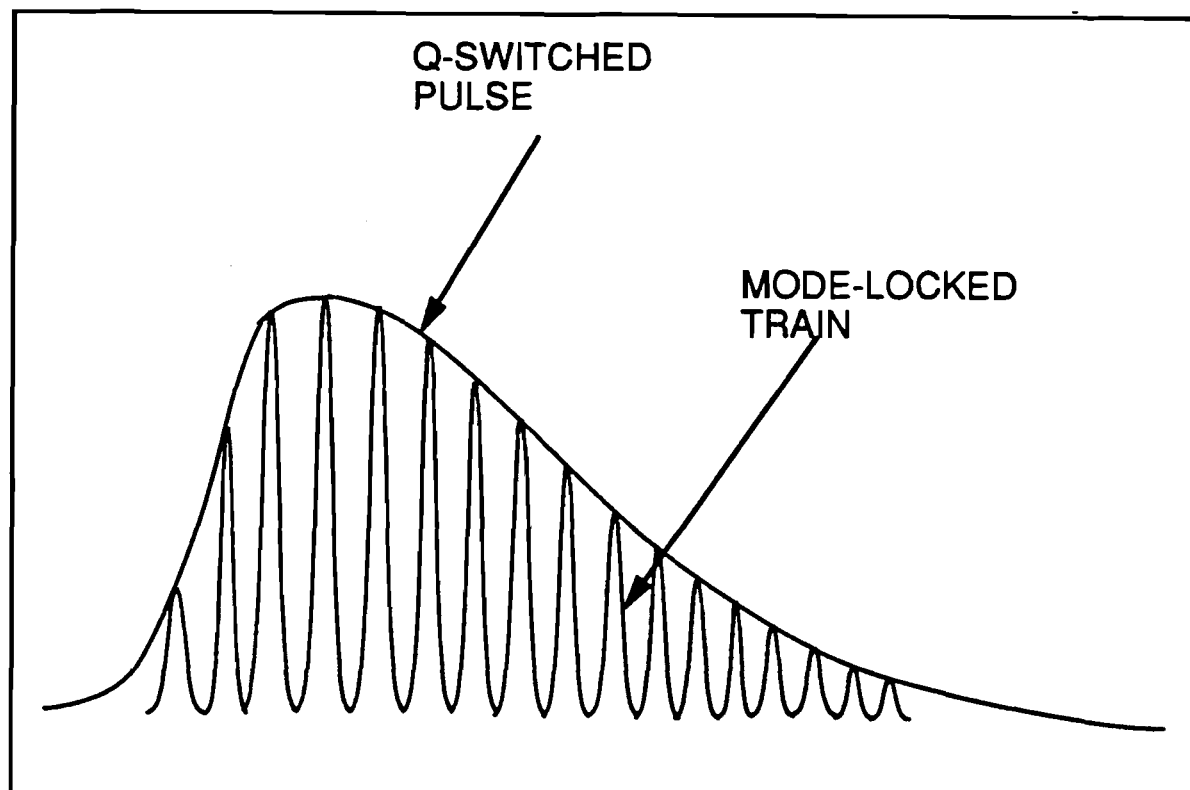


Fig. 2.6 Mode-locked train enveloped by the giant Q-switched pulse which has a rapid risetime and a relatively long tail.

greater maintenance difficulties of the laser system when shorter pulses are used.

(b) The electron diffraction system.

The electron diffraction instrument consists of an electron emitter, a focussing and deflection system to control the electron beam, and an image forming system.

The front end of a streak camera tube was converted into an electron probe-forming system.⁸ The tube contains a photocathode, an extraction grid, a focus cone, deflection plates, and the image forming assembly. The photocathode was made by vapor-deposition of 250Å-thick gold film onto a quartz or sapphire substrate. The work function of Au is 4.8 eV. The quantum efficiency of Au is 10^{-4} for photon energies above 3.0 eV. A yield spectrum⁵ of evaporated gold film is shown in Fig. 2.7. The photoelectric effect is relatively clean and is capable of providing an extremely short and well-formed electron pulse that is a replica of the optical pulse. The frequency-quadrupled 266 nm UV pulse matches the work function of the gold photocathode and produces the primary electrons. The lifetime of the photocathode was typically 100 hours due to laser damage in our experiment.

An extraction grid with a pinhole approximately 250µm to 350µm in diameter was placed immediately after the photocathode, about 1 mm from the Au film of the photocathode, in order to reduce the energy-spread of the

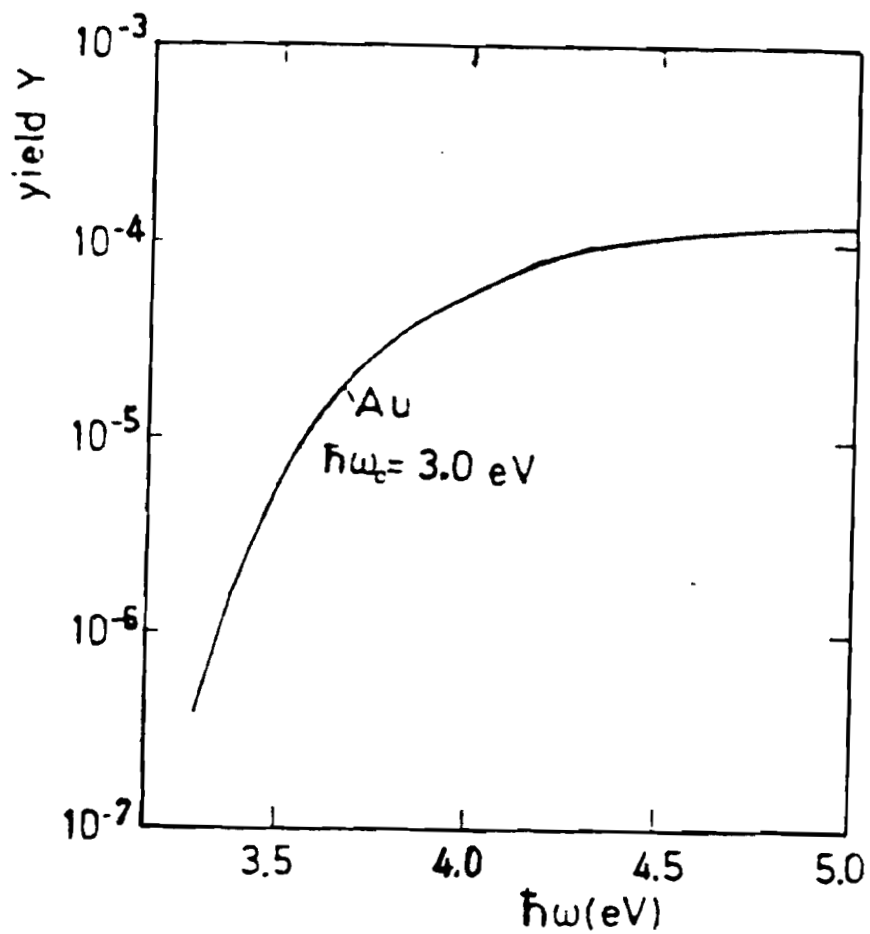


Fig. 2.7 The yield spectrum of evaporated gold film. The threshold energy is 3 eV.

electrons. A negative potential was applied to the photocathode and the grid to accelerate the electrons to an energy of 25.5 keV through the focus cone. The nonrelativistic de Broglie wavelength of the electrons is 0.07680 Å for an operating voltage of -25.5 kV (the relativistic correction to the wavelength at this energy is about 1%). The spatial resolution of electron beam can be as small as 100 μm. In our experiment, the electron beam was 250 μm to 400 μm in diameter.

A set of electron deflection plates for x- and y-direction are placed right after the anode for positioning the electron beam on the specimen. In the course of the experiment, surface charge can build up on any ungrounded or insulating components to the extent that the electron beam path is changed. A Faraday cage is placed around the electron beam path in order to prevent the shift of the electron beam on the sample.

The image forming system consists of a two-stage microchannel plates (MCP) and phosphor assembly. The MCP can be used to amplify the electron signal with a maximum amplification of 10^4 . The RCA P-47 ultrafast phosphor screen that was used has a relaxation time of several hundred nanoseconds. The phosphor coating is on the inner surface of a fiber-optic faceplate. The faceplate provides a one-to-one image of electron diffraction pattern. This MCP and phosphor assembly is mounted on a vacuum flange for attaching directly to the vacuum chamber. The spatial resolution of the MCP is 10 μm, which is the size of each element. The response of the electron intensity

measured as a function of UV pulse intensity for several amplification voltages of the MCP is shown in Fig. 2.8. At high amplifications the MCP shows saturation effects even at very low UV intensities because of high peak power. We usually used 1.25 to 1.3 kV in order to obtain adequate signal strength and still remain in a linear region. The MCP had a 5 mm hole drilled in the center of each plate. The purpose of this hole is to prevent the amplification of the strong directly transmitted (000) beam. The constant illumination of this zero order (primary) beam on the phosphor layer will reduce its lifetime. A high voltage of between 4.0 and 5.0 kV was applied on the P-47 phosphor. The spectral response of the phosphor is shown in Fig. 2.9. The spectral response peak is around 410 nm. In photographic imaging analysis, a high resolution aerographic film with UV-sensitivity that provides a good match to this spectral response was chosen.

(c) Synchronization of pump and probe beams

A laser-activated electron-deflection technique⁶⁻⁷ was applied to accomplish synchronization between the laser heating pulse and the electron-probe beam. A balanced stripline formed by two planar electrodes was used as the electron deflection assembly. A photoconductive silicon switch was integrated into the top electrode. When the switch is activated by an IR laser pulse, an electric field is established between the two electrodes with a rise-time equal to the IR pulse duration. Since zero time is when the electron probe beam is coincident with the IR heating beam at the sample

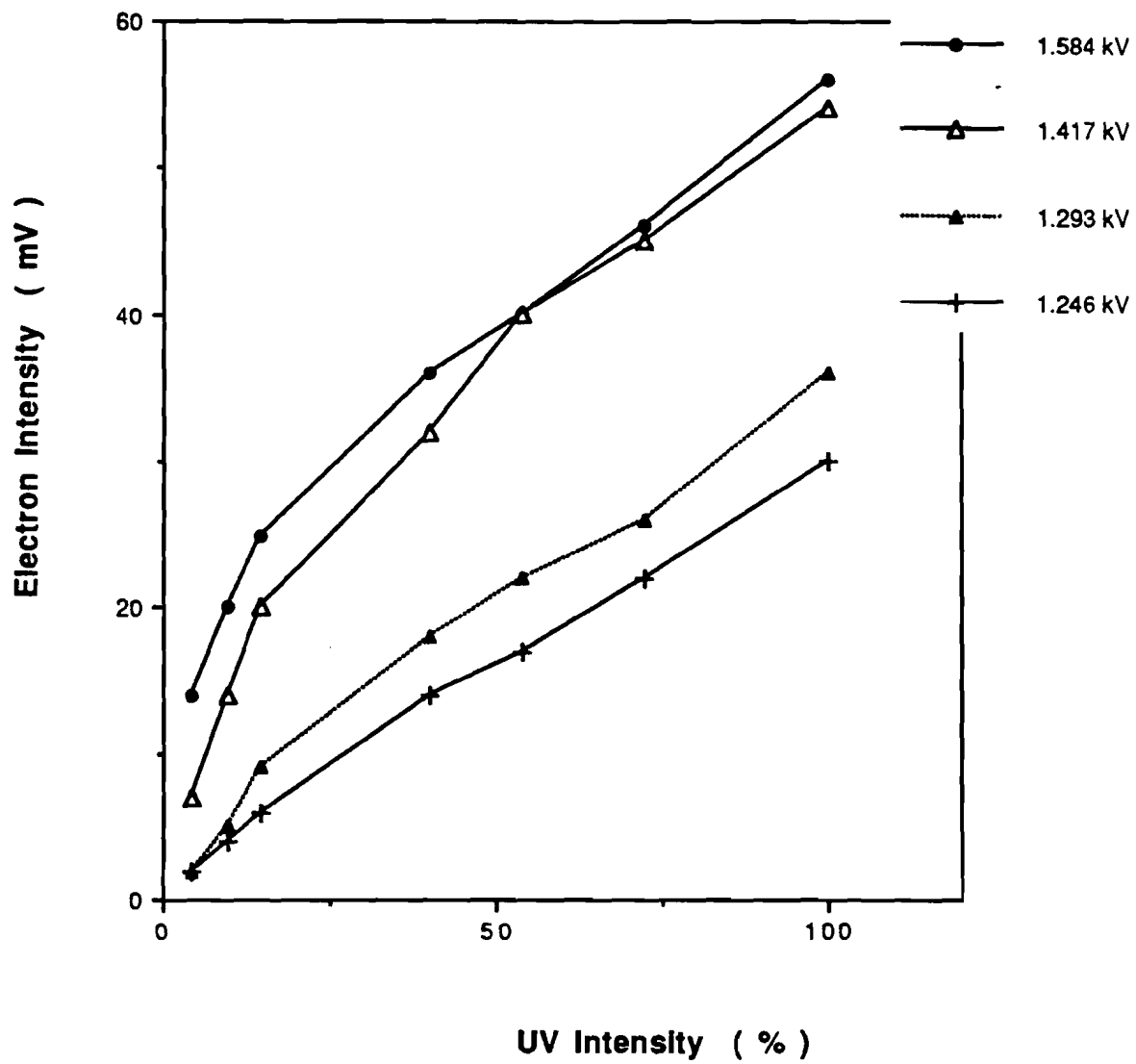


Fig. 2.8 Transmitted electron intensity as a function of UV intensity for various MCP amplification voltages.

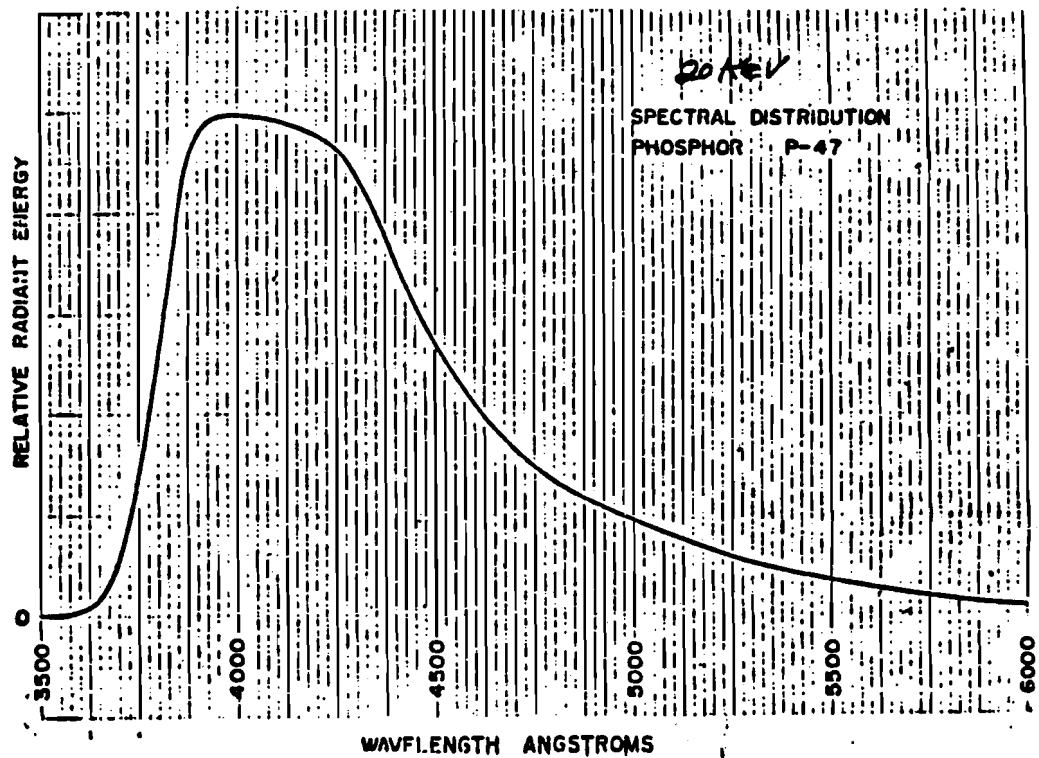


Fig. 2.9 Spectral response of P-47 phosphor for 20 keV electrons. The response changes very little for higher electron energies.

position, the deflection plate assembly was placed in the path of the electron beam at the position where the sample would be in the experiments. In the synchronization procedure, the IR pump pulse activates the photoconductive switch, producing an electric field at the sample position. If the electron pulse arrives before the switch is activated, no electron deflection is observed; otherwise the electron beam position on the phosphor screen is shifted. The IR delay line is adjusted until the electron beam profile on the phosphor screen shows a unique double spot. This indicates that the pump and probe pulses are synchronized. This method will determine the "zero time" within an accuracy of 50 ps, the same as the time resolution of electron pulse. A diagram showing the changes in shape and position of the electron beam image on the screen as a result of altering the relative timing of the IR and electron beams was given in ref. 8. This diagram is reproduced in Fig. 2.10. The two peaks at $t=0$ indicate that electron pulse was at the sample position just as the IR laser activated the photoconductive switch.

The significant features of this ultrafast electron probe are the following:

- (a) It can provide an extremely short electron pulse; (~ 20 ps);
- (b) The electrons are monoenergetic with a relative energy spread of about 10^{-4} ;
- (c) The electron pulse can be synchronized with the optical pulse to tens of picoseconds accuracy depending on the duration of optical pulse. A portion of the same infrared laser pulse that generates the electron pulse can be split off and passed through an optical delay line to provide a synchronized heating pulse to the specimen.

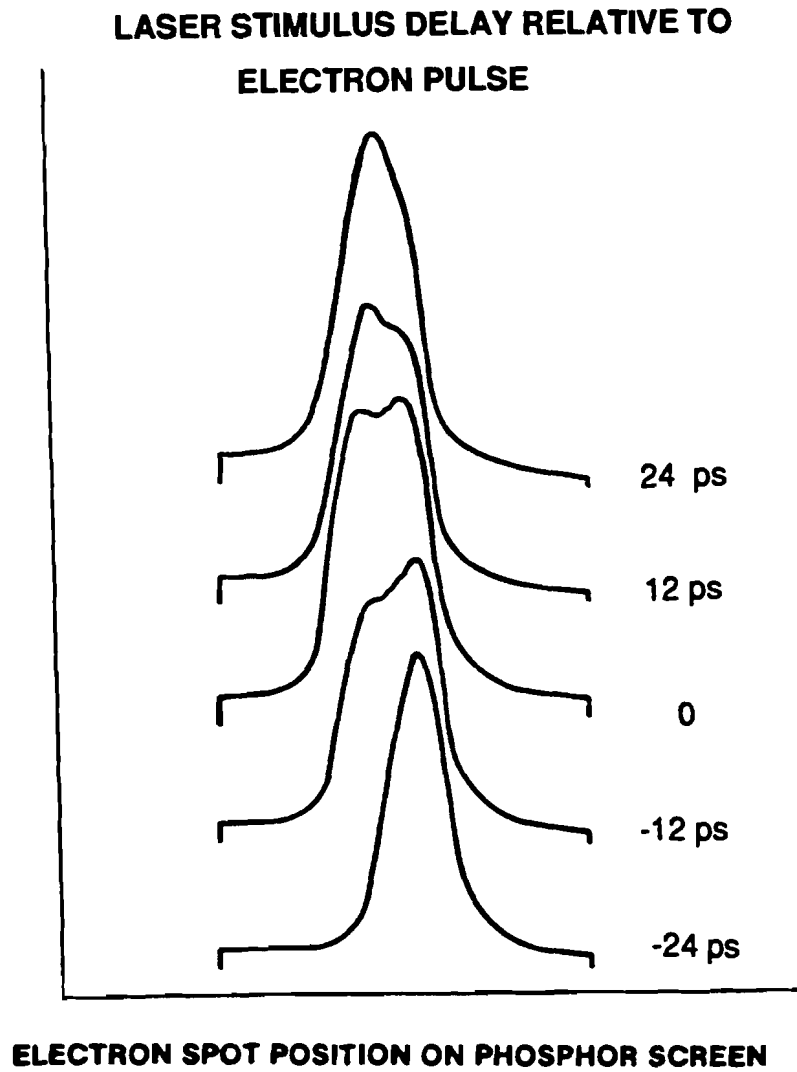


Fig. 2.10 Spatial profile of electron beam for various delay times between the IR pulse and the electron probe. (From ref. 8.)

2.3 STEADY-STATE DEBYE-WALLER EFFECT IN THIN Al FILMS

During the initial stage of the development of the ultrafast electron probe, a study was made of the Debye-Waller effect in thin polycrystalline Al film. The electron diffraction intensity measurement was carried out using the electron diffraction system described in the previous section. However, a UV mercury lamp was used to generate the photoelectrons instead of the REGEN laser system in order to produce a CW electron beam. The Al sample was prepared by vacuum evaporation with a deposition rate of 1 Å per second on a formvar substrate that was later removed by ethylene dichloride vapor etching. The details of its preparation are given in Appendix A. The sample was mounted on a specimen holder and was otherwise free-standing. The diameter and the thickness were 0.5 mm and 25 nm, respectively. The heating was achieved by attaching the sample onto a hot plate which was heated uniformly. A temperature rise from room temperature to 400 C was achieved. The temperature of the sample was monitored by a copper-constantan thermocouple. Signal-to-noise ratio (S/N) enhancement was achieved by using a EG&G PAR Model 124A lock-in amplifier with a Model 116 differential preamplifier.

In this experiment (see Fig. 2.11) two nearly identical Al specimens with a polycrystalline structure were used. One specimen was heated by the hot plate and the other remained at room temperature. The CW electron beam was deflected every 0.5 ms by using a pair of deflector plates which was driven by a 1 kHz square wave from a pulse generator. The two specimens

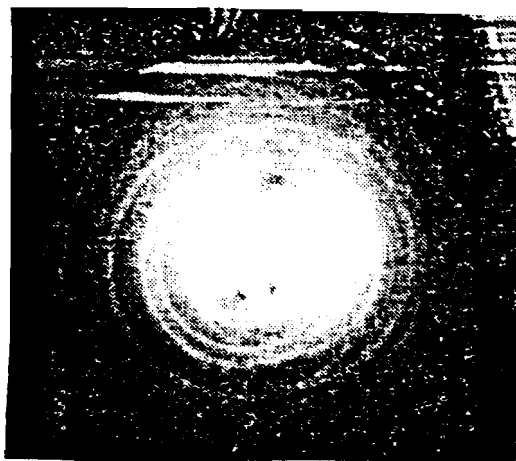
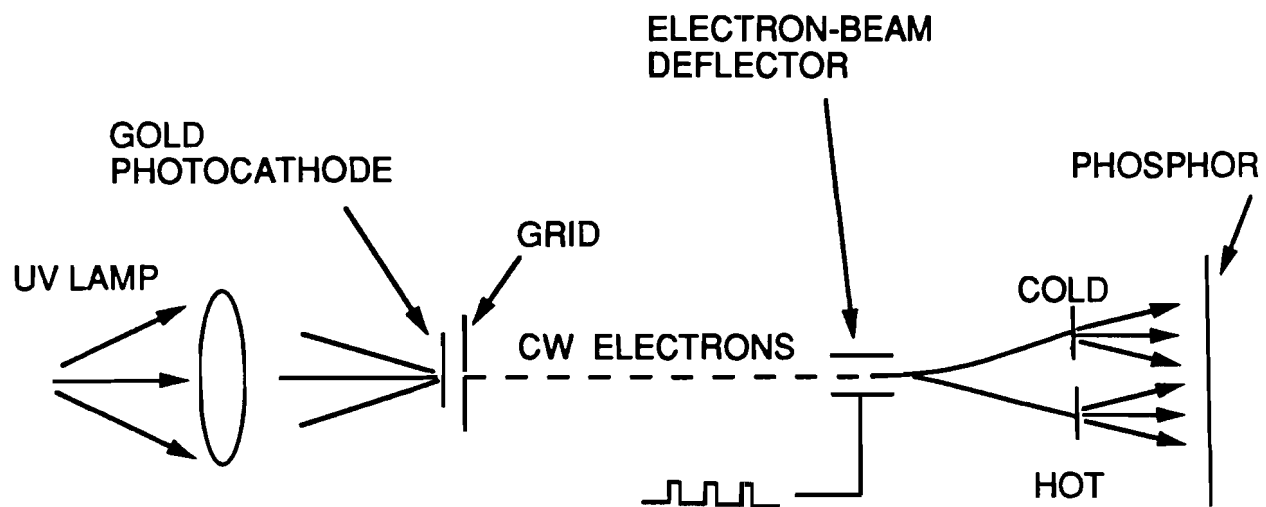


Fig. 2.11 Schematic of the experimental arrangement for a CW electron probe of polycrystalline aluminum film. Also shown is a photograph of the resulting diffraction pattern.

were positioned so that they were alternately irradiated by the moving electron beam. The dual electron diffraction image so produced is shown in Fig. 2.11. The square wave was also used to trigger the reference channel of the lock-in amplifier. The dual diffraction image was masked off so that only the 220 order rings (the third one from the center of each diffraction pattern) were visible. The intensities of the 220 order rings were measured with a large-area photodiode connected to the input of the preamplifier. The lock-in amplifier converted the intensity difference of the hot and cold specimens into a DC level which was applied to the Y-input of an X-Y chart recorder. The temperature of the hot specimen was measured by a copper-constantan thermocouple which had one junction in contact with the hot plate at temperature T and the reference junction in contact with the ground plane at the room temperature T_0 . The thermoelectric emf corresponding to a temperature $\Delta T = T - T_0$ was applied to the X-input of the chart recorder. The raw data is shown in Fig. 2.12 with the intensity difference in arbitrary units. Before these data can be used, the thermoelectric emf plotted on the X-axis must be converted into temperature. This was done using the manufacturer's published data.

Figure 2.13 shows the normalized intensity difference Y plotted against the temperature difference $\Delta T = T - T_0$. The normalized intensity difference Y is defined by

$$Y = (I_{\text{cold}} - I_{\text{hot}}) / I_{\text{cold}}, \quad 2.1$$

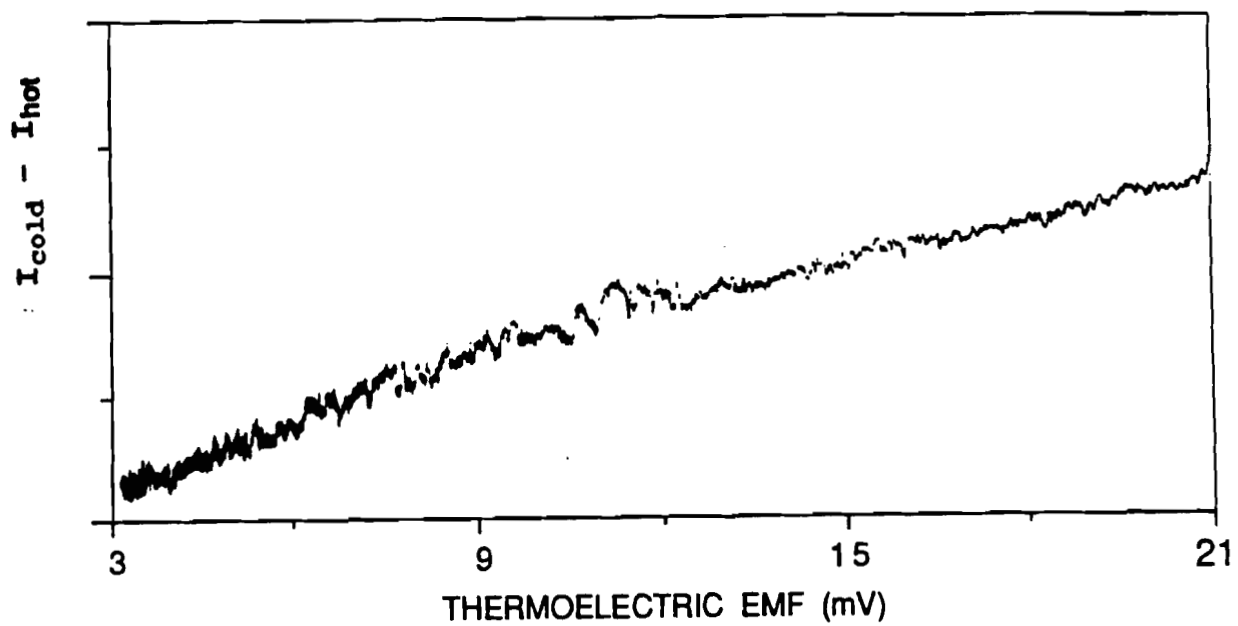


Fig. 2.12 Negative of the change in the electron diffraction intensity of polycrystalline aluminum (arbitrary units) as a function of thermocouple emf.

where I_{hot} (I_{cold}) is the intensity of the 220 diffraction ring of the hot (cold) specimen. The data show a quasi-linear characteristic. The normalized electron diffraction intensity Eq. (2.1) can be rewritten in terms of ΔT by using Debye's expression for the temperature-dependent diffraction intensity Eq. (1.2) for the case $T > (1/3)\Theta$, resulting in

$$Y = 1 - \exp[-\beta \Delta T] \quad 2.2$$

Here $\beta = 3h^2/mk_B d_{hkl}^2 \Theta^2$; all these quantities are the same as those defined in Eq. (1.3). When the two specimens are at the same temperature, Y is zero. At extremely high temperatures, Y approaches unity. For small values of $\beta \Delta T$, Y may be approximated by

$$Y = \beta \Delta T \quad 2.3$$

This implies that in Fig. 2.13 the slope of the straight dashed line passing through the data points at small ΔT values is just β . The β value for the (220)-order of Al was found to be $4.9 \times 10^{-4} \text{ K}^{-1}$. This value for β was then inserted into Eq. (2.2) to plot the solid curve in Fig. 2.13. The solid curve, as expected, show significantly better agreement with the experimental data for large ΔT compared with the dashed straight line.

The results show that diffraction intensity profile of polycrystalline Al films conforms to the Debye-Waller theory. The Debye temperature of aluminum is determined to be $450 \pm 50 \text{ K}$, in close agreement with the known

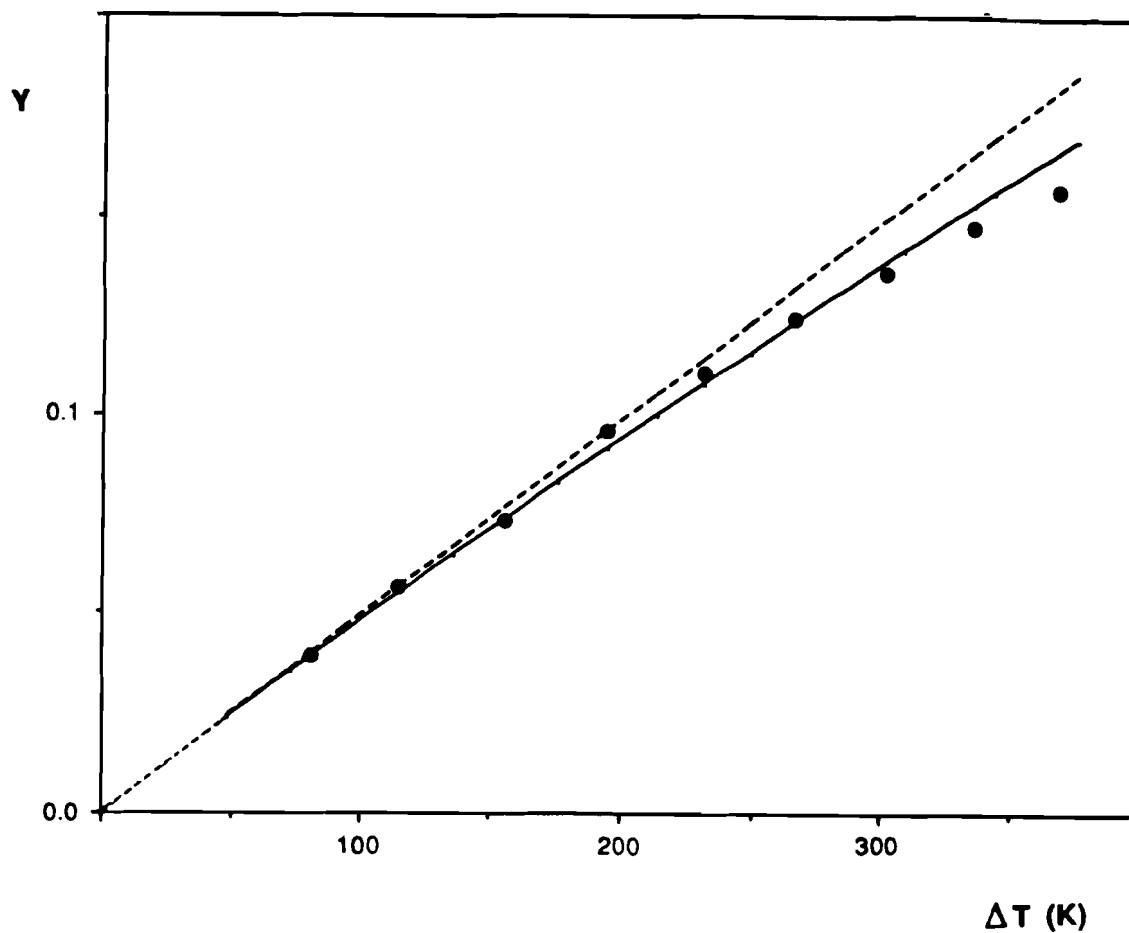


Fig. 2.13 The normalized electron diffraction intensity Y (Eq. 2.1) as a function of temperature rise from ambient temperature for polycrystalline aluminum. The slope of the dashed line is found to be $4.9 \times 10^{-4} \text{ K}^{-1}$. The dots are the experimental points and the solid line was fitted with Eq. 2.2.

value of 420 K for bulk aluminum.⁹

2.4 TIME RESOLVED ELECTRON DIFFRACTION INTENSITY MEASUREMENTS

(a) Introduction

We have already seen that by making steady-state electron diffraction intensity measurements, the lattice temperature can be deduced from the temperature dependence of the electron diffraction intensity. However, time-resolved measurements are much richer in information than steady-state measurements. An ultrafast electron probe is potentially capable of providing insight into many solid state phenomena such as lattice dynamics in crystals, energy transfer processes, phase changes, defect formation, and various surface processes. In this section we report 100-ps time-resolved measurements of the diffraction intensities of Au film irradiated by an IR laser pulse.

In principle, the measurement of a time-resolved electron diffraction intensity profile is straightforward. However, the desired signal may be hidden because of the large fluctuations originating from both the laser and the production of the electron pulse. An additional hurdle is the low average level of the electron diffraction intensity. The diffraction pattern can be enhanced by using image intensifier, but this procedure also contributes noise at the same time. So a major goal of this experiment was to develop a measuring technique to extract the change in time-resolved electron diffraction intensity

caused by pulsed laser heating.

We investigated several techniques, including using a boxcar averager, electronic imaging by video camera, and a photographic imaging method. Two different and complementary methods have been successfully implemented. The photographic imaging technique was used extensively in the beginning. This technique basically consists of two steps: digitization of a photographic negative of the electron diffraction image and signal processing by computer data analysis. The photographic imaging method is best suited for investigating global features of the diffraction image such as the distribution of thermal diffuse scattering. This method may also be used to investigate specific features such as diffraction maxima, but it is more cumbersome and susceptible to noise than our other method. With this other technique, a personal computer is used to control the experiment. The diffraction image is masked off except for the specific feature of interest. The intensity is measured with a photomultiplier tube connected to a boxcar averager that serves as a gated integrator. The use of the computer allows the noise from some sources to be reduced.

(b) Experimental consideration

Before proceeding further, we describe the experimental features common to both techniques.

High electron flux is desirable in the experiment for good signal-to-noise ratio. Unfortunately, the maximum electron flux is constrained

by space-charge broadening effects arising from the mutual repulsion of the electrons. Low electron flux, therefore, is required in order to prevent space-charge broadening of the pulse which would reduce the temporal resolution of the electron beam. We have measured the duration of the electron pulse using a streak camera and have confirmed that the electron pulse has the same duration as the UV pulse for sufficiently low UV intensity. This constraint on the electron flux may be relaxed somewhat if a longer electron pulse duration is acceptable. However, it may then be necessary to carefully consider the heating effect of the electron probe on the sample.¹⁰⁻¹³ We have made a worst case analysis of this effect where we have assumed all the energy of the electron pulse is deposited into the sample. Our calculations show only a modest 15 K rise for the gold samples that we used in our experiments. Additional evidence that electron heating is insignificant was provided by changing the UV intensity and hence, the electron flux in our experiments; our results remained the same in each case. The low electron flux used in our experiments, in order to obtain good time resolution, results in a poor signal-to-noise ratio in the electron diffraction intensity measurements, and therefore it is necessary to employ signal enhancement methods as discussed below.

Because of the need to resolve very small changes in the diffraction intensity due to laser heating, the stability of the heating fluence on the sample is critical to the success of the experiment. The path of the heating beam passes through an optical line and also a rotating filter used to control the

heating fluence. The adjustment of either of these two components may alter the alignment of the heating beam on the sample. The sample, which was mounted on a specimen holder, was about 0.5 mm in diameter and roughly a factor of two smaller than the heating beam spot. Thus, it was possible to monitor the transmitted laser intensity to check the alignment of the heating beam. A mirror was placed behind the sample to intersect the transmitted heating beam. This beam was then monitored by photodiode connected to a fast oscilloscope. The alignment was checked and readjusted if necessary after each change of the optical delay line or the rotating filter. This procedure also served to detect sample damage. A sudden large increase in the transmitted intensity through the sample is an indicator of permanent damage in the sample.

One of the most difficult aspects of the experiment involved the retrieval of the signal from the large amount of noise present. A major source of noise is the REGEN laser system. The short-term (shot-to-shot) laser fluctuation was about 5% and there was a long-term drift with a time scale of several seconds that could result in a fluctuation as high as 10 to 15%. Some noise is also contributed to the UV beam by the frequency-doubling crystals and a large amount of shot noise is produced by the photoelectric process and the image intensifier. The measured electron diffraction intensity had around 40% fluctuation, but it could be even greater with a damaged photocathode. The typical photocathode lifetime was found to be about 100 hours.

(c) Photographic imaging technique

Digital image signal processing was developed to study a three-dimensional real-world physical process through a two-dimensional image which is projected by means of an optical process, such as diffraction, absorption, reflection, or emission. An image acquired by photographic means is analog in nature. In order to obtain information by using computer image enhancement, the image must first be quantized with respect to its spatial coordinates and intensities. A digitized image is usually analyzed using one or more computerized signal-processing methods, which include digital image enhancement, image restoration, and even image segmentation, before it is interpreted. A block diagram of digital image analysis is shown in Fig. 2.14. A fundamental part of two-dimensional signal imaging is based on the Fourier transform which provides a useful signal analysis technique for obtaining information from a physical process.¹⁴ The theory of the Fourier transform can be used to analyze or characterize relationships not evident in the brightness (gray-scale) distribution of the digitized image through a space, time, or intensity representation.

Film images of the diffraction pattern at various probe delays were obtained. The spectral response of the P-47 phosphor used in the electron diffraction experiment is shown in Fig. 2.9 for an incident electron energy of 20 keV. The wavelength corresponding to maximum response shifts very little for electron energy above 20 keV. A blue-sensitive aerographic duplicating film therefore was chosen to record the electron diffraction images.

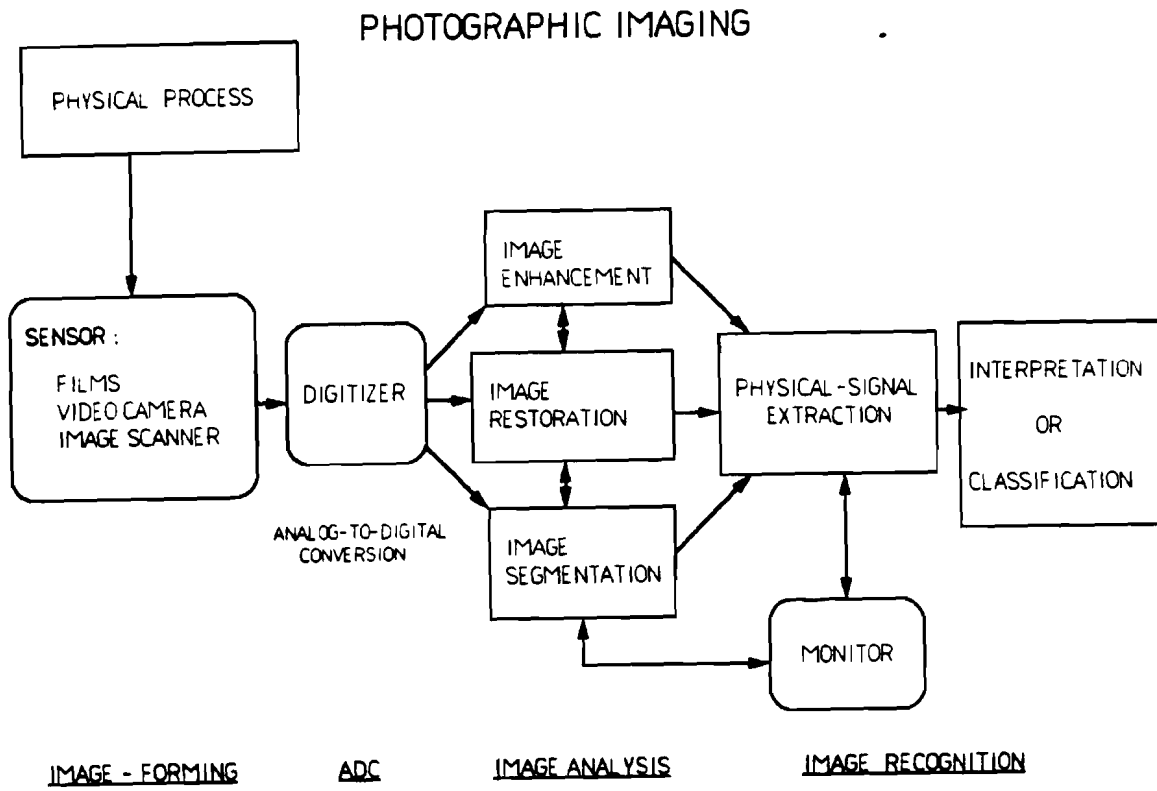


Fig. 2.14 Block diagram showing the digital image analysis process.

A custom-made film holder was used to obtain contact negatives of the diffraction images off the fiber-optic faceplate.

The negative duplicating film used, Kodak aerographic 4421, was found to have very little variation from batch to batch so the error contribution from this source could be ignored. This black-and-white negative duplicating film has a very high resolution, extremely fine grain emulsion. The resolving power is $4\mu\text{m}$ and $10\mu\text{m}$ for a image contrast of 1000:1 and 1.6:1, respectively. The thick ESTAR base (about 7-mil) of the film provides excellent dimensional stability, which is required in the accurate mapping of images.

The microchannel plates (MCP) amplification voltage was set at between 1.25 and 1.3 kV for the best signal level while keeping the linear relationship between the electron intensity and the UV intensity. For this image brightness, an exposure time of 50-60 seconds was normally used. The exposed films were processed in a JOBO ATL-1 processor, with 1:1 Kodak DK-50 developer. The developing time was maintained at 7 minutes at 20 C throughout the process.

A necessary part of our experimental procedure was the creation of a D-log I (image density vs. logarithm of intensity) calibration curve that relates electron diffraction intensity to the image density of the film developed under these processing conditions. The first step was to make four contact negatives of a defocussed electron beam set at four different intensities. There was no sample in the electron beam path. The electron beam intensity was reduced

by a factor of 2, 4, and 8, in succession, by inserting appropriate UV filters in the UV beam path. Linearity of the electron beam intensity with respect to the UV beam intensity was ensured by measuring the intensity of the beam image on the phosphor screen with a photodetector as each filter was inserted. The photodetector was UV-sensitive to match the phosphor spectral response. These four pieces of photographic film were developed using the same film processing condition as in the experiments in order to obtain a valid D-log I conversion curve for the experimental data. Each piece of film was digitized to obtain density levels corresponding to exposures that differ by factor of 2. These density values were then used as inputs to an Image Analysis Laboratory (IAL) "dlog I" computer program to produce an intensity calibration file. The "dlog I" routine produces a D-log I conversion curve, (displayed in Fig. 2.15) that can be used to map pixel values (actually densities) into intensities.

Information on photographic film is analog in nature. Converting the grey-tones of a black-and-white photograph to density levels is the first step in digital image processing. These density levels, which are defined as the degrees of opacity of a translucent material, can be converted into numbers by digitization with a microdensitometer. The light transmitted through each picture element, isolated by an aperture of a suitable size, is measured with a photodetector. The logarithm of the opacity, i.e., $\log(1/T_1)$, where T_1 is the transmittance, is equal to the density which is then digitized and stored in a computer. In this way, the entire photographic film can be converted into a

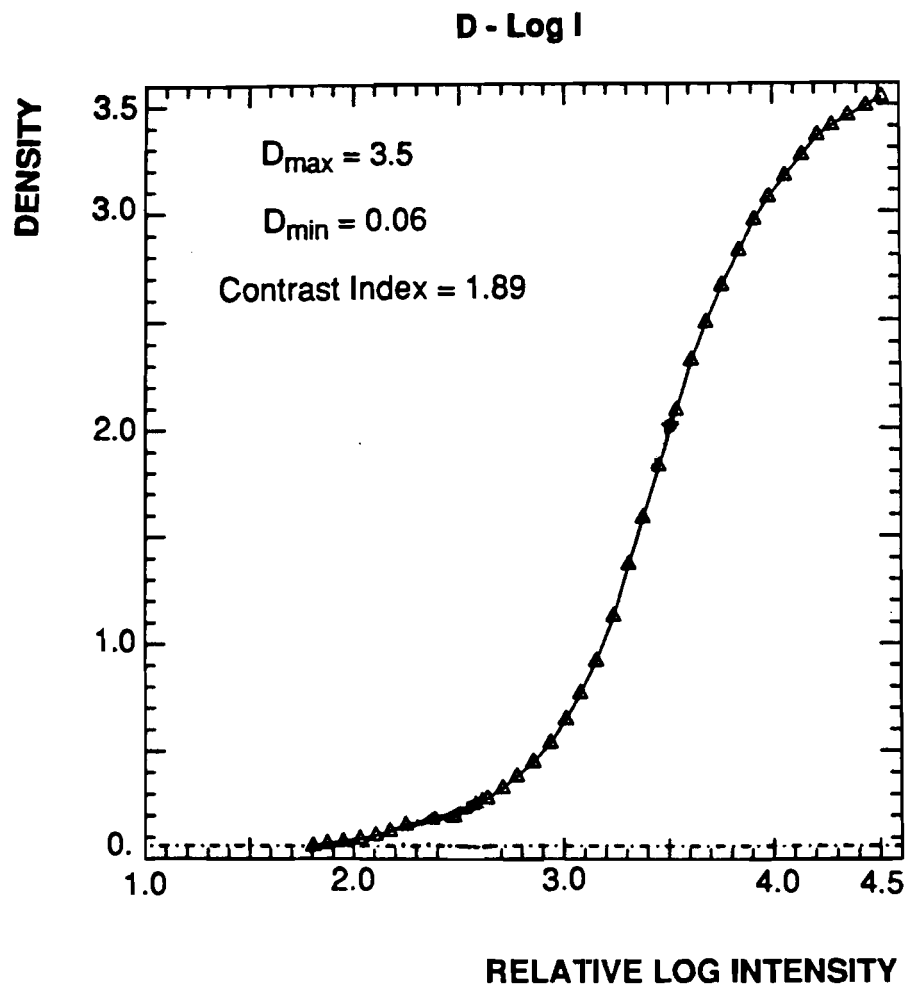


Fig. 2.15 D-log I curve for translating image densities to intensities.

matrix of numbers available for digital image analysis. Each picture element after the digitization represents a discrete element known as a pixel. In order to preserve the data of a picture, the pixel size or aperture size should be comparable to the resolving power of the film.

The microdensitometer used in the IAL of Laboratory for Laser Energetics at the University of Rochester is a Perkin-Elmer PDS Microdensitometer System, Model 1010GMS, and is herein referred to as the PDS (for photometric data system). The PDS is especially designed to take highly accurate density readings of extremely small areas, as small as 5 micrometers of photographic film. The 12-bit PDS can measure analog densities of up to 5.12, i.e., a pixel value of 4095 corresponds to a density of 5.12. This relationship can be used to compute the density of a digitized image from its pixel value. Square or rectangular apertures are available on this unit. The actual size of aperture used depends on the particular application. An extremely small aperture size is not recommended because of jitter due to vibration. For a small segment of the electron diffraction image, a square aperture 25 μm by 25 μm was normally used. However, when the whole electron diffraction image was digitized, a rectangular aperture of 25 μm by 100 μm was used in order to save computer memory space and time. The intensity corresponding to each pixel value of this digital image can be obtained by intensity conversion using the D-log I conversion curve in Fig. 2.15. A digitized image, shown in grey-scale, is displayed in Fig. 2.16.

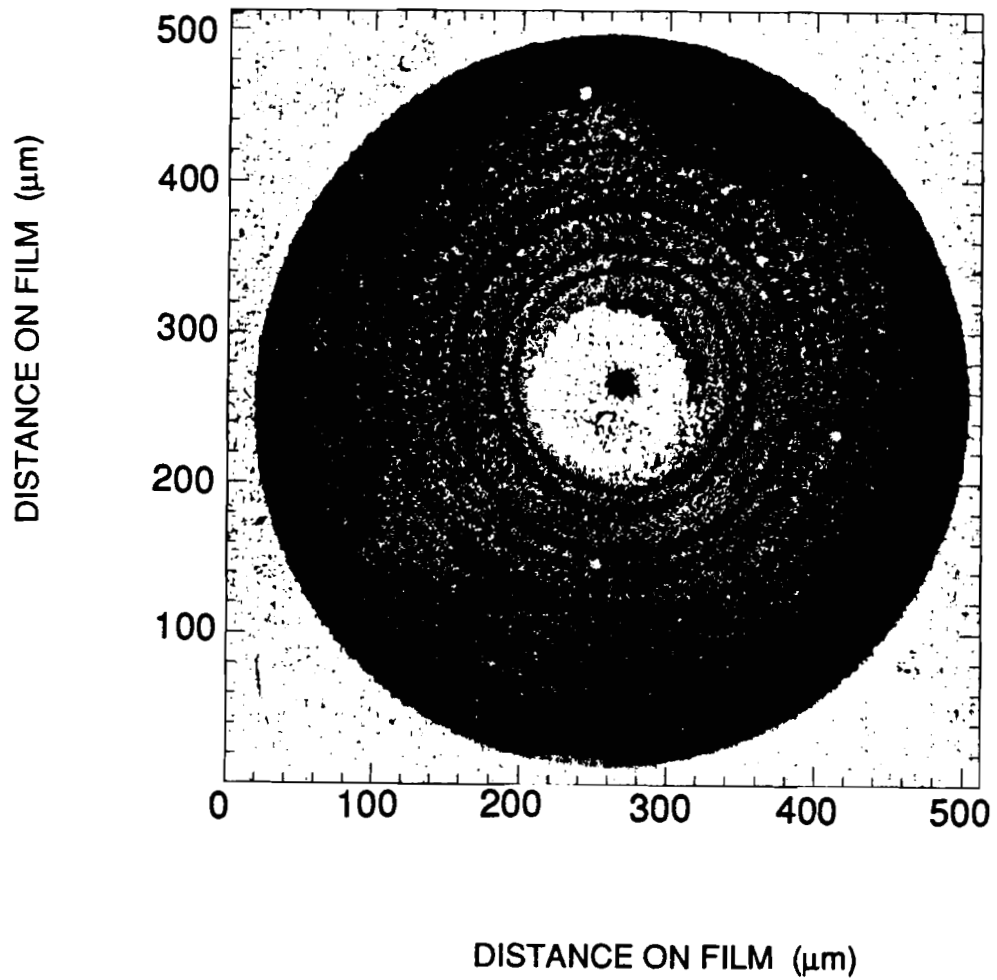


Fig. 2.16 Printout of a digitized image of the diffraction pattern of polycrystalline gold.

Note that the image quality is limited by poor printer resolution and does not reflect the quality of the image data file.

Linear smoothing operations, such as averaging can reduce the intensity spikes produced in the digitization processes. However, some fine structure of the image is lost due to suppression of high frequency components of the signal. This process produces a less sharp, i.e., slowly varying, intensity value, so that the abrupt intensity change at the transition edge is suppressed. Nonlinear median filtering was developed to avoid this disadvantage and to sustain edge sharpness of image. However, unacceptable image artifacts may sometimes result. For a circularly symmetric image, a circular operator window instead of a rectangular operator window is normally preferable. Therefore, cone low-pass filtering, which is particularly suited for circular symmetric images, was used for smoothing the polycrystalline Au diffraction images. The pixels or elements lying at a distance r from the center were averaged. All these pixels were then assigned their average value. It should be clear that the determination of the center of the diffraction image was crucial for this averaging to be effective. The author is indebted to S. Swals for his help in writing the software for this circular averaging. The circularly-averaged image is shown in Fig. 2.17. The diffraction rings are much better defined after circular averaging. The mottled appearance in some portions of the picture is a grayscale printer artifact.

Once an image is digitized, it is easy to plot a scan or "lineout" across the image in any direction desired. The computer command: LINEOUT of the

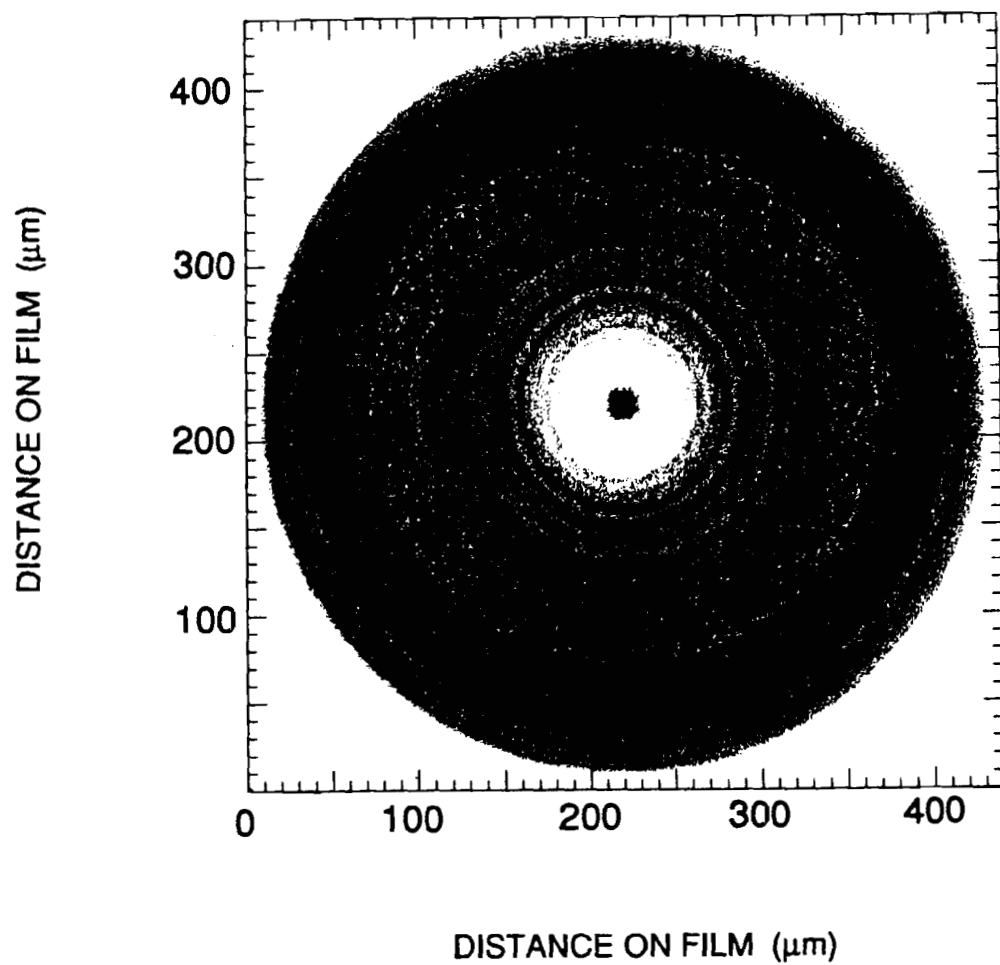


Fig. 2.17 The digitized image of Fig. 2.16 after circular averaging.

IAL software package performs this function, allowing scans to be made in any direction by specifying the appropriate coordinates. The scans are equivalent to microdensitometer traces over a specified region. It is also possible to specify a width about the specified coordinates to plot the scan as average of a number of lines around the coordinates. The width is the distance above and below the specified coordinate. The lineout can be plotted as pixel values, densities or intensities of the image. A lineout of a specified width involves a certain amount of spatial signal averaging. The lineouts of the circularly averaged image of Fig. 2.17 are presented in Figure 2.18(a). This may be compared with Fig. 2.18(b), the lineout of the raw image shown in Fig. 2.16. The lineouts are one pixel wide and they clearly show the effectiveness of circular averaging in reducing fluctuations.

The strong background intensity evident in Figs. 2.18(a) and 2.18(b) can be removed by further processing with Fourier transform techniques.¹⁵ In frequency domain representation, the slow-varying background of the electron diffraction image is represented by the low frequency components of the Fourier-transform image. High-pass filtering can eliminate or reduce the low-frequency background components. The inverse Fourier transform can then convert the image from the frequency domain back to the spatial domain. Figure 2.18(b) was processed with a Butterworth high-pass filter, and the results are shown in Fig. 2.18(c). Most of the background has been removed. The scale in Fig. 2.18(c) has been multiplied by a factor of 5 to show the peaks clearly.

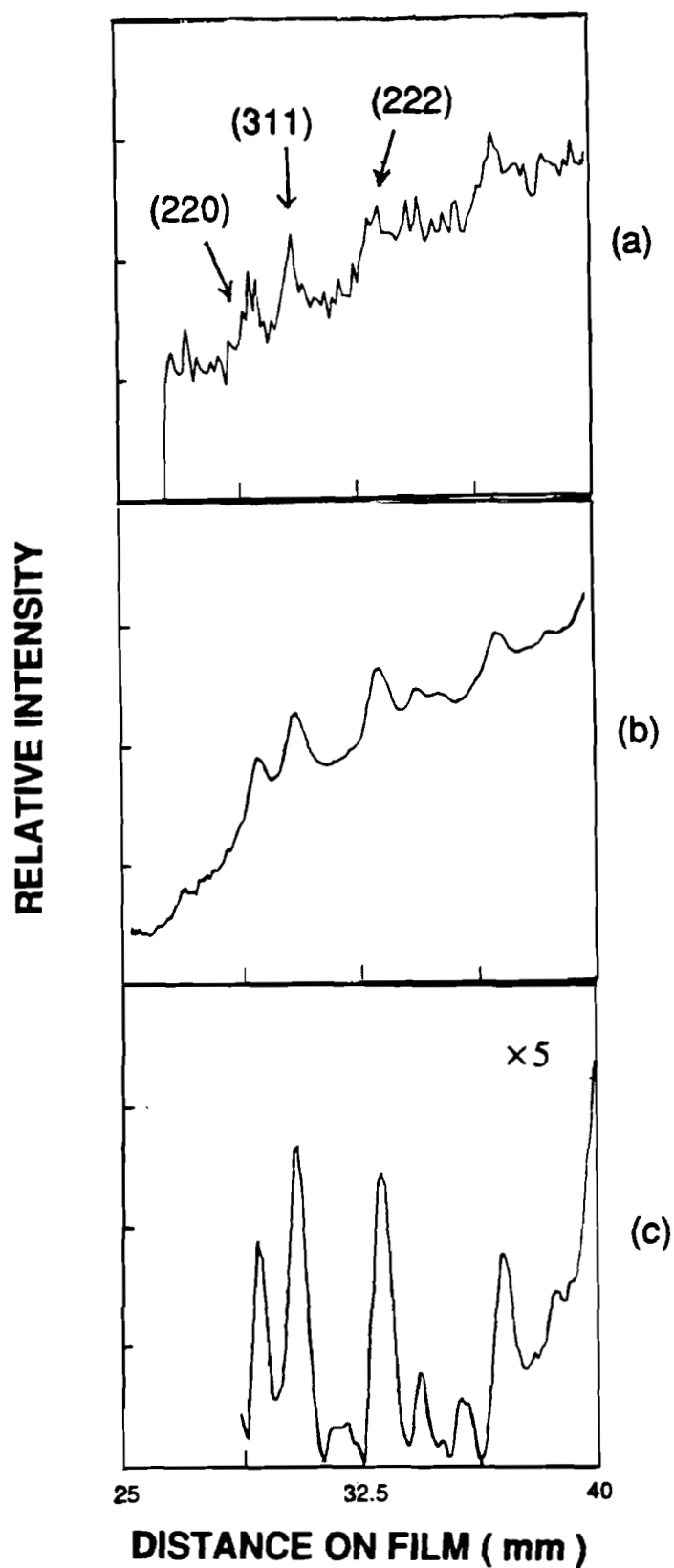


Fig. 2.18 Panel (a) shows a lineout (single-pixel scan) along a radius of the digitized image of Fig. 2.16. Panel (b) shows the corresponding lineout for the circularly averaged image of Fig. 2.17. The last panel shows the result after the lineout in panel (b) was high-pass filtered to remove the background. The intensity in (c) has been scaled by a factor of 5.

Figure 2.19 shows the lineouts of the electron diffraction patterns of polycrystalline Au at room temperature and at 100 ps and at 500 ps after laser irradiation. The lineouts were processed in the same way in Fig. 2.18(c). At 100 ps (Fig. 2.19(b)) the intensity of each peak is much reduced compared with corresponding peak at room temperature in Fig. 2.19(a). The (220) order peak shows a smaller relative reduction. We attribute this to the stronger temperature dependence for higher order diffraction maxima. At 500 ps (Fig. 2.19(c)) the intensities of the peaks show either partial or near-complete recovery. This is puzzling since, according to the Debye-Waller theory, all the peaks should recover at the same time. We will examine this anomaly more closely in the next chapter.

We have also investigated the single-crystal Au film. The film was prepared by vacuum evaporation onto a hot NaCl substrate with a deposition rate 1 Å per second. When the vapor deposition is carried out with a hot crystalline substrate, the orientation of the film follows that of the substrate and grows epitaxially.¹⁶ For the substrate, we cleaved single crystal rock salt (NaCl) to form a smooth [100] orientation. This was placed on a hot plate in the evaporator. The temperature of the substrate was monitored and maintained at 450 C. Using a low deposition rate, a continuous coherent thin single-crystal gold film with a [100] orientation could be produced. We required the thickness to be less than 30 nm for the transmission electron diffraction experiment.¹⁶ The actual thickness was 25nm. The film was removed by dissolving the substrate in water and then lifted out with a

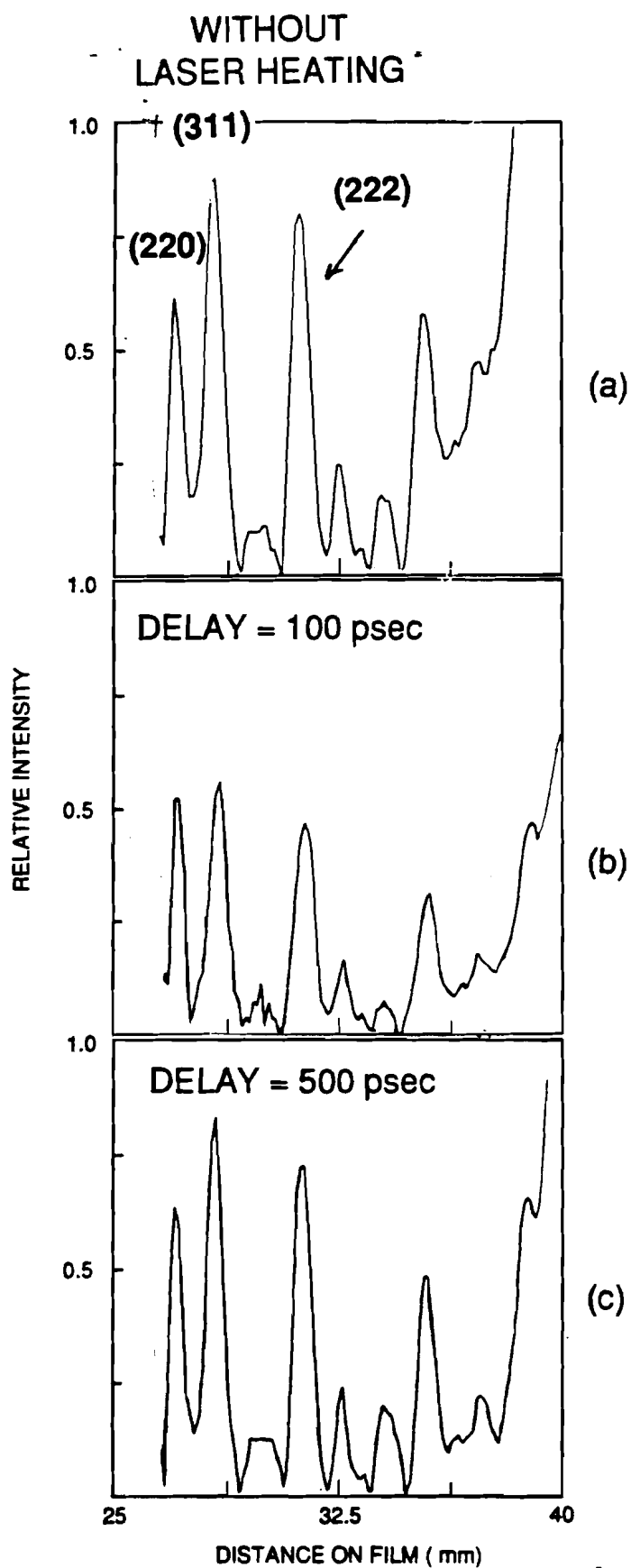


Fig. 2.19 The electron diffraction intensity of polycrystalline gold (a) without laser heating, (b) 100 ps after laser heating, and (c) 500 ps after laser heating.

specimen holder with hole diameter of 0.5mm. The sample was otherwise free-standing. The electron diffraction image for the Au single crystal in Fig. 2.20(a) shows a typical dot pattern for a face-centered cubic crystal with a [100] orientation. The digitized image is shown in Fig. 2.20(b) and each dot pattern was indexed according to the relationship

$$\frac{r_1}{r_2} = \sqrt{\frac{h_1^2 + k_1^2 + l_1^2}{h_2^2 + k_2^2 + l_2^2}}, \quad 2.4$$

where the distance r is the distance from diffraction maximum to the center, and h , k , and l are the Miller indices.

Since the diffraction peaks are much stronger than the diffused background for the case of single crystalline Au films, there is no need for extensive averaging or high-pass filtering to be applied. A 3-pixel wide lineout of the digitized image that passes over the (200), (220), and (331) diffraction peaks is shown in Figs. 2.21(a) and 2.21(b). The 3-pixel width provides a limited amount of spatial averaging. The averaging, however, does not affect the peak values of the diffraction maxima since the tops of the peaks are about 5 pixels wide. Figure 2.21(a) was taken from a sample at room temperature (no laser irradiation) and Fig. 2.21(b) was taken from a sample 1 ns after laser irradiation. The diffraction maxima are reduced as a result of laser heating. The background contribution comes from the base level of the photographic film and thermal diffuse scattering. It can be seen that the

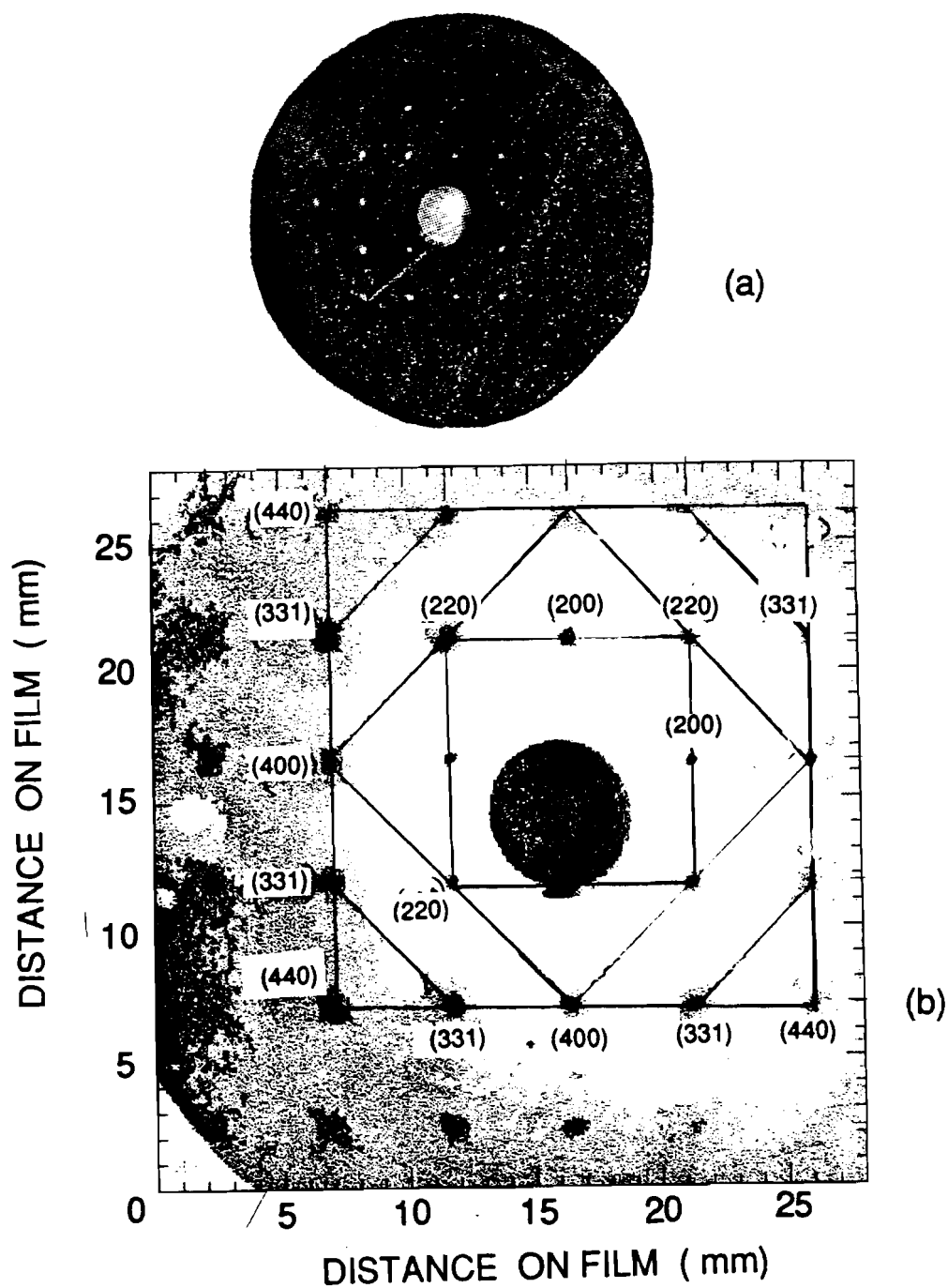


Fig. 2.20 (a) Photographic image of the diffraction pattern of single-crystal gold film. (b) A portion of the diffraction image in (a) after digitization. The diffraction maxima are indexed for a face-centered-cubic structure.

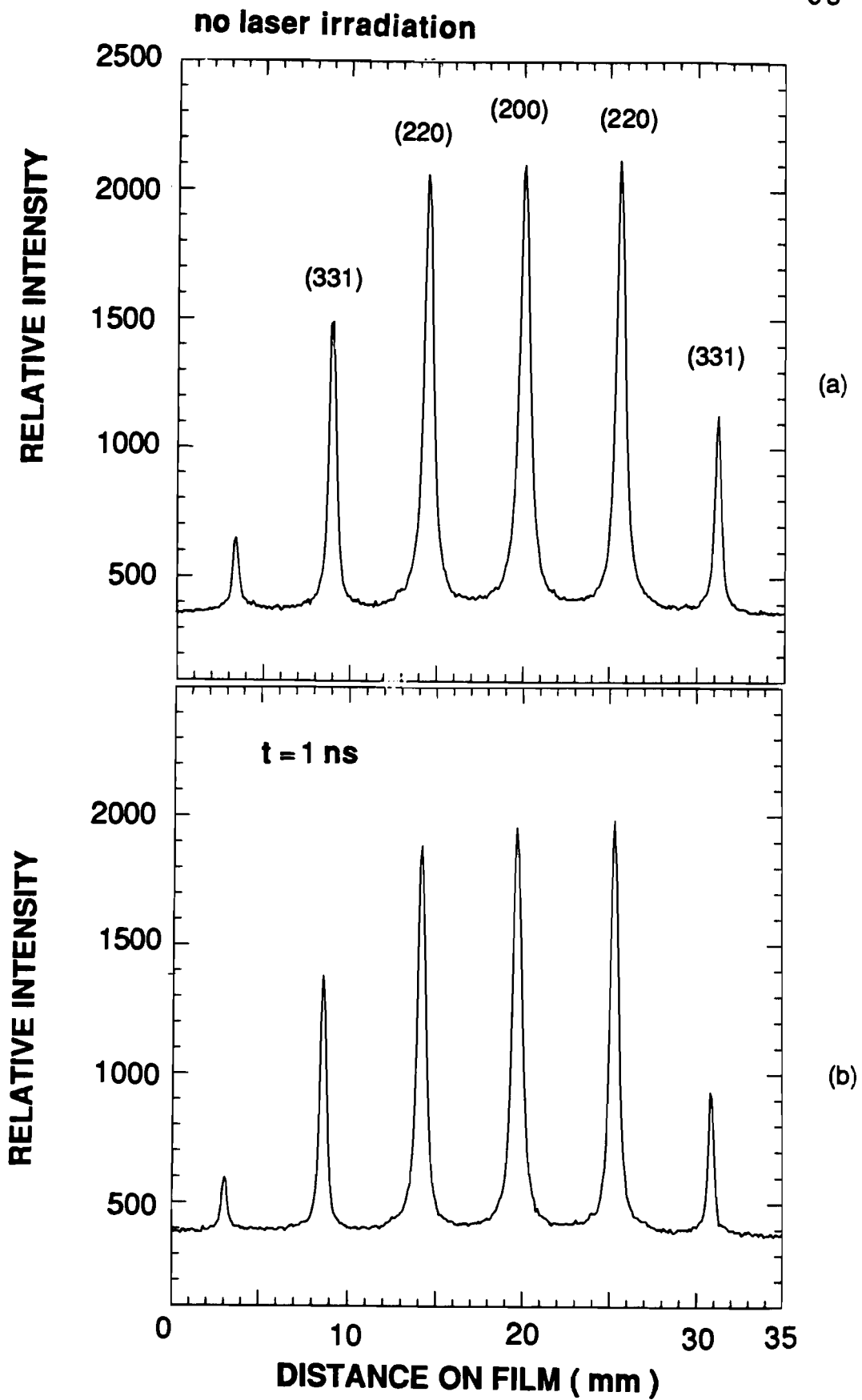


Fig. 2.21 Lineouts showing the diffraction intensity of single-crystal gold (a) without laser heating and (b) 1 ns after laser heating.

background level is slightly higher in Fig. 2.21(b) compared to Fig. 2.21(a) as a result of the loss of intensity from the diffraction maxima to the thermal diffuse background.

The diffraction intensities as a function of probe delay time for the various diffraction orders of 25-nm thick Au film can therefore be taken from the lineouts of the digitized images. The results are plotted in Figs. 2.22 and 2.23 for the (220) and (331) orders, respectively for 9 delay times. The intensities do not include the background and were normalized by the intensity measured at the room temperature, that is, without laser heating. Figures 2.22 and 2.23 each contain 2 sets of data points corresponding to separate experimental runs and they show good agreement with each other. The data points in each run were taken in no particular order to reduce the possibility of system error. The initial sharp decay is indicative of the increase of lattice temperature rise induced by laser heating. The peak-to-peak error in the intensity measurements was estimated to be less than 5%. The fast recovery and apparent oscillations following the initial decay were at odds, however, with the expected monotonic Debye-Waller curve. The limited data we have on polycrystalline Au seem to show similar behavior. To confirm that oscillations were indeed present, an additional, more extensive experimental run for the (331)-order diffraction was then carried out. The results are shown in Fig. 2.24 and clear evidence of an oscillatory behavior is observed. The error bars have been removed because of congestion. As before the data points were taken in a random order. Discrepancies in the change of the

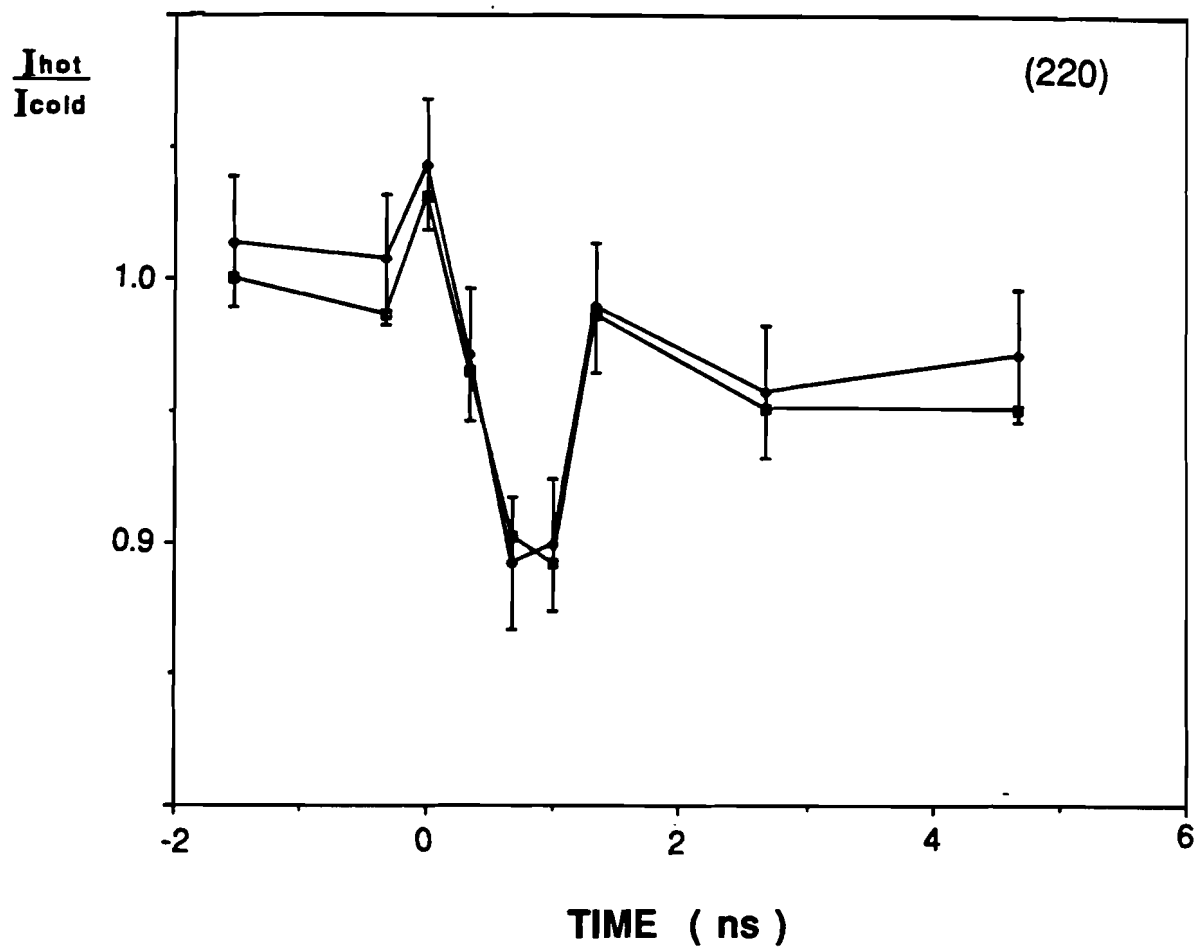


Fig. 2.22 The relative (220)-order electron diffraction intensity for single-crystal gold as a function of probe delay time. The two sets of data points correspond to different experimental runs.

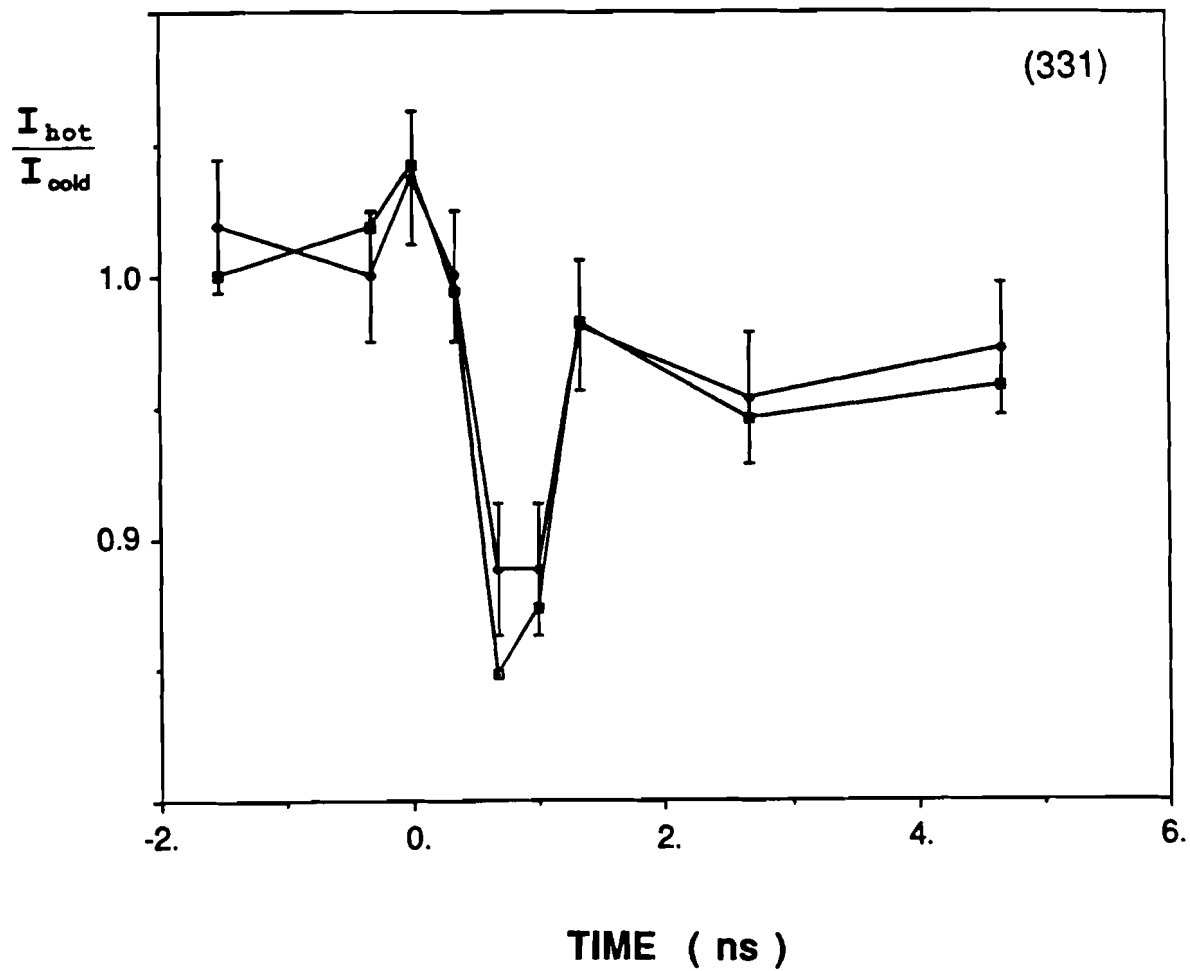


Fig. 2.23 The relative (331)-order electron diffraction intensity for single-crystal gold as a function of probe delay time. The two sets of data points correspond to different experimental runs.

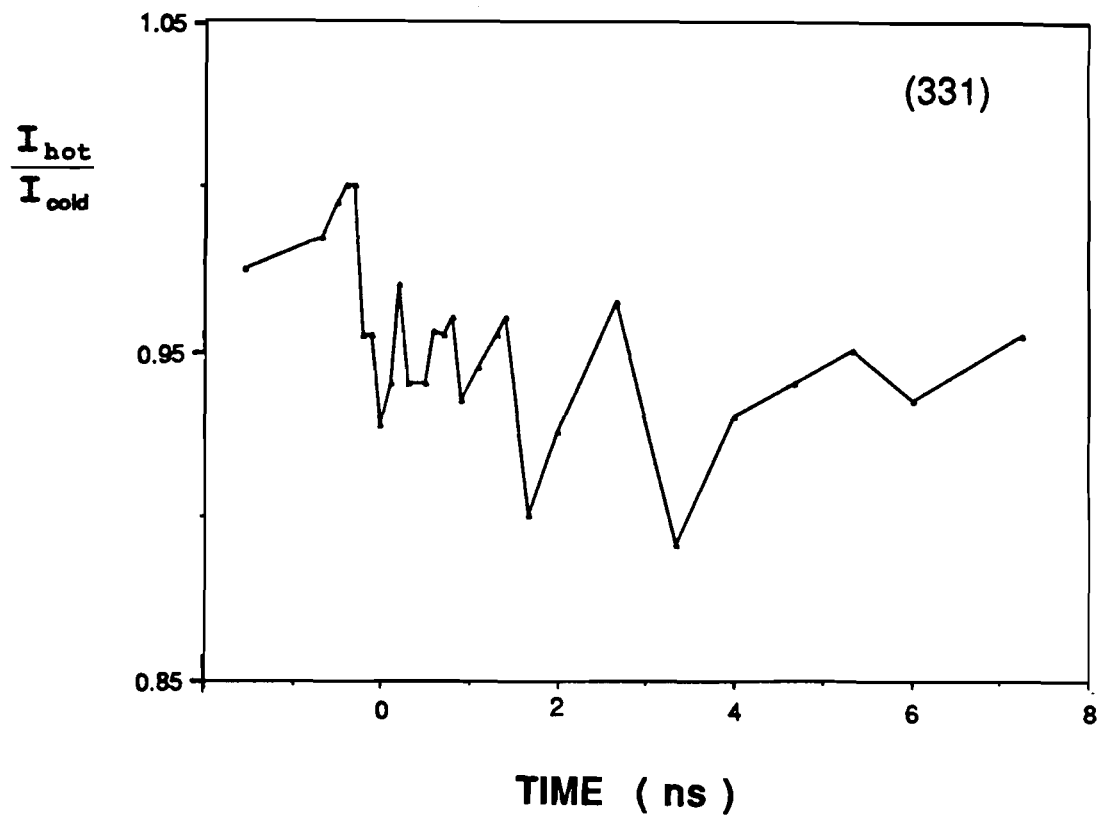


Fig. 2.24 The relative (331)-order electron diffraction intensity for single-crystal gold as a function of probe delay time. The sample used here is different from the one in Fig. 2.23.

diffraction intensity between Figs. 2.23 and 2.24 may be accounted for by the fact that different specimens were used.

The error in the intensity measurements in Figs. 2.22 and 2.24 is estimated to be less than 2.5 percent. The PDS contributes a digitizing error of less than 1 percent for the particular aperture size used. Very small apertures, which were not used in our work, may result in a larger error since jitter then becomes a problem. The D-log I calibration is not only essential but also required special care in electron diffraction intensity measurements. Usually more than 2.5% of error is possible in the density to intensity conversion process. However, in this particular experiment, we were interested in only a small relative change in electron diffraction intensity due to laser heating, and so highly accurate absolute values of the electron diffraction intensities were not needed. A small change in density of the image, ΔD , can be converted with a good accuracy to a change in the intensity ΔI , with a reasonably good D-log I conversion curve. Nevertheless, the conversion is still our greatest source of error. The long exposure time, 50-60 seconds, which is equivalent to 50-60 thousand shots when the laser system is operating at 1 kHz, was needed to average out fluctuations in the system.

(d) Sorting/averaging technique

The photographic imaging technique is basically a two-dimensional investigation where a PDS digitizer was used to quantize the film image and

convert the analog film image to digital numbers (pixel values). The information for several diffraction orders can be then obtained at the same time. The elimination of the system fluctuations depends on a long time exposure. The signal was extracted through digital data analysis of the image. We have designed an experimental procedure based on a computer interfaced boxcar that allows us to investigate specific features of the diffraction pattern more quickly and efficiently than the photographic imaging procedure and with greater accuracy.

The two key components in this scheme are an IBM compatible personal computer and a Stanford SR250 boxcar averager. The SR250 boxcar provides two input channels. Each channel contains an input amplifier and a gated integrator that features a continuously adjustable gate width of 2 nanoseconds to 15 microseconds. The gate delay can be adjusted from a few nanoseconds to 100 milliseconds, and can be triggered internally or externally. A special feature of the SR250 boxcar is its "last sample" capability which allows selective shot-to-shot measurement of a process through a computer interface. Both digital and analog output are available on the boxcar, but we chose to interface the computer to the analog output through a 12-bit analog-to-digital (adc) converter card because of superior speed. The computer and the boxcar are synchronized with the REGEN laser system. The triggering signal is the same as that used to trigger the Pockels-cell driver of the REGEN amplifier and consists of a square pulse with an amplitude of 2.5 V

and a duration of $1\mu\text{s}$. The risetime of the pulse is less than 10 ns.

This combination of a personal computer and a boxcar allows us to look at the noise of the laser system and to see the additional noise contributed by other components in the experiment. Figure 2.25 is a histogram showing the intensity distribution of the IR pulses from the REGEN laser. The intensity scale is in arbitrary units. There were 25,000 samples in the data set and the distribution shows a spread of 10 percent. The IR pulse intensity was measured using a photoconductive diode. Figure 2.26 shows the UV intensity plotted as a function of IR intensity in arbitrary units. The data contains 500 samples. The short term spread in the IR pulse intensity is 5 percent, which is typical. The corresponding spread in the UV intensity is 15 percent, reflecting the additional noise contributed by the KDP and ADP frequency-doubling crystals. The UV intensity was measured with a UV sensitive photodetector and the intensity increases with the fourth power of the IR intensity, which is as expected for fourth harmonic generation. Figure 2.27 shows the electron diffraction intensity of single crystal Au as a function of IR intensity for 4 sets of 500 shots. As in Fig. 2.26, the IR intensity show a 5 percent spread in each of the four cases, but the center of the IR distribution changes because of long-term fluctuations in the laser system. The electron diffraction intensity shows a spread of 40-50 percent. This is partly due to a deteriorating photocathode. With a fresh photocathode, the spread is usually about 35 percent which is still large. Because of the much larger amount of

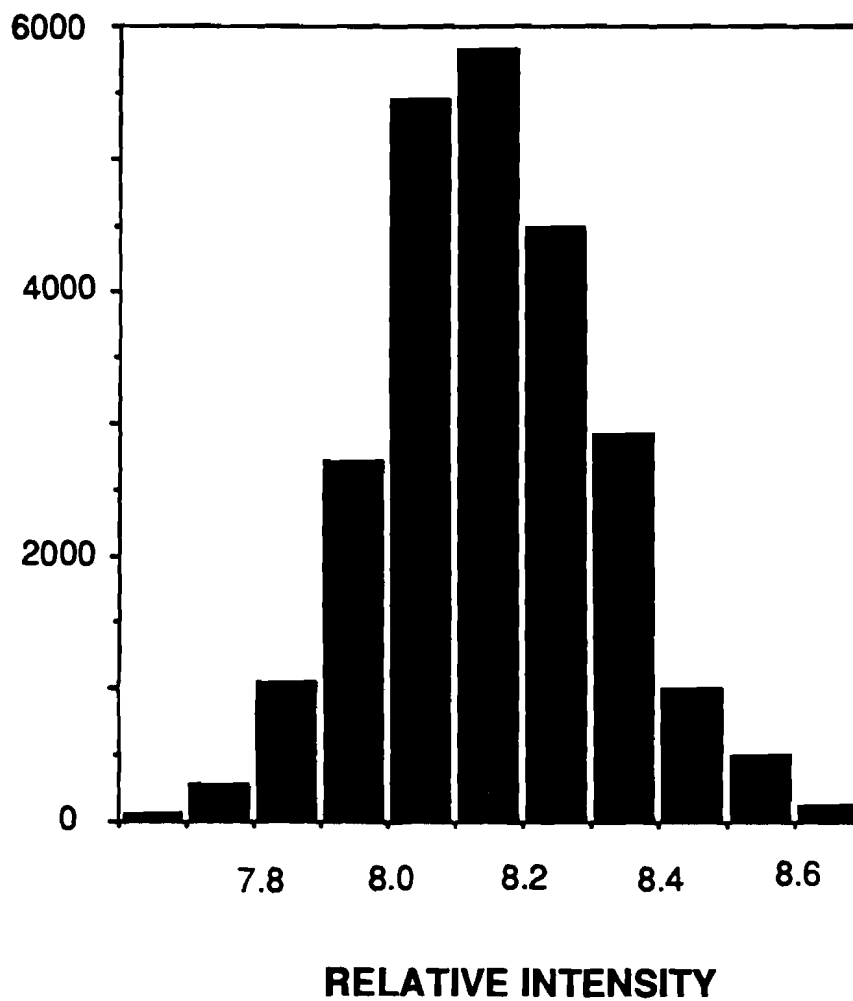


Fig. 2.25 Histogram showing the energy distribution of the REGEN laser pulse output. The data represents 25,000 consecutive samples. The asymmetry in the distribution is due to long-term laser fluctuations.

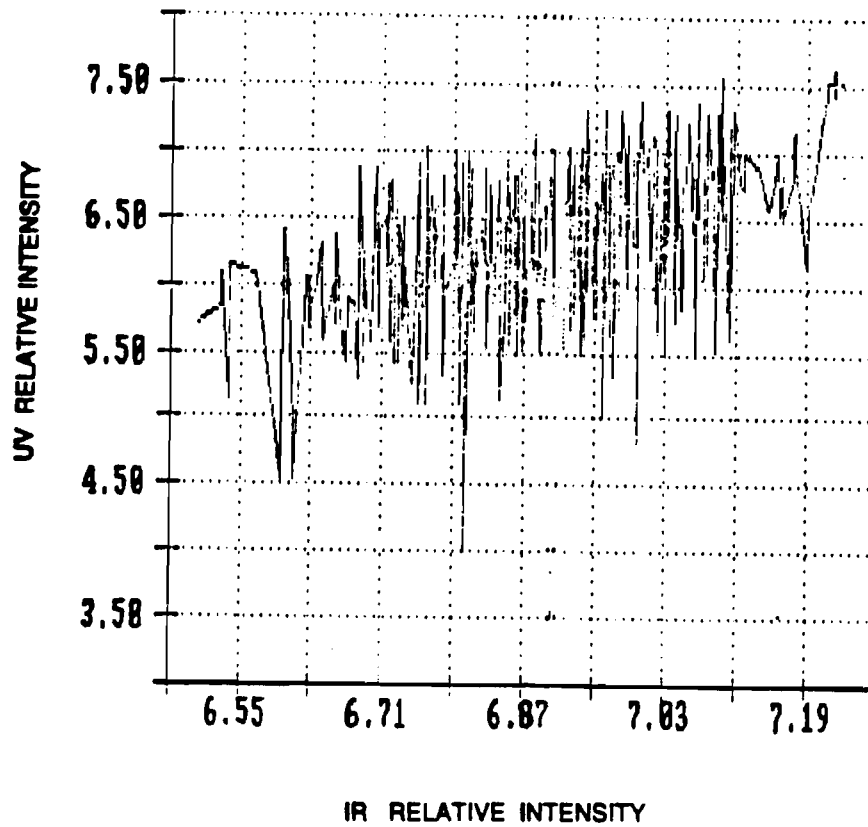


Fig. 2.26 The measured UV pulse intensity and the corresponding IR pulse intensity plotted for 500 samples. Both intensity scales are in arbitrary units.

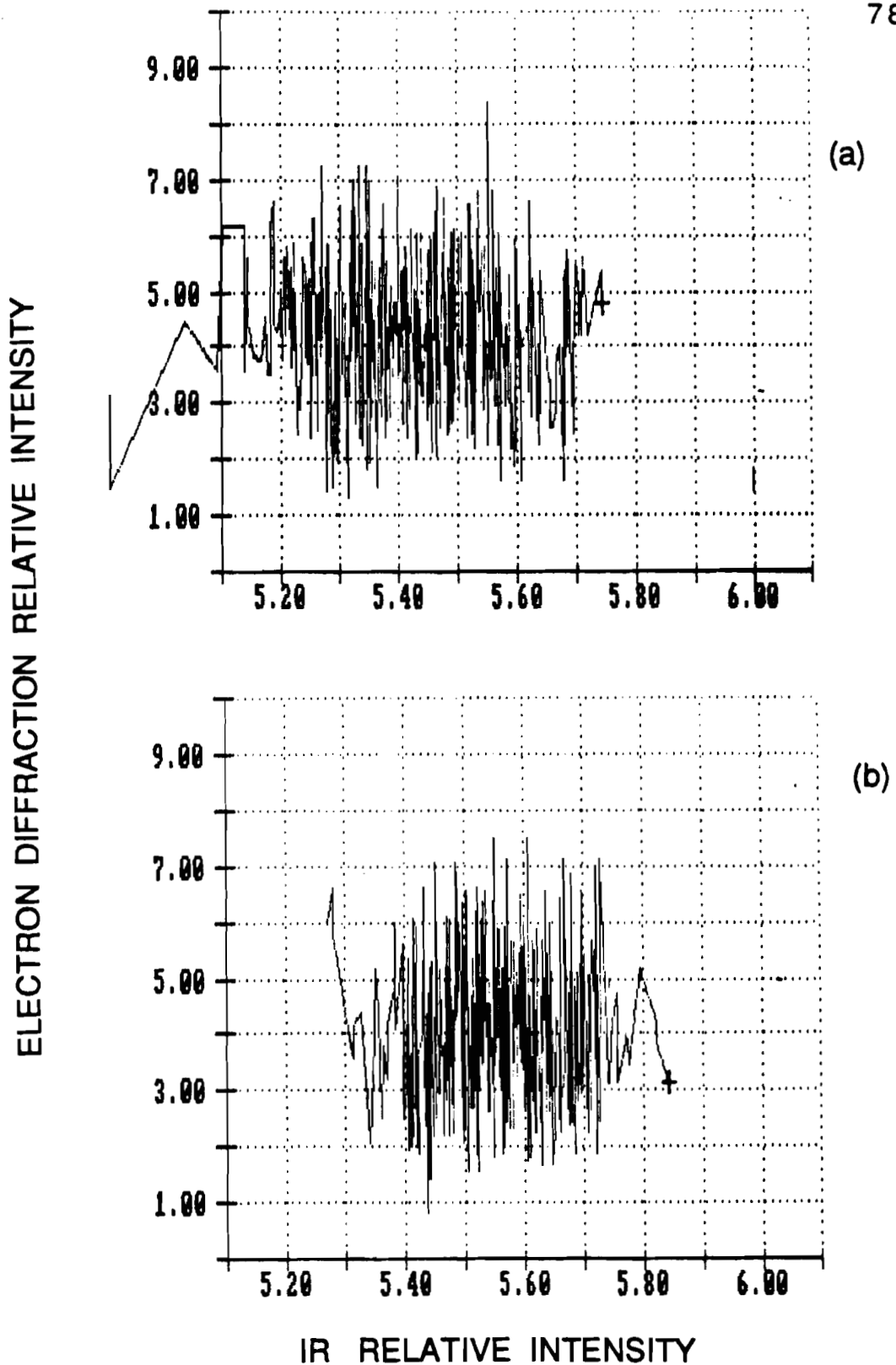
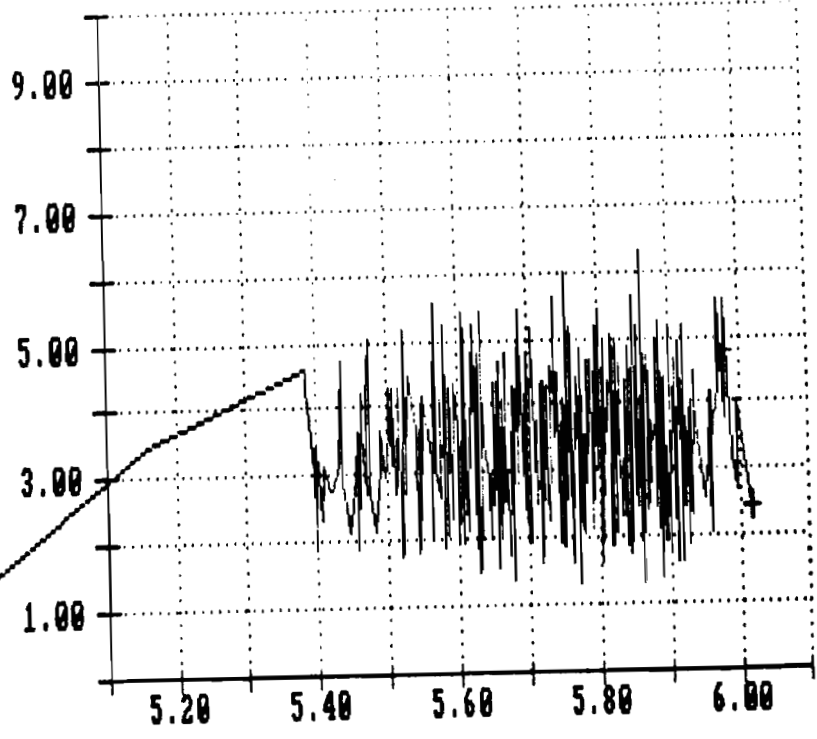
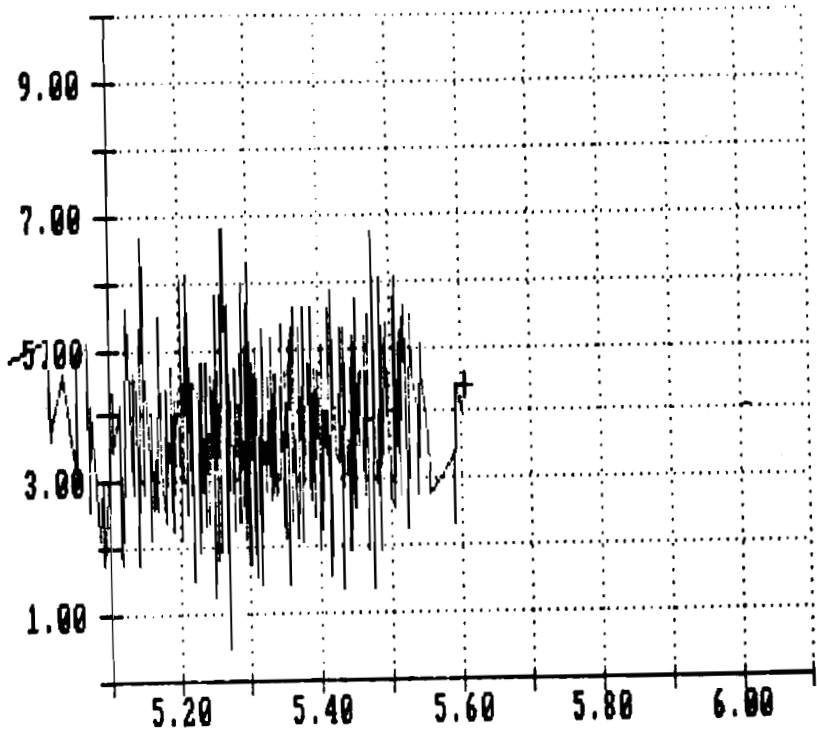


Fig. 2.27 The measured electron pulse intensity and the corresponding IR pulse intensity plotted for 4 runs of 500 samples. Both intensity scales are in arbitrary units. The center of the IR intensity distribution is different in each run because of long-term laser fluctuations. (see next page)

ELECTRON DIFFRACTION RELATIVE INTENSITY



IR RELATIVE INTENSITY

noise in the electron diffraction intensity, no correlation can be observed in the relationship between the electron diffraction intensity and IR intensity.

A diagram of the experimental arrangement for the computer-controlled data acquisition procedure is shown in Fig. 2.28. In order to monitor the laser output, a photoconductive detector DIODE1 was placed before the optical delay line to pick up a fraction of IR pulse. The IR monitor signal was sent to the first channel of the SR250 boxcar integrator. The second channel was used to integrate the output of the photomultiplier PMT which measures the electron diffraction intensity. The peak of the spectral response of the photomultiplier was about 350 nm. The gating of the two channels of the boxcar is triggered by a synchronization pulse from the laser system. The typical gate width was 50 ns for the IR pulse measurement and 150 ns for the electron diffraction intensity measurement. The data is stored in the computer in an array. The array is sorted according to IR intensity and only those data that fall within an specified IR intensity bracket are kept. This serves two important functions. First, it effectively reduces the fluctuations of the laser system to about 1-2 percent. Second, it improves the intrinsic resolution of our data since, without the sorting, the measured electron diffraction intensity is an average over the temperature range produced by the spread in the IR pulse energy. The data acquisition and analysis was performed using the ASYST scientific software package.

An important part of the experimental arrangement is the computer-controlled shutter placed in the path of the IR heating beam. The

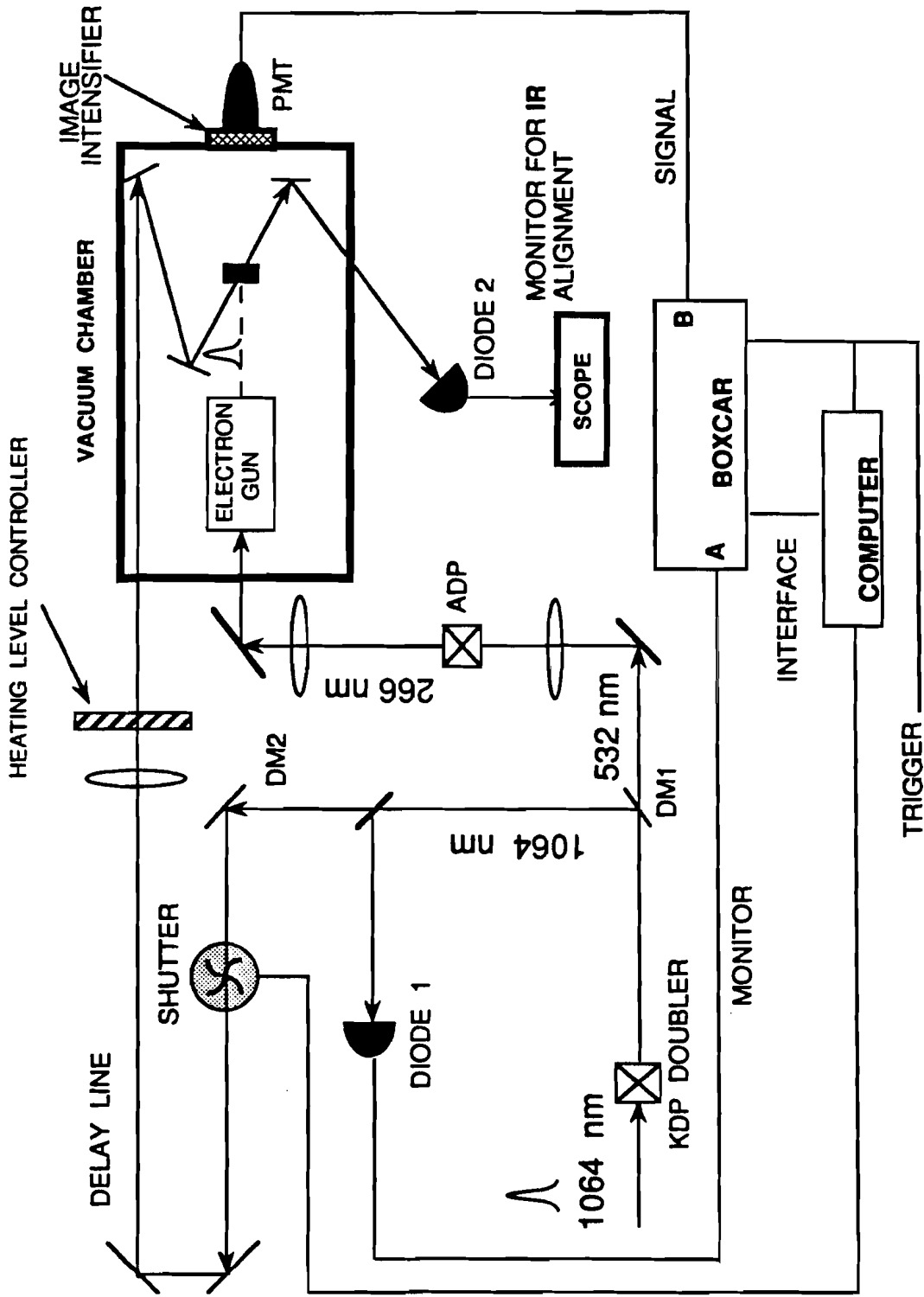


Fig. 2.28 Schematic of experimental arrangement using computer sorting and averaging. DM1 and DM2 are dichroic mirrors; PMT is a photomultiplier tube.

purpose of the shutter is to quickly alternate between measurements of a hot (shutter open) and a cold (shutter closed) specimen so that the measurements are taken at nearly the same time. This is to minimize experimental error due to long-term drift in the operating parameters of the equipment. This may result, for example, from the progressive deterioration of the photocathode, and temperature fluctuations and vibrations in the frequency-doubling crystals. Typically, it took 4-5 minutes to measure a single data point. The error due to drift within this time could be significant if not compensated for.

A flow chart of the experimental procedure typically followed in taking a single data point is displayed in Fig. 2.29. The shutter was opened to allow 200 single-shot measurements of the hot specimen. The shutter was then closed to allow 200 single-shot measurements of the cold specimen. This process was repeated, usually about 150 times, and the data taken was sorted and accumulated for averaging. The reason we chose to accumulate data in increments of 200 shots was that a larger increment resulted in reduced consistency.

Figures 2.30(a), (b), and (c) show the relative (220)-order time-resolved electron diffraction intensity, $I_{\text{hot}}/I_{\text{cold}}$ for three heating intensities corresponding to the three laser power densities of $P_1=0.66 \times 10^8$, $P_2=1.3 \times 10^8$ and $P_3=1.6 \times 10^8$ W-cm⁻², respectively. The brighter (220) order of the electron diffraction pattern was measured because it gave the best signal-to-noise ratio. The electron diffraction intensity I_{cold} was that measured

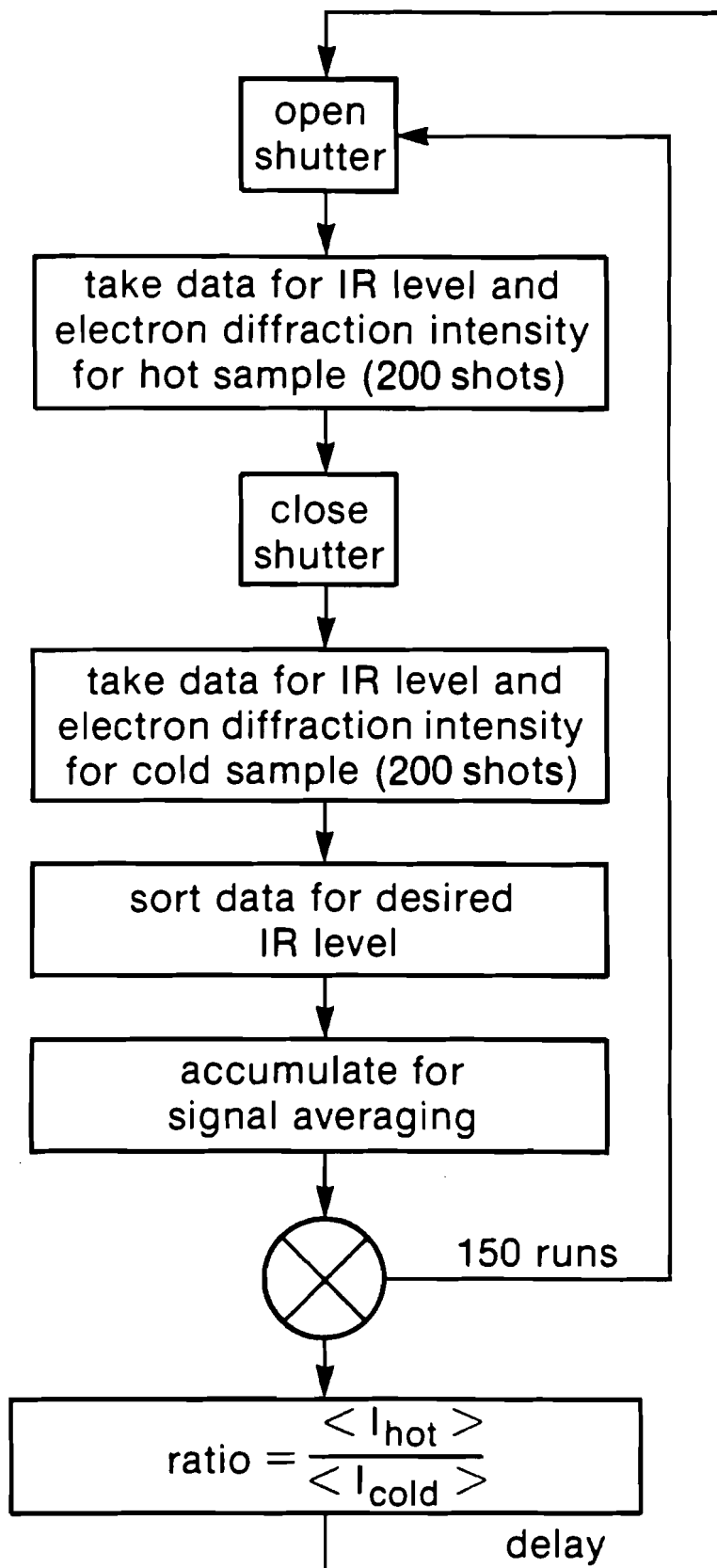


Fig. 2.29 Flow chart showing computer data acquisition procedure.

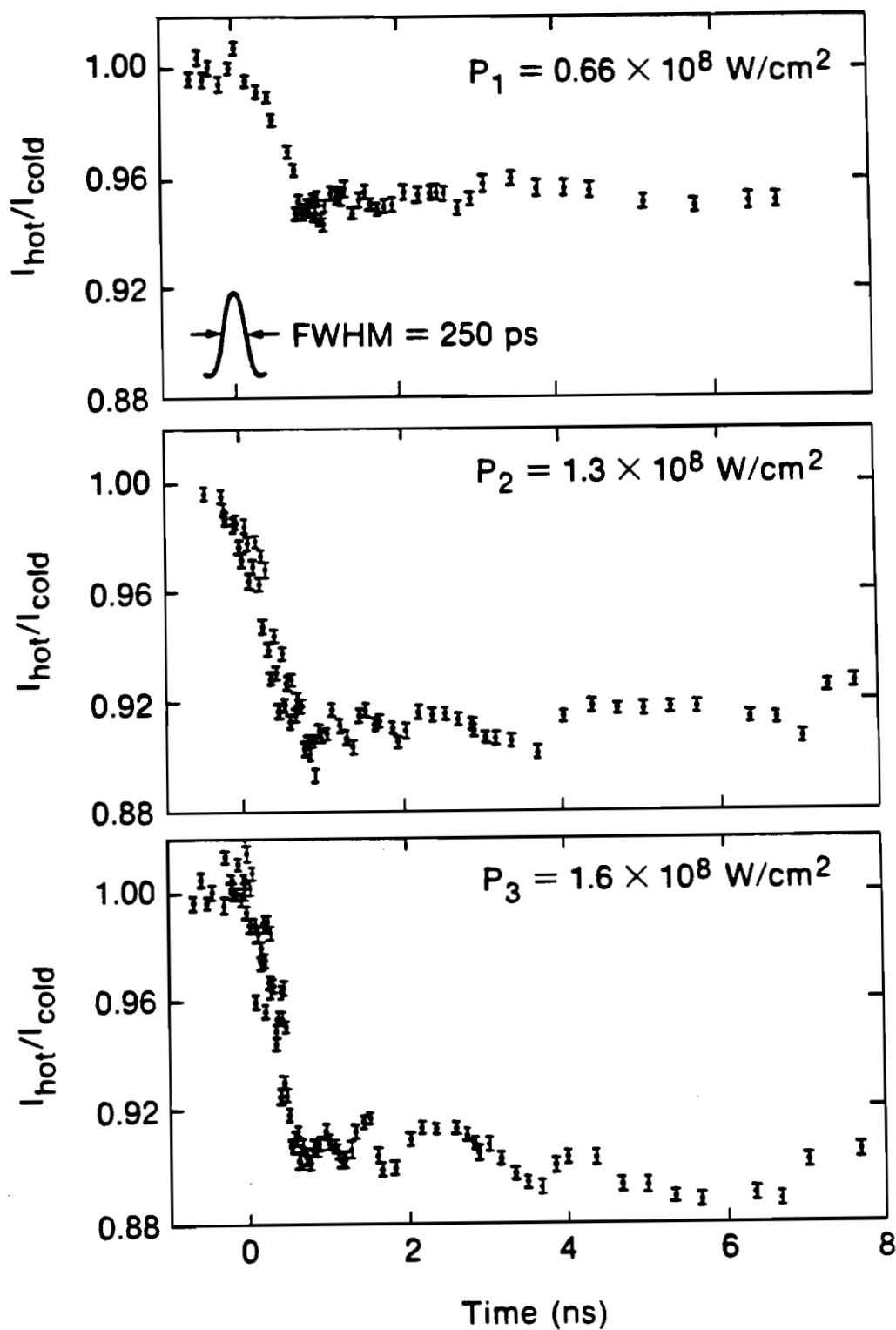


Fig. 2.30 The (220)-order normalized electron diffraction intensity for single-crystal gold as a function of probe delay for the three indicated laser power densities, the heating laser power density is indicated in each panel.

without laser irradiation, so I_{cold} is the electron diffraction intensity of the sample at room temperature. The electron diffraction intensity ratio, $I_{\text{hot}}/I_{\text{cold}}$, is unity in the absence of laser heating. The figures show not only the corresponding electron diffraction intensity changes for different heating levels but also an oscillatory structure. The oscillatory structure was also seen in the photographic image analysis of the electron diffraction intensities, but it is more evident here because of a greater number of data points and better experimental resolution. The number and the amplitude of the oscillations are more pronounced with increasing laser irradiance. The sharp initial decay is indicative of the rapid bulk temperature rise of the material. The initial decay time is about 500 ps, whereas the REGEN laser pulse width FWHM was 250 ± 25 ps. The figures show the results before background correction. The peak to peak error is about 0.5% while the change in $I_{\text{hot}}/I_{\text{cold}}$ due to laser irradiation was as high as 10%. Near $t=0$, there is an occasional anomalous rise in the intensity (see Fig. 2.30(a) and 2.30(c)) above I_{cold} which we cannot explain.

The oscillation superimposed does not agree with the predictions of the Debye theory. This unexpected outcome prompted us to investigate possible mechanisms responsible for this oscillatory behavior. Since the oscillatory structure was more pronounced at increasing laser heating power in terms of the amplitude and the number of oscillations, it was surmised that the

thermodynamic response of sample to the influence of laser irradiation was playing an important role. The interference between scattered electrons from different regions of the sample with different time-varying lattice constants can produce minima and maxima in electron diffraction intensity. The oscillation amplitude is about 2 percent for both of irradiating laser power densities P_2 and P_3 , respectively, and is 1 percent for P_1 . The oscillation rate in each case decreases continuously with increasing delay time which again may be associated with thermal relaxation processes within the sample.

2.5 SUMMARY

In summary, using an optical pump and electron probe we have obtained what we believe are the first quantitative time-resolved measurements of the electron diffraction intensity. Our measurements were of subnanosecond resolution, but it is feasible to extend our technique into the picosecond regime by using lasers with shorter pulse widths. We have developed two techniques for the acquisition and analysis of the electron diffraction intensity. One technique involves photographic imaging and digital image enhancement. The advantage of this technique is that the information on the whole diffraction pattern can be acquired and analyzed at the same time. The other technique used a boxcar interfaced with a personal computer. The computer enables us to control fluctuations in the laser and to reduce error due to drift in the operating parameters of the experimental equipment.

We have measured the time-resolved diffraction intensities of single-crystal and polycrystalline gold films under pulsed laser irradiation. The sharp decay in the electron diffraction intensity indicates an increase in the lattice temperature as a result of laser heating. We have also observed an unexpected oscillatory behavior in the intensity which we surmise is associated with thermal relaxation processes. The origin of the oscillations is investigated in the next chapter.

CHAPTER 3

DISCUSSION AND INTERPRETATION

3.1 BACKGROUND CORRECTION

In Chapter 2, it was found that the time-resolved diffraction intensity maxima of the Au exhibited an unexpected oscillatory behavior in time. The oscillations are superimposed on a decay which appear to correspond with the expected Debye-Waller effect, namely, a decrease in intensity with temperature rise. The oscillations are particularly evident in the computer-interfaced boxcar measurements of the (220) diffraction order. In this Chapter we analyze these results and explore some possible mechanisms that may provide an explanation for these oscillations. However, in order to proceed with our analysis, we must first remove the background contribution to the (220)-order diffraction intensity.

The measurement of the (220) diffraction intensity on the phosphor screen image was performed using a photomultiplier in conjunction with a mask containing a hole with a radius of 1 mm that was centered over the diffraction spot. To correct for the background, the measured signal is assumed to consist of a diffraction spot with a Gaussian profile superimposed on a constant background that is uniform over the hole in the mask. The background has two major sources, thermal diffuse scattering (TDS) and

noise in the microchannel plates (MCP), neither of which are expected to vary significantly over the dimension of the hole. The relative intensity of the background to the total signal can be estimated by making use of the lineout of the (220)-diffraction peak at room temperature in Fig. 3.1. By separately integrating the gaussian diffraction peak and the thermal diffuse background over the aperture, we estimated that the thermal diffuse background comprises approximately 40 percent of the total signal at room temperature. For simplicity we now assume that the background level remains constant under laser heating in order to make our background correction. This is not strictly true since the loss in diffraction maxima intensity due to laser heating goes to increase the thermal background. The increase in the background level can be seen in the lineouts shown in Fig. 2.21, but it is very small and we shall neglect it. Figure 3.2 show the background corrected relative time-resolved intensities $I_{\text{hot}}/I_{\text{cold}}$ of the (220) order of gold for the three laser power densities $P_1=0.66 \times 10^8$, $P_2=1.3 \times 10^8$, and $P_3=1.6 \times 10^8$ W/cm². To obtain these data, the background was subtracted from the raw data of Fig. 2.32 and then rescaled so that $I_{\text{hot}}/I_{\text{cold}}$ is unity at room temperature. The overall effect of the background correction is to accentuate the initial decay and to increase the amplitude of the oscillation.

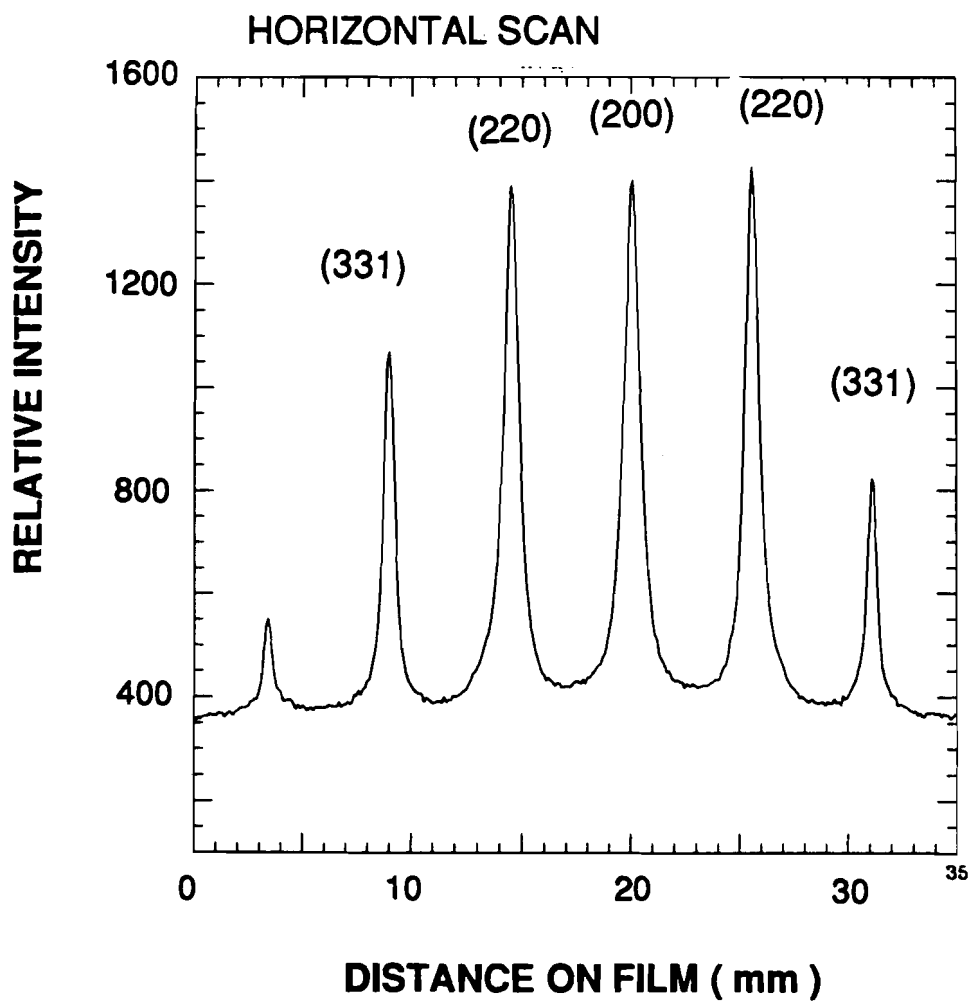


Fig. 3.1 The lineout of the diffraction intensity for single-crystal gold at room temperature used in the background correction.

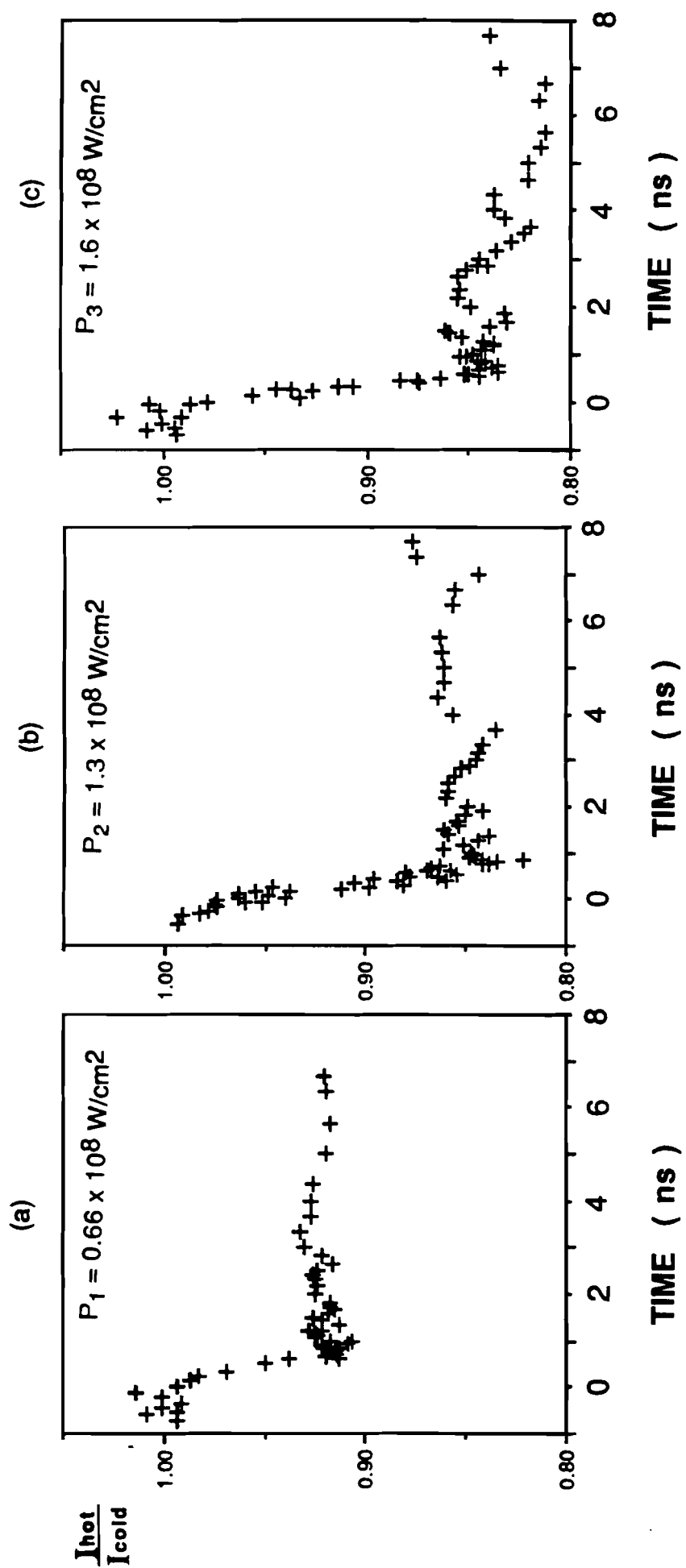


Fig. 3.2 The background-corrected (220)-order normalized electron diffraction intensity (from Fig. 2.30) for single-crystal gold as a function of probe delay for the three indicated laser power densities. The data have been rescaled so that the normalized intensity is unity without laser heating

3.2 MECHANISMS OF OSCILLATIONS

We have noted that our observed oscillations in the experimental results shown in Fig. 3.2 is at odds with the monotonic-curve expectation of the Debye-Waller theory. We have considered several mechanisms to explain the observed oscillations. These include bulk phenomena such as laser-induced shock-wave modulation, membrane or thin plate vibration, and temperature gradients in the sample and surface phenomena such as enhanced surface heating and surface plasmon formation.

(a) Shock waves

Laser-induced shock waves in metals and their formation mechanisms were first proposed in 1963 by Askaryon and Morez and explored by other workers.¹⁻³ It was suggested that a high-intensity laser pulse can produce recoil pressure pulses on metal surfaces due to vaporization and induce surface shock waves. This effect was verified for either confined surfaces,⁴⁻⁶ i.e. surfaces covered by suitable transparent overlay, or unconfined surfaces⁷⁻⁹ of metals. The significance of the confined configuration is that the vaporized materials stayed near the metal surface and increased the peak pressure developed during the laser irradiation considerably and thus enhanced the density of shock waves. The surface shock waves then propagate into the bulk and are presumed to attenuate exponentially. The propagation speed is of the order of sound speed in the media. The highly localized thermal expansion due to the short and intense laser pulse

irradiation are considered as the origin of shock deformation of metal surfaces. We do not, however, believe that the shock wave mechanism provides an adequate explanation for the oscillations in our data. The sound speed in gold film is in the order of few nanometers per picosecond. Therefore the shock-wave modulation is extremely fast with a propagation time on the order of tens of picoseconds through a 25 nm-thick gold film. The shock wave mechanism is thus too fast to produce the comparatively slow oscillations observed. In addition, shock wave formation is accompanied by vaporization and damage to the material. No such permanent damage to the Au sample was observed in our experiments.

(b) Normal mode vibrations

A very thin free standing film is a thin plate that vibrates when a laser pulse is applied. We consider thin plate vibrations rather than membrane vibrations in our model. The essential difference between thin plate vibrations and membrane vibrations is that in a membrane the restoring force is entirely due to the stretching tension whereas in a thin plate the force is due to the stiffness of the material. Our sample preparation technique does not put appreciable tension in the film. For a circular thin film with radius r_c , the fundamental frequency of vibration is given¹⁰ as

$$f_1 = 0.47 \frac{d_c}{r_c^2} \sqrt{\frac{Y_m}{\rho (1-\psi^2)}} \quad 3.1$$

where d_c is the thickness of the film, Y_m is Young's modulus, ρ is the volume density of material in kilograms per cubic meter, and ψ is its Poisson's ratio.

Poisson's ratio is the negative of the ratio of the lateral strain $\partial\zeta/\partial z$ to the longitudinal strain $\partial\varepsilon/\partial x$. The negative sign in the definition is to ensure that ψ be a positive number since a positive longitudinal strain of tension is always accompanied by a negative lateral strain of compression. The fundamental frequency f_1 for the 25 nm-thick gold film with radius 0.25 mm is calculated to be about 400 Hz. This vibrational frequency is far too low compared with the oscillations observed in time-resolved electron diffraction intensity profile. Higher order modes are also ruled out because of the seemingly regular oscillations observed in the experimental results--the density of the higher modes would preclude well defined oscillations.

(c) Temperature gradients

Differential thermal expansion due to the laser-induced temperature gradient in the sample was investigated in order to examine its effect on the electron diffraction intensity. The mean free path, i.e., the skin depth in metals for visible and near infrared laser radiation, is about ten nanometers. Therefore, only a very thin surface layer is directly heated by the laser. In addition, if the laser beam is of sufficiently short duration, the laser energy deposition rate could be so rapid that the heating rate exceeds the thermal

diffusion time within the sample. Under these conditions, it is possible to have a large temperature gradient with very high surface temperatures. In some cases, the surface of a material heated by a short pulsed laser can vaporize without going through melting. Therefore, the thermal vibrational amplitudes and lattice constants are expected to vary within the sample because of the temperature gradient. Different regions on the sample will have different Debye-Waller factors and different lattice constants. When the lattice constant changes from layer to layer because of a temperature gradient, the scattered electrons from these layers cannot be in phase and will give rise to interference. Relaxation of the temperature gradient could then cause oscillations in the time-resolved electron diffraction intensity. This possibility will be considered in a thermal diffusion model calculation in the next section.

(d) Surface expansion

The thickness of the gold film is about 25 nm. In a thin sample, the surface atoms form a significant fraction of the total number of atoms and may influence experimental results in a way that is not normally observed for the bulk material. The observed oscillations may be due to interference between the scattered electrons from the surface and from the bulk. Surface atoms are more loosely bound and have larger vibrational amplitudes giving rise to a larger temperature effect. Moreover, we note that the interlayer spacings between the top few surface layers, in general, are significantly larger than the bulk spacings,¹¹ that is, the lattice in the surface region is distorted and has a

different thermal expansion coefficient. Surface oxide, impurities, defects, and excitations may increase the coupling with photons and cause enhanced surface heating. Evidence of surface heating due to surface-plasmon-enhanced absorption has been investigated by Musal.¹² Surface plasmons are coherent fluctuations of electrons on a metal surface. Their existence has been confirmed in electron energy loss experiments by Powell and Swan¹³ after surface plasmons were first suggested by Ritchie.¹⁴ More recently, transient optical reflectivity measurements¹⁵ have confirmed the dense surface plasma formation under laser irradiation. Surface plasmon formation on metal mirrors is believed to lead to enhanced thermally induced surface damage.

3.3 THERMAL DIFFUSION MODEL

(a) Pulsed-laser heating

In this section we use a thermal diffusion model to simulate the time-dependent temperature distribution induced by the laser in the Au sample and calculate the corresponding electron diffraction intensity. The basic dominant effect of laser irradiation in semiconductors and metals is believed to be heating and melting processes.¹⁶ The temperature rise induced by the laser pulse therefore can be simulated by using a thermal diffusion equation with appropriate initial and boundary conditions. The mathematical description of laser heating used here is volume heating which is based on the laser energy absorbed by a layer of thickness up to the

absorption depth. The volume heating model and the surface heating model have been discussed by Bechtel.¹⁷ In the surface model the absorption coefficient is taken to be infinity or, equivalently, the absorption length is assumed to be zero. The physical meaning is that the laser energy is coupled to the irradiated surface. The surface model is mathematically simpler than the volume model. However, the surface model of heat generation is not valid when the thermal diffusion length for the laser pulse duration is comparable to or less than the absorption length as is the case here. Most of the calculations on laser heating are based on conventional macroscopic diffusion equations with a finite-difference formulation¹⁸ so that the space, time, and temperature dependence of various physical parameters such as the thermal diffusivity, specific heat, optical absorption coefficient, etc., can be included in the laser heating model. However, for metals, the temperature dependence of the absorption coefficient and the reflectivity may be neglected since they change less dramatically (than for semiconductors) for the temperature range we are interested in. The thermal diffusivity is less sensitive to the temperature except near phase transitions. It should be noted that when phase transition occurs, the latent heat should be included in model calculations.

The computation of laser-induced temperatures is very complex in general because it involves the material properties and optical parameters which often are unknown. The initial and boundary conditions may not be necessarily linearly coupled to the spatial and temporal variables. Fortunately

some approximation can be made for the specific case here so that the calculation procedure can be simplified.

When there is no melting or vaporization involved during pulsed laser irradiation, a heat conduction differential equation with a source term representing the heat absorbed by the material from the laser can be applied.

The relevant thermal diffusion equation is

$$\nabla \cdot [K \nabla T(\vec{r}, t)] + A(\vec{r}, t) = \rho C \frac{\partial T(\vec{r}, t)}{\partial t} \quad 3.2$$

where K is the thermal conductivity, $T(\vec{r}, t)$ is the time-dependent temperature rise distribution in the material, $A(\vec{r}, t)$ is the source term due to laser irradiation, ρ is the density, and C is the specific heat capacity.

For a laterally large irradiating beam traveling in the z -direction and incident on a target surface in the xy plane, a one-dimensional thermal conduction equation can be used. The laser intensity has a gaussian profile in both of time and space with $1/e$ radii r_p and pulse width t_p , respectively. In the material, the laser is exponentially attenuated with an absorption coefficient α . The thermal conductivity K and specific heat per unit volume ρC of the solid can be taken to be constant over the temperature range of interest. Radiative heat loss from the surfaces is negligible (about 1 K per nsec for a surface temperature of 1000 K) in the time scale of the experiment (<10 ns). Appropriate boundary conditions and initial conditions must be specified in

order to solve the heat diffusion equation. Some approximations may be made to arrive at an analytical solution. The initial temperature rise distribution is

$$T(z, t=0) = 0 \quad 3.3(a)$$

where $T(t, z)$ in Eq. (3.3(a)) is the temperature increase above the room temperature T_0 . The final temperature distribution resulting from laser heating can be calculated using

$$T_f(t, z) = T(t, z) + T_0 \quad 3.3(b)$$

In our model we assume that the film is of infinite extent in the radial direction. This is an acceptable approximation since heat conduction through the edges affects only a negligible fraction of the extremely thin metal film on the time scale of interest. For all times, we have the boundary conditions

$$\left. \frac{\partial T}{\partial z} \right|_{z=0, L} = 0 \quad 3.4$$

Equation (3.4) implies that there is no heat loss through the surfaces. The source term representing heat produced by the laser is given by

$$A(z, t) = I_m [1-R] \alpha \exp[-\alpha z] p(r)q(t) \quad 3.5$$

where I_m is the maximum incident irradiance, R is the reflectance for the irradiating laser wavelength, α is the absorption coefficient, $p(r)$ is the lateral

distribution of laser irradiance, and $q(t)$ is the temporal dependence of laser irradiance. A simplifying assumption that we make here is that $p(r)$ is unity, that is, the the sample is uniformly irradiated. This approximation is justified since the IR beam diameter is much larger than the size of the specimen. A major advantage of this approximation is that we can now use a one-dimensional diffusion equation to model the laser heating of the specimen. A gaussian distribution was used for the temporal profile of the irradiating laser beam, that is

$$q(t) = \exp[-(t/t_p)^2] \quad 3.6$$

The solution of the thermal diffusion equation Eq. (3.2) for this set of boundary conditions is given by

$$T(z, t) = \int_{t=0}^t dt' \int_{z'=0}^z dz' G(z, t | z', t') \frac{A(z', t')}{\rho C} . \quad 3.7$$

The Green's function $G(z, t | z', t')$ is the solution of the one-dimensional differential equation

$$\nabla^2 G + \frac{1}{K} \delta(z - z') \delta(t - t') = \frac{1}{D_T} \frac{\partial G}{\partial t} , \quad 3.8$$

where D_T is the thermal diffusivity. The one-dimensional Green's function satisfying the boundary and initial conditions can be expressed as

$$G(z, t | z', t') = \sum_{n=0}^{\infty} W(n) \cos(\eta_n z) \cos(\eta_n z') \exp[-\eta_n^2 D_T (t - t')]$$

$$\eta_n = n\pi/L \quad n = 0, 1, 2, \dots$$

$$W(n) = \begin{cases} 1/L & n = 0 \\ 2/L & n = 1, 2, 3, \dots \end{cases} \quad 3.9$$

where $W(n)$ is a weighting factor. A closed expression for the laser-induced temperature rise $T(z, t)$ can be obtained in terms of the error function $\text{erf}(x)$,

$$T(z, t) = \frac{1}{\rho C} I_m (1 - R) \sqrt{\frac{\pi}{4}} t_p \sum_{n=0}^{\infty} \frac{\alpha^2}{\alpha^2 + \eta_n^2} W(n) F_z(n) F_t(n)$$

$$F_z(n) = [1 - \exp(-\alpha L) \cos(\eta_n L)] \cos(\eta_n z)$$

$$F_t(n) = [1 + \text{erf}(\frac{t}{t_p} - \frac{\chi_n}{2})] \exp[-\chi_n (\frac{t}{t_p} - \frac{\chi_n}{4})]$$

$$\text{where } \chi_n = \eta_n D_T t_p. \quad 3.10$$

The simulated laser-induced surface temperatures of a thin 25-nm-thick gold film for the three laser power densities, P_1 , P_2 , and P_3 , respectively, are shown in Fig. 3.3. A constant absorption coefficient $\alpha = 1 \times 10^6 \text{ cm}^{-1}$ for gold and a laser pulse duration of 250 ps were used. The thermal diffusivity for bulk-gold at room temperature is $1.255 \text{ cm}^2/\text{s}$. The final predicted temperatures ranged from 400 K to 560 K. The largest temperature gradient in the sample occurred at approximately $t=0$. Figure 3.4 shows the temperature gradient at $t=0$ for the highest laser power density P_3 . The

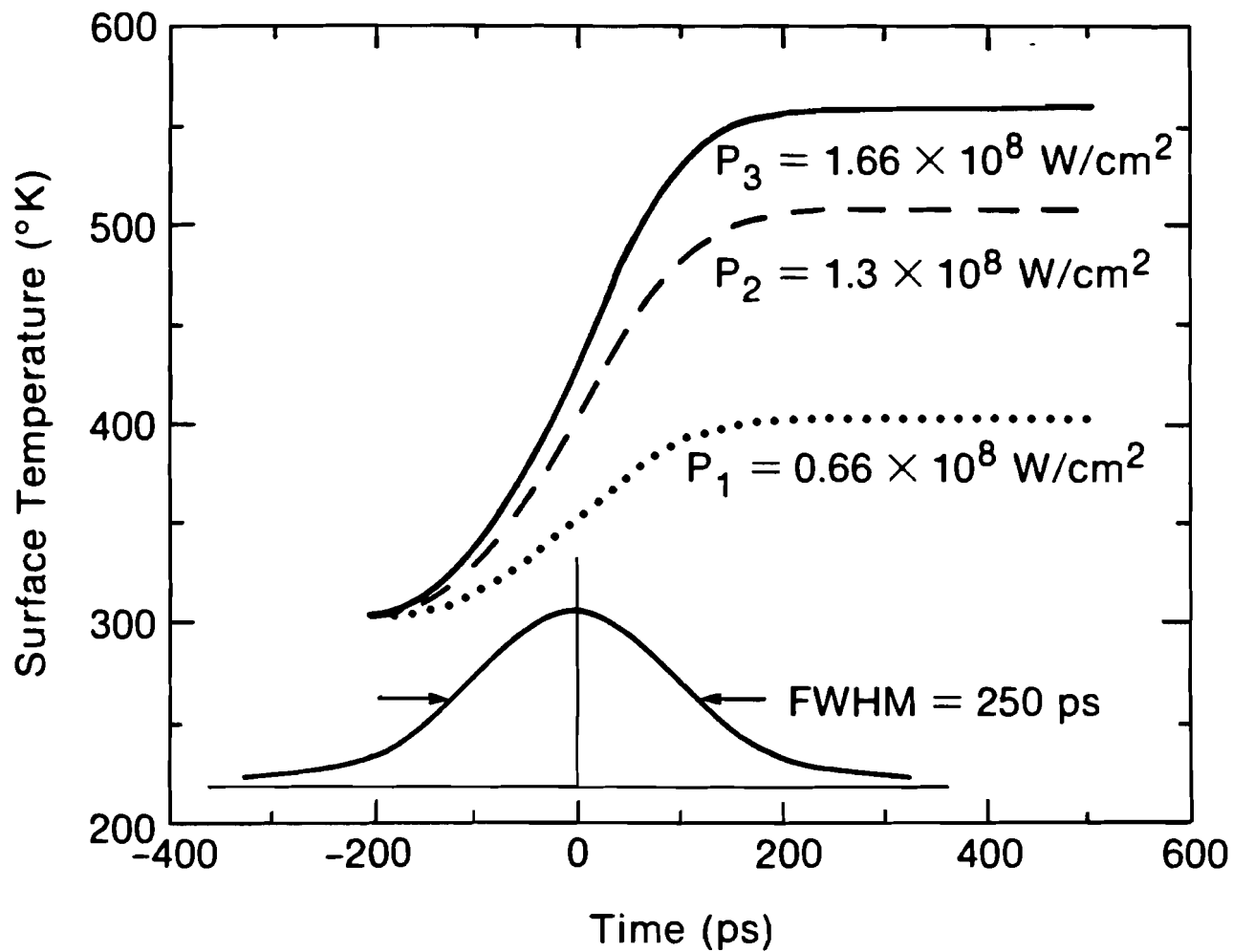


Fig. 3.3 The surface temperature of a laser-heated 25-nm thick gold sample as a function of time calculated using the thermal diffusion model described in the text. The pulse width and the power densities of the heating pulse are indicated.

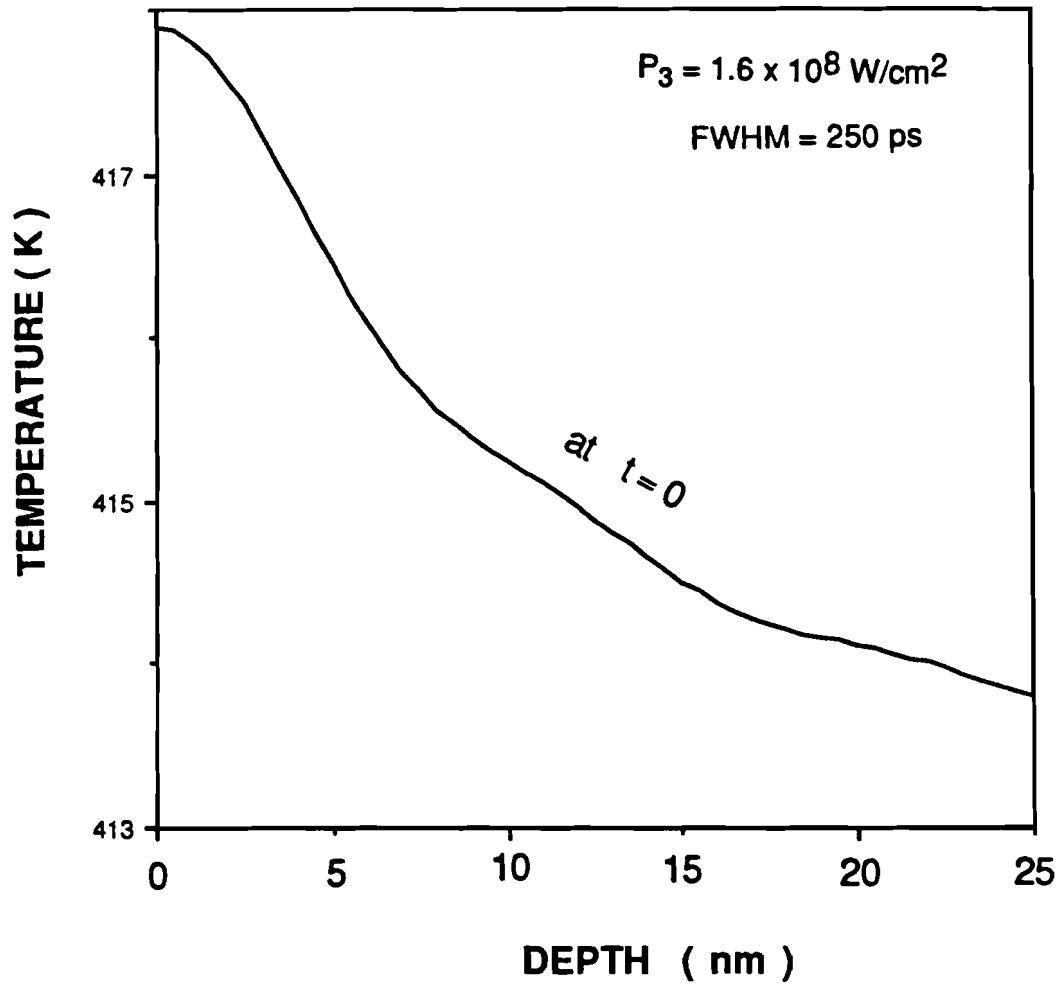


Fig. 3.4 The temperature of a laser-heated 25-nm thick gold film as a function of its depth at $t=0$ calculated using the thermal diffusion model. The laser power density and the pulse width are as in Fig. 3.3.

temperature difference of the front and the back surfaces is only about 5 K. The theoretical calculation shows that, because the sample is so thin, thermal equilibration takes place during the pulse and equilibration is essentially complete at the end of the pulse. The thermal diffusion length for a 250-ps pulse is about 300 nm. This is much larger than the sample thickness. In other words, no significant temperature gradient will develop unless the thermal diffusivity is much smaller.

(b) Temperature conversion

Given the temperature of the sample as a function of time, we can calculate the time-dependent electron diffraction intensity using the Debye-Waller factor for gold. This requires a reliable value for the Debye-Waller factor which we were unable to measure because of outgassing problems in our apparatus at high temperatures, a problem not encountered during the very brief localized heating by the laser pulse. We can, however, look at published values. The steady-state temperature dependence of electron diffraction intensities in metals has been investigated by several research groups. Experimental values of β (defined in Eq. (2.2)) for the (220)-order of gold are listed in Table 3.1. Except for the cases in which the size effect²¹⁻²³ (large surface atomic vibrational amplitude) or anharmonicity¹⁹⁻²⁰ at very high temperature must be taken into account, the values are in good agreement, better than within an order of magnitude, with

Table 3.1. Temperature factors for the (220)-order electron diffraction from gold. Here β is the factor defined in Eq. 2.2, T is the peak temperature attained in our experiment at intensity I(P3) as predicted by the corresponding temperature factor. The T value 560 K listed under "present work" was calculated by the thermal diffusion model.

	β [10^{-4} K $^{-1}$]	T [K]	notes	references
Debye [Eq. (1)]	4.58	760	harmonic approx.	
Owen & Williams;				
			X-ray single crystal	22
			300-1000 K	
Gupta	harmonic: 4.35 anharmonic: 5.37	785 692	theoretical analysis	23
Buffat	5.0	720	50 keV ele.-diff. 300-600 K	21
Kovalenko et al	small particle(9 nm-dia): 6.36-6.78 large particle(>10.5 nm): 5.4	610-630 690	50 keV ele.-diff. size effect 20-90 K	19
Solliard et al	small particle(5-10 nm): 5.2-6.16 large particle(>15 nm): 4.88	640-700 732	HEED. powder, 3-15 nm-dia size effect 130-600 K	20
Niedrig et al	theoretical: 15 experimental: 13	440 460	26 keV elec.-diff. thickness=25 nm 77 K & 300 K	24-26
present work	13 8.1	460 560	25.5 keV elec.-diff. thickness = 25 nm laser-induced	

the Debye value $4.58 \times 10^{-4} \text{ K}^{-1}$. Various X-ray diffraction results²² were analyzed by Gupta²³ and the values in the harmonic approximation and with an anharmonic correction are listed in Table 3.1 for comparison. We noted that Niedrig *et. al.*²⁴⁻²⁶ obtained a larger value for β . They attributed this discrepancy to the dynamical effects of electron diffraction. The limitations of the Debye-Waller theory are discussed more fully in Appendix B with particular emphasis on dynamical effects.

(c) Time-resolved temperature results

We have chosen to use the β value given by Niedrig *et. al.*²⁴ to convert our experimental time-resolved electron diffraction intensities into temperatures because their experimental conditions (26 keV in electron energy and 25 nm film thickness) most closely resemble ours. The resulting temperature values plotted as a function of probe delay, are shown in Figs. 3.5-3.7 with the incident surface temperatures calculated from our thermal model for the three laser fluences. As we have noted, the surface temperatures do not differ significantly from the bulk temperature in our model simulation. We estimate from the data that the maximum laser-induced bulk temperature rise from room temperature for the three laser fluences were 75, 155, and 160 K, respectively. In Figs. 3.5-3.7 the error in the determination of these numbers is estimated to be $\pm 20\%$. The maximum temperatures T obtained experimentally are therefore 375, 455, and 460 K for the respective

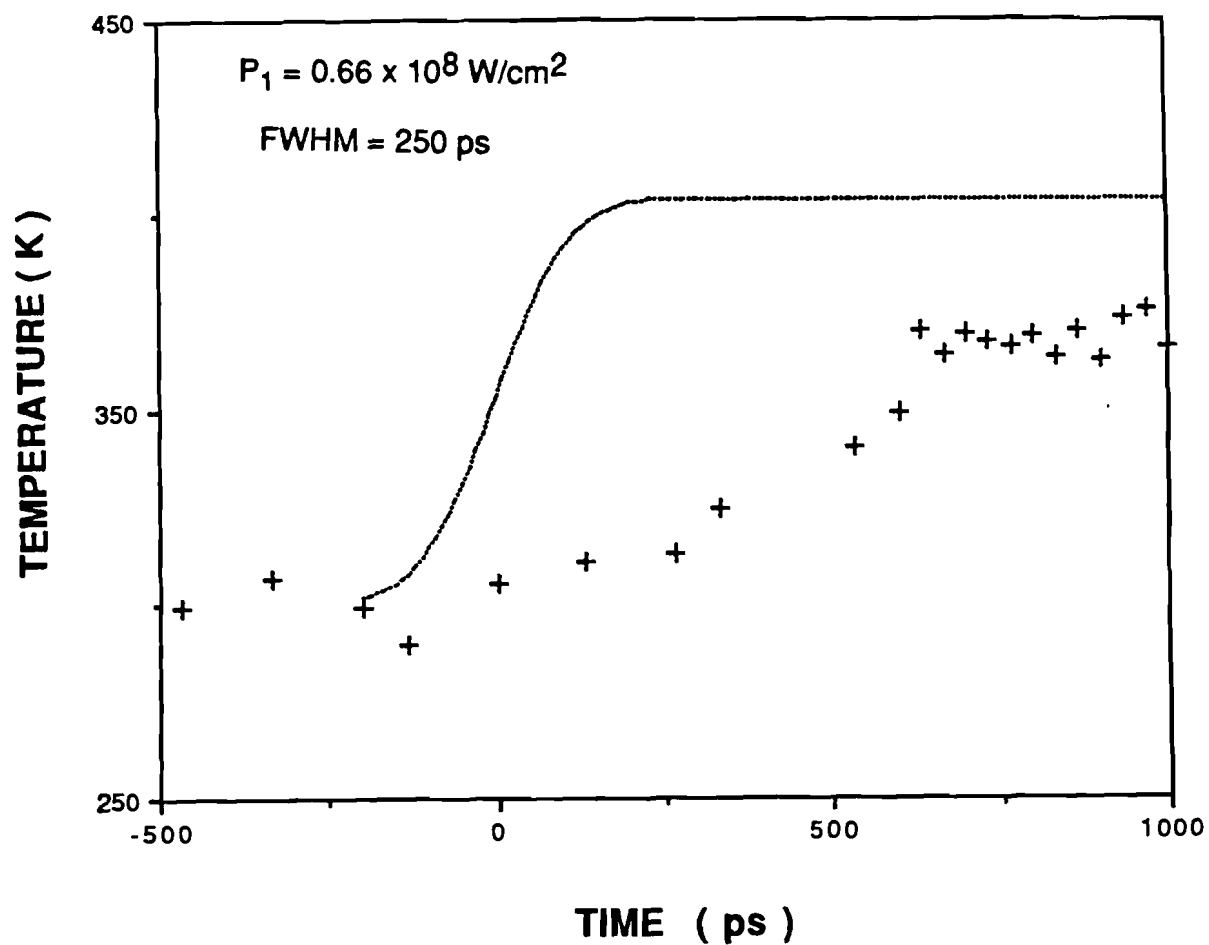


Fig. 3.5 The time-dependent temperature extracted from the time-resolved electron diffraction intensity data given in Fig. 3.2(a) for single-crystal gold. The dashed line is the calculated from the thermal diffusion model and the crosses are the experimental points.

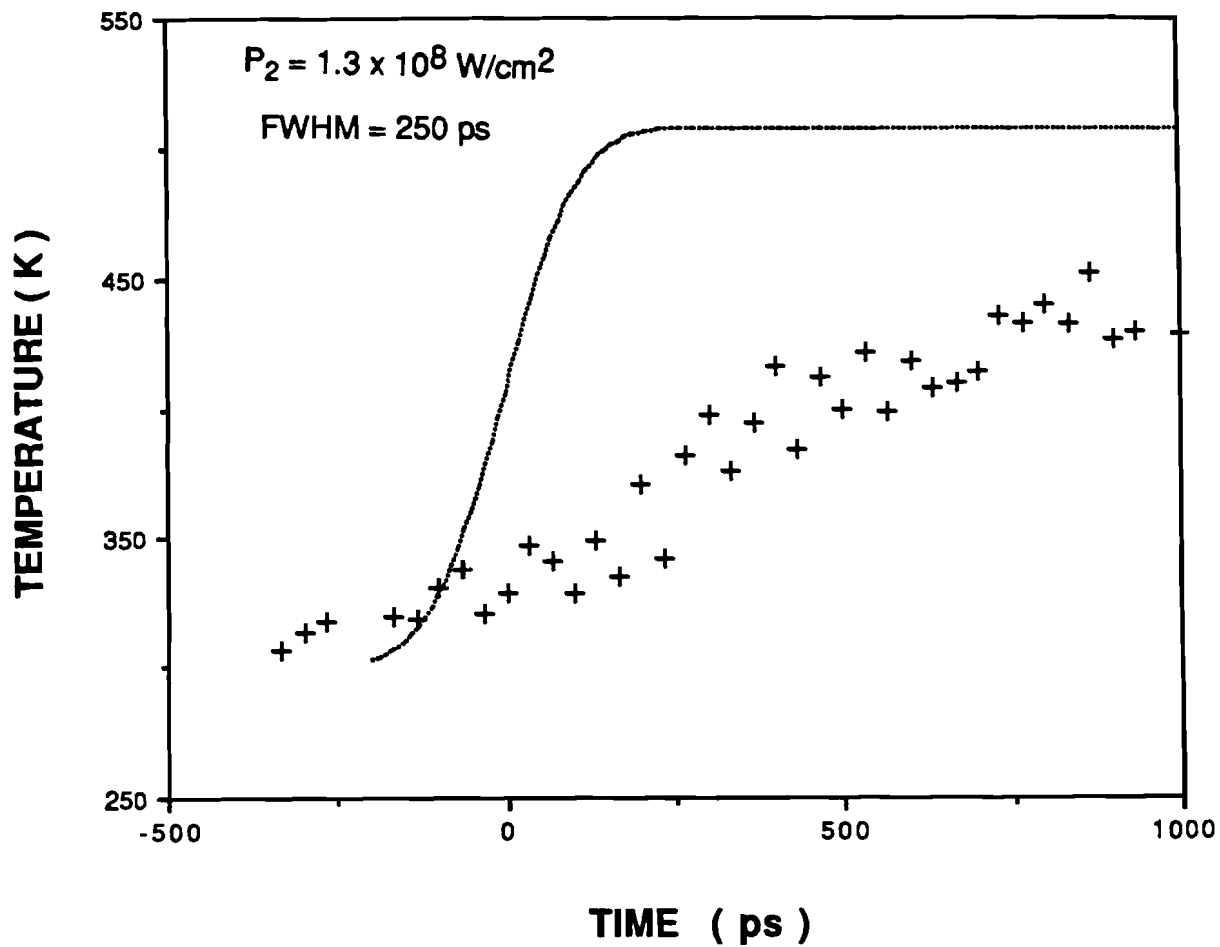


Fig. 3.6 The time-dependent temperature extracted from the time-resolved electron diffraction intensity data given in Fig. 3.2(b) for single-crystal gold. The dashed line is the calculated from the thermal diffusion model and the crosses are the experimental points.

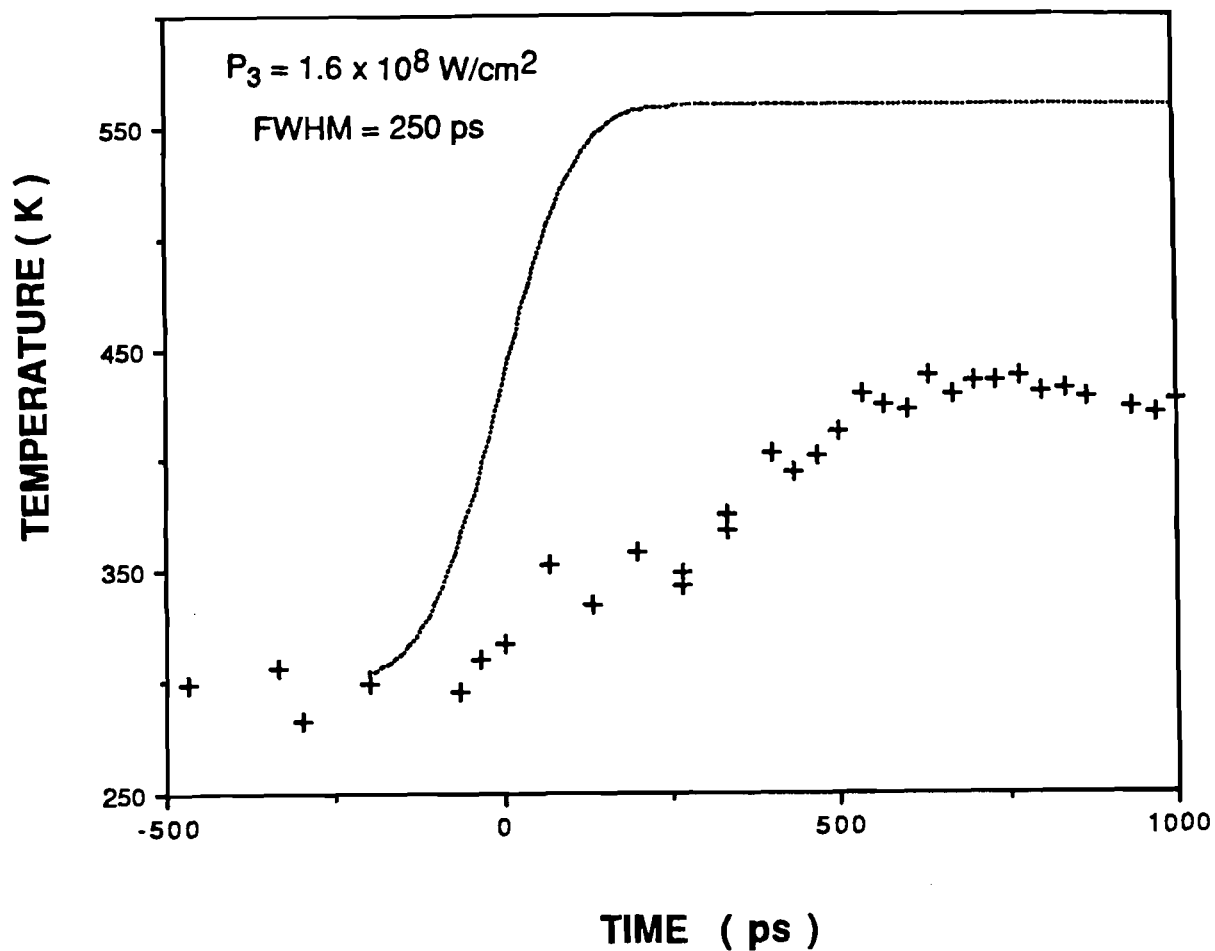


Fig. 3.7 The time-dependent temperature extracted from the time-resolved electron diffraction intensity data given in Fig. 3.2(c) for single-crystal gold. The dashed line is the calculated from the thermal diffusion model and the crosses are the experimental points.

laser fluences for the β value of Niedrig *et. al.*. The values for the final temperature produced by the laser power density P_3 calculated using other reported experimental values of β are listed in Table 3.1 for comparison. The model-calculated maximum bulk temperatures corresponding to the three laser heating levels were found to be 400, 500, and 560 K, which are higher than the temperatures extracted from the experimental data by about 20%. At the same time, they are consistently lower than those we might predict from the use of a Debye-theory temperature factor. As noted in Table 3.1, the appropriate value of β which would have predicted these values is $8.1 \times 10^{-4} \text{ K}^{-1}$. We believe that our Albrecht-Niedrig calibration underestimates the temperature rise, if anything, since the criterion for anomalous transmission may not be as well satisfied as in their case. It was pointed out²⁴⁻²⁵ that the value given by their theory,²⁶ which agreed with their experiment, is likely to give an upper limit for the temperature factor under more general circumstances. We note that in Figs. 3.5-3.7 the duration (about 500 ps) of the temperature rise is slower than the 250 ps that the thermal model predicts. The longer rise time in the experimental curve may represent the electron-phonon energy transfer time.

(d) The temperature-gradient effect

We have seen that, according to our thermal model simulation, only a very small temperature gradient (about 1 K/nm) develops within the sample.

This seems to preclude the temperature gradient as an explanation for the oscillations. However, this conclusion may be premature because we used an extremely simple model. There may be some unanticipated phenomena present in thin films that may result in a larger than expected temperature gradient. Therefore, we have created an artificially large gradient by assuming a small thermal diffusivity and calculated the resulting electron diffraction intensity using a modified Debye-Waller expression. The temperature-dependent atomic scattering amplitude a_g as a function of time t for electrons for a crystal of N atoms is

$$a_g(T,t) = N \sum_s f_s \exp[-i \vec{g} \cdot \vec{r}_s(T,t)] \langle \exp[-i \vec{g} \cdot \vec{u}_s(T,t)] \rangle \quad 3.11$$

Where f_s is the atomic structure factor of the atom at \vec{r}_s , \vec{g} is the reciprocal lattice vector which determines the possible electron beam reflections, $[\vec{g} \cdot \vec{r}_s(T,t)]$ is the phase factor when the diffraction condition is satisfied, and $\vec{u}_s(T,t)$ is the thermal displacement of the atom fluctuating in time. In the usual Debye-Waller model the time-averaged term $\langle \dots \rangle$ is the same for all atoms. The differential thermal expansion in the normal direction will cause different interplanar spacings, which contributes a phase factor ϕ among the scattered electrons. For the j th atom, the phase factor is

$$\phi_j = 4\pi r_j \frac{\sin \theta_B}{\lambda} \epsilon T(t,z) , \quad 3.12$$

where ε is the linear thermal expansion coefficient. The scattering intensity can then be expressed as

$$I = \sum_m \sum_n F_n(hkl) F_m^*(hkl) \exp[-i(\phi_n - \phi_m)] \exp[-(M_m + M_n)] \quad 3.13$$

where M is the Debye-Waller factor defined in chapter 1, and F is the structure factor. For a face-centered cubic crystal, F is equal to $4 f_e$, where f_e is the atomic scattering factor for electrons. By summing over all atoms or integrating over the sample depth z , the intensity as a function of time can be obtained. If there were no temperature gradient, then all the values of ϕ would be identical. The intensity can be written as

$$I = I_0 \exp(-2M), \quad 3.14$$

where I_0 is the diffraction intensity at the absolute zero temperature for a perfect crystal. This is identical to the Debye-Waller expression.

Figure 3.8(b) shows the calculated time-dependent electron diffraction intensity for 25-nm Au film that is the result of a large artificial temperature gradient. A calculation using the thermal diffusion model for the laser-induced temperature profile was carried out first and then the corresponding electron diffraction intensity was simulated using Eq. (3.13). The thermal model results shown in Fig. 3.8(a) showed that a temperature gradient of several hundred degrees Kelvin can be induced between the front and back surfaces of the sample by using a value $D = 1.255 \times 10^{-4} \text{ cm}^2/\text{s}$ (four orders of magnitude smaller than the bulk value). There are oscillations in the electron diffraction

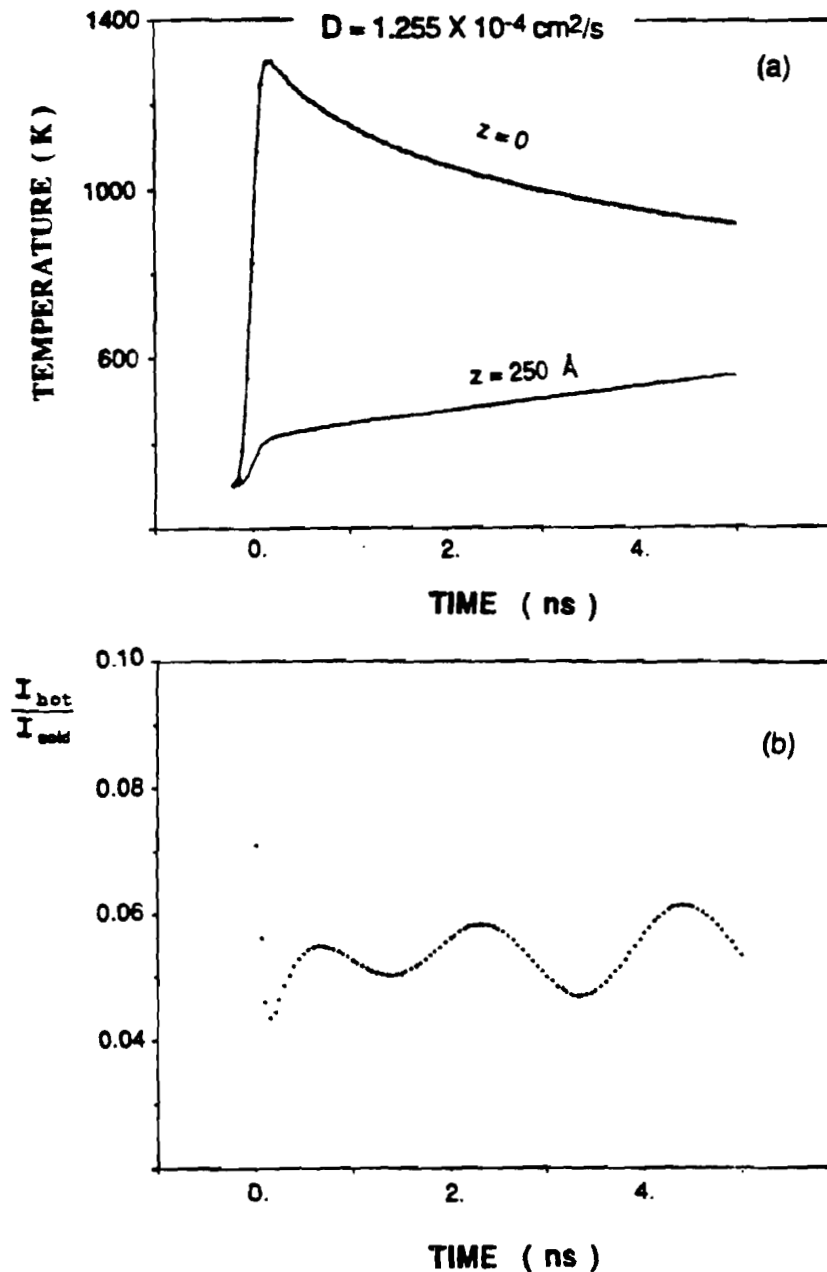


Fig. 3.8 (a) The temperature of the front and back surfaces of a laser-heated 25-nm thick gold film as a function of time calculated with the thermal model assuming the thermal diffusivity $D=1.255 \times 10^{-4} \text{ cm}^2/\text{s}$ which is four orders of magnitude smaller than the actual value. The duration of the laser pulse was 250 ps and the power density was $1.6 \times 10^8 \text{ W/cm}^2$. (b) The calculated time-dependent (220)-order normalized diffraction intensity corresponding to the temperature profile in (a). The average intensity is very low.

intensity but a significant decrease in diffraction intensity is also obtained, see Fig. 3.8(b). This implies that a continuous function such as the temperature gradient can not be responsible for the interference since its contribution to phase factors results in large reduction in the diffraction intensity, contrary to the experimental results. The calculated electron diffraction intensity for the correct thermal diffusivity $D = 1.255 \text{ cm}^2/\text{s}$ is shown in Fig. 3.9 for the three laser fluences.

3.4 SURFACE EXPANSION MODEL

The relatively small amplitude in oscillation seemed to indicate that the interference of scattered electrons was mainly between a small fraction of material, i.e. atoms at or near the surface, and the atoms of the bulk. In a 25-nm sample, the surface atoms form a significant fraction of the total number N and must be treated separately. They will have a different Debye-Waller factor. In addition, we note that the interlayer spacings between the top few layers, in general, are significantly larger than the bulk spacings,¹¹ that is, the lattice in the surface region is distorted and has a different thermal expansion coefficient. Additionally, the period of oscillations increases with time indicating that some relaxation processes are involved. We postulate that the rapid laser excitation of the material is followed by a surface lattice relaxation that is much slower than thermal equilibration within the bulk. The observed increase of the oscillation period with time and the size of the oscillation amplitude is consistent with this surface relaxation model. The electron waves

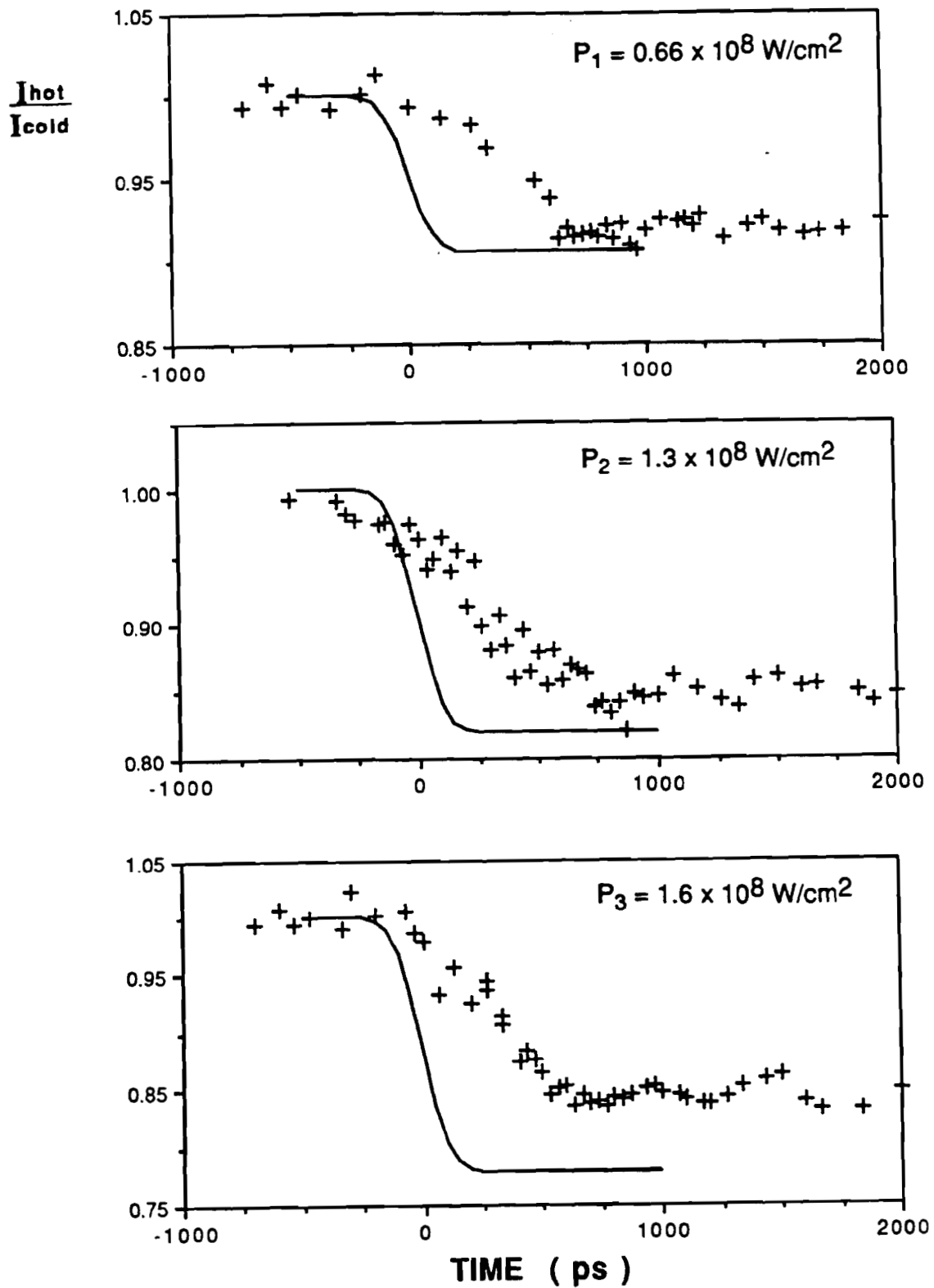


Fig. 3.9 The (220)-order normalized electron diffraction intensity as a function of probe delay for the three laser fluences. The solid curves were calculated using the thermal diffusion model. The crosses are the experimental points.

scattered by the atoms of the outermost surface layers are not necessarily in phase with those from the bulk, and therefore the resulting interference may produce an oscillation superimposed on the expected Debye-Waller monotonic curve.

It is well known that surface plasmons can be produced by relatively low laser fluences and may be associated with the observed oscillations. The formation of surface plasmons is initiated by electron emission from the surface of metals. This relatively low electron density then is increased by further absorption of laser photons to form a plasma layer. The plasma strongly couples with laser radiation and enhances the surface absorption. The surface plasmons will relax by either re-radiation (causing a change in optical reflectivity) or thermal equilibration with the surface atoms thus increasing the surface temperature. With thin films, as in this case, the plasmon formation may be quasi-symmetric with respect to the two surfaces.²⁷

The surface plasmon-generation is a two-step process. First, free-electron emission occurs. Second, this relatively low electron concentration increases through further absorption of laser energy to form a plasma layer. For the initial electron emission to occur at the laser fluence much below the bulk melt threshold, one mechanism requires the presence of localized surface defects, such as foreign particles on or embedded in the surface, metal flakes over a subsurface that are in poor thermal contact with the bulk. Another mechanism is electron emission due to plastic

micro-yielding of the metal surface that is induced by a rapid rise of surface temperature. The electrons are emitted from the metal surface at the deformation sites as a result of thermal stresses built up under laser irradiation. The number of the ejected electrons is assumed to be proportional to the total plastic strain.

The analytical model of plastic deformation proposed by Musal¹² defines the plastic yield threshold for a metal surface in terms of a critical surface temperature rise ΔT_y , which can be used to determine the laser fluence threshold P_y . Here ΔT_y is given as

$$\Delta T_y = \frac{1 - \psi}{\epsilon Y_m} S \quad 3.15$$

where S is the yield stress, ψ is poisson's ratio, ϵ is the coefficient of the thermal expansion, and Y_m is Young's modulus of the metal. If the maximum temperature rise during a laser pulse exceeds ΔT_y , electrons will be ejected from the surface. The sudden change in surface temperature required for plastic deformation can be as low as 20 K for copper irradiated by a CO₂ laser pulse.¹² We have estimated this required temperature-rise for our gold sample to be about 100 K. The further build-up of electron density is achieved through the interactions of the laser beam with the electrons which eventually form a dense electron plasma layer. With a shorter pulse duration, the laser fluence threshold electron emission will decrease. Other electron emission

initiation, such as through multiphoton photoelectric emission and high field emission processes, however, requires substantially higher laser intensity.

We have incorporated these concepts into a model calculation of the electron diffraction intensity. We considered a perfect lattice sandwiched between four layers of surface atoms with larger interlayer spacings than that of the bulk. The increase in the outermost interlayer spacing was taken to be larger than that between the second and third layer. Model simulations have shown that only the two or three outermost interlayer spacings depart appreciably from the bulk value.¹¹ After pulsed laser irradiation, the surface interlayer spacings are assumed to relax exponentially to their equilibrium values. The scattered electron waves by the surface atoms will not be in phase with those from the bulk under this condition. Therefore, this interference could cause the oscillation superimposed on the Debye-Waller monotonic curve. We proposed a simple model for this relaxation process as a preliminary investigation. A surface atom will be displaced to a position relative to the reference point in the reciprocal space as $z(t,T)$

$$z(t, T) = z_0(T) + \Delta z(T) \exp(-t/t_0) \quad 3.16$$

Where z_0 is the displaced position initially and $\Delta z = z_0 - z_\infty$ is the difference in distance between the expanded and relaxed position. The effect of irradiating laser power density levels on the phase factor was taken into account by adjusting the lattice spacing for both surface atoms and the atoms of its adjacent layers. Those free parameters were manipulated in order to obtain a

best fit with the experimental results. The size of the oscillation amplitude depends on the number of atoms affected by the distortion of the crystal lattice near the surface relative to the number of bulk atoms. If it is a large fraction, the overall oscillation amplitude will be larger. The period of the oscillations depends on the magnitude of the rate of change in the interlayer spacings. More oscillations occur with larger changes in the spacings. Both of the fraction of displaced surface atoms and the interlayer spacings are temperature-sensitive parameters dependent on the fluence of the laser heating pulse. The relaxation time constant controls the period of the oscillations. A smaller time constant causes faster oscillations. The best fit with our experimental data can be obtained by adjusting the changes in the interlayer spacings of the surface layers Δz and the relaxation time constant t_0 . The outermost spacings used in the surface expansion model simulation were 15% and 25% larger than their equilibrium values for the cases of laser heating power densities P_1 and P_3 , respectively. Our simulated curves for the three laser fluences are given in Fig. 3.10-3.12, where the exponential time constant was taken to be 3 ns. The sequence of maxima and minima is in reasonable agreement with the data considering the crudeness of the parameters used in the calculation. The calculated oscillation amplitude is considerably larger than the experimental. This may be due in part to a larger temperature factor β when surface plasmons are densely excited. Another possible reason for the large calculated amplitude is that in our model, we

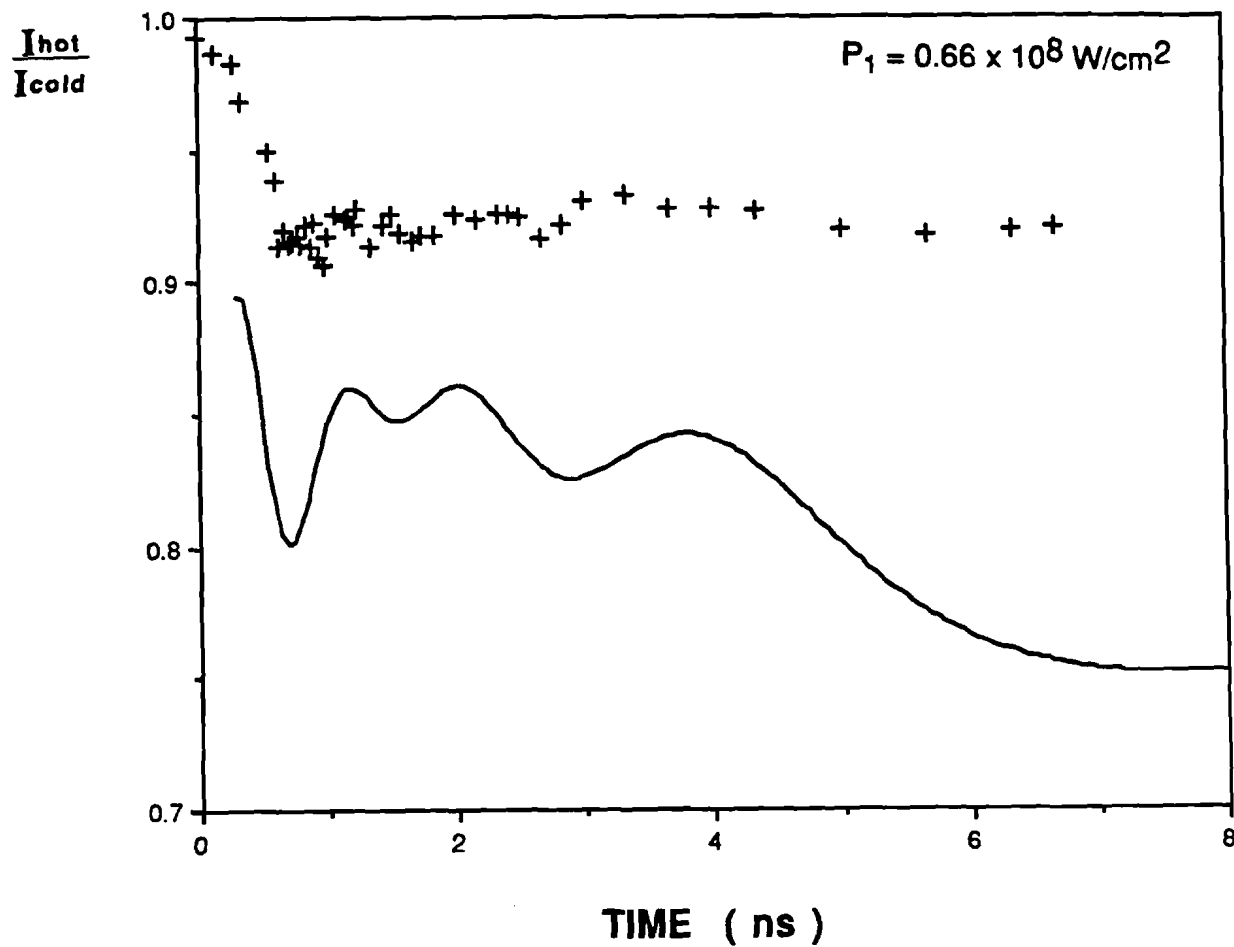


Fig. 3.10 The time-dependent (220)-order electron diffraction intensity for the indicated power density. The solid curve was calculated using the surface expansion model and the crosses are the experimental points.

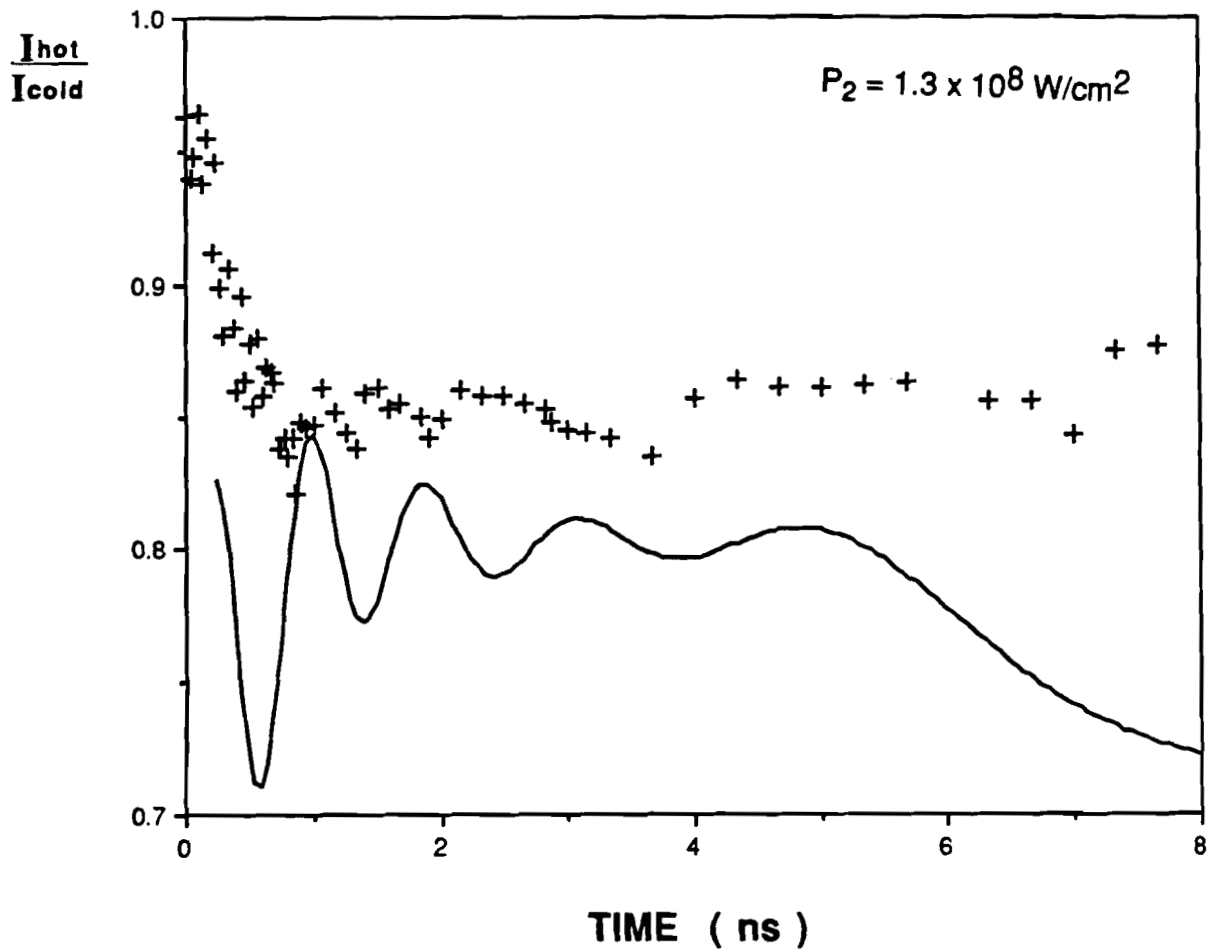


Fig. 3.11 The time-dependent (220)-order electron diffraction intensity for the indicated power density. The solid curve was calculated using the surface expansion model and the crosses are the experimental points.

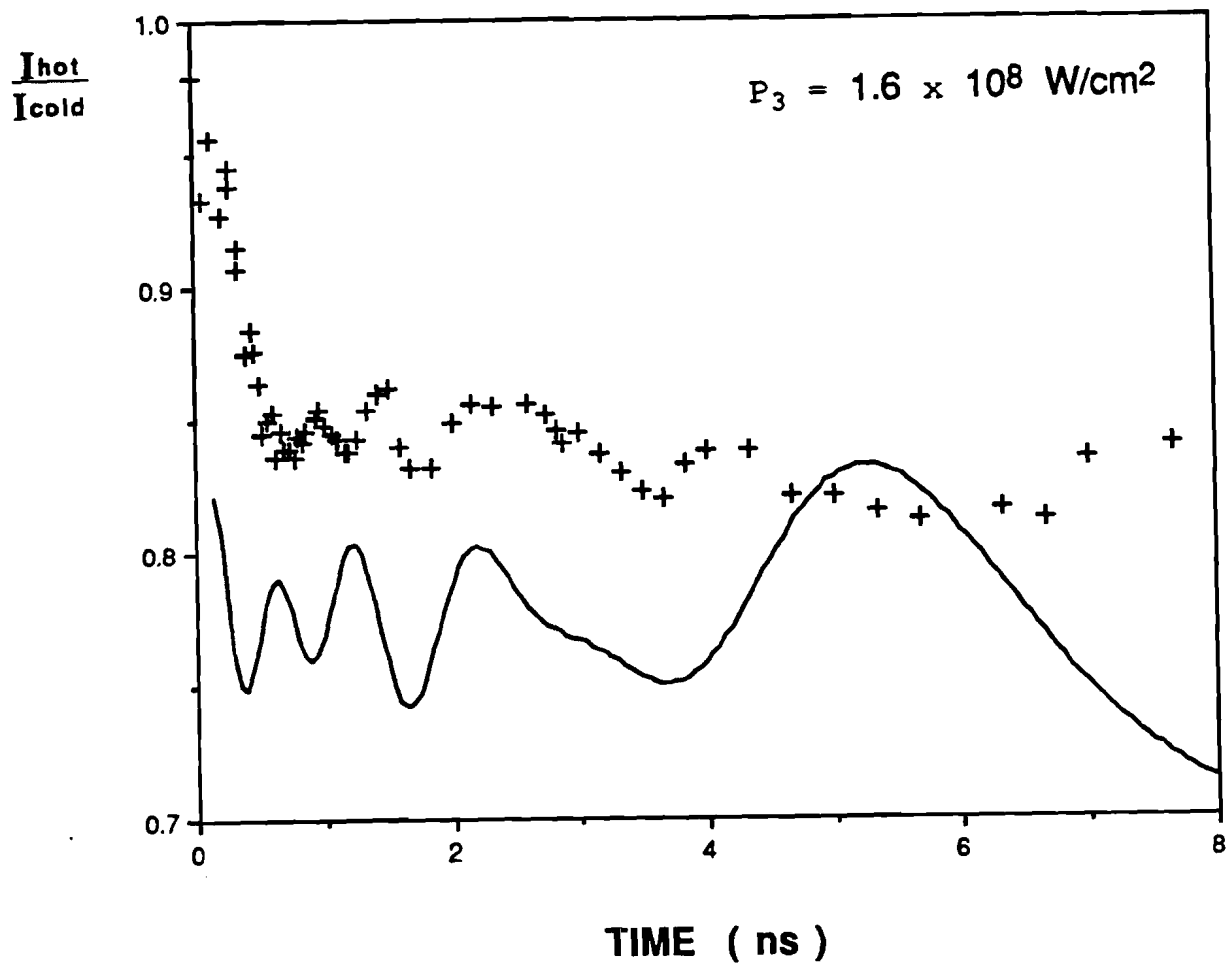


Fig. 3.12 The time-dependent (220)-order electron diffraction intensity for the indicated power density. The solid curve was calculated using the surface expansion model and the crosses are the experimental points.

assumed the surface layers expand and contract uniformly so that the electrons scattered from the atoms each individual layer are in phase. This may not be true. There may be some degree of incoherence in the movement of the atoms in the surface layers that would act to reduce the amplitude of the oscillations. The incoherence in the movement of the atoms is consistent with the plastic micro-yielding mechanism of electron emission by the surface layers.

The exact relaxation mechanism responsible for the observed oscillations has not been determined. One possibility is simply thermal relaxation of extremely hot surface atoms with the bulk. However, the long relaxation time we obtained (3 ns) is at least an order of magnitude greater than the thermal relaxation time of the bulk material. Therefore, this mechanism seems to be an unlikely explanation for the observed oscillations. A more plausible explanation is that the long relaxation time corresponds to the surface plasmon lifetime. This concept is in accord with estimated surface plasmon lifetimes (10^{-7} - 10^{-9} s).²⁸ We surmise that the excitation of surface plasmons weakens the bonds attaching the surface atoms leading to expansion of the crystal lattice in the surface region. This weakening of the bonds has obvious bearing on investigations of laser annealing. The postulated contraction of the surface region of the lattice is thus a direct consequence of the relaxation of surface plasmons. Further experiments are needed in order to establish the surface plasmon relaxation mechanism.

3.5 CONCLUSION

This work has established what we believe is the fastest lattice temperature probe to study the dynamics of pulsed laser heating. We observed oscillatory behavior in the electron diffraction intensity as a function of delay time. We offered an interference mechanism between the scattered electron waves from surface atoms and those from bulk atoms as an explanation of the oscillations observed in the experimental data. The amplitude and the number of oscillations depend on the increased lattice spacing near surface with respect to bulk lattice. The lattice distortion near the surface, resulting from surface-plasmon excitation, relaxes to its equilibrium position in about 3 ns which is considerably longer than the bulk thermal relaxation time.

The model associated with the surface effect can explain the oscillation only qualitatively. However, the computer simulation gave a reasonably good data fit with the experimental results. It should be noted that this above discussion was not intended to give a conclusive interpretation but rather, to evaluate the possibility of surface effects. For future studies we would urge that data be taken with various thicknesses, various diffraction orders and different materials to enable further interpretation. More detailed theoretical models should employ lattice dynamics directly.

References for Chapter 1

1. E. I. Shtyrko, I. B. Khaibullin, M. M. Zaripov, M. F. Galyatudinov, and R. M. Bayazitov, *Sov. Phys.-Semicond.* **9**, 1309 (1975)
2. J. Narayan, O. W. Holland, C. M. White, and R. T. Young, *J. Appl. Phys.* **55**, 1125 (1983)
3. C. Cesari, G. Nihoul, J. Marfaing, W. Marine, and B. Mutaftschiev, *J. Appl. Phys.* **57**, 5199 (1985)
4. M. J. Hart and A. G. R. Evans, *Semicond. Sci. Technol.* **3**, 421 (1988)
5. C. J. Lin and F. Spaepen, *App. Phys. Lett* **41(8)**, 721 (1982)
6. W. K. Wang and F. Spaepen, *Appl. Phys. Lett.* **49(5)**, 295 (1986)
7. W. M. Steen and J. Powell, *Laser Surface Treatment*, (1981)
8. C. H. Wu and J. I. Gittleman, *J. Appl. Phys.* **55**, 2928 (1984)
9. R. Kern and W. Theiner in: *Proceedings of The European Conference on Laser Treatment of Materials* ed. B. L. Mordike (Verlag, Germany 1987), p.427
10. J. M. Poate, *J. of Crystal Growth* **79**, 549 (1986)
11. D. H. Auston, J. A. Golovchenko, P. R. Smith, C. M. Surko, and T. N. C. Venkatesan, *App. Phys. Lett* **33**, 539 (1978)
12. C. W. Draper, C. M. Preece, D. C. Jacobson, in *The 1979 Proceedings of Symposium on Laser and Electron Beam Processing of Materials*, ed. C. W. White and P.S. Peercy (Academic Press, New York 1980), p.721

13. P. L. Antona, S. Appiano, and R. Moschini in: Proceedings of The European Conference on Laser Treatment of Materials ed. B. L. Mordike (Verlag, Germany 1987), p.133
14. C. W. Draper, in 1980 proceedings of Symposium in Lasers in Metallurgy, ed. K. Mukherjee and J. Mazumder (The metallurgical Society of AIME, New York 1981) , p.67
15. J. Powell and W. M. Steen, in 1980 proceedings of Symposium in Lasers in Metallurgy, ed. K. mukherjee and J. Mazumder (The metallurgical Society of AIME, New York 1981), p.93
16. N. Bloembergen in 1979 Laser-Solid Interactions and Laser Processing, ed. S. D. Ferris, H. J. Leamy, and J. M. Poate (AIP, New York 1979), p.1
17. D. M. Kim and D. L. Kwong, IEEE J. of Quantum Electronics **QE-18**, 224 (1982)
18. J. A. Van Vechten, in The 1979 Proceedings of a Symposium on Laser and Electron Beam Processing of Materials, ed. C. W. White and P.S. Peercy(Academic Press, New York 1980), p.53
19. J. A. Van Vechten, R. Tsu, and F. W. Saris, Phys. Lett. **74A**, 422 (1979)
20. A. Compaan, A. Aydinli , M. C. Lee, and H. W. Lo in 1982 Laser and Electron Beam Processing of Materials, ed. B. R. Appleton and G. K. Celler, p.43
21. D. H. Auston, J. A. Golovchenko, A L. Simons, R. E. Slusher, P. R. Smith, C. M. Surko, and T. N. C. Venkatesan, in: 1979 Laser-Solid Interactions and Laser processing, ed. S. D. Ferris, H. J. Leamy, and J. M. Poate (AIP, New York 1979), p11
22. A. Compaan, M. C. Lee, H. W. Lo, G. Trott, and A. Aydinli, J. Appl. Phys. **54**, 5950 (1983)

23. C. A. MacDonald, A. M. Malvezzi, and F. Spaepen, in 1986 MRS Symposium Proceeding on Energy Beam-Solid Interactions and Phase Transformations 5, ed H. Kurz, G. L. Olson, and J. M. Poate (North-Holland, New York 1986), p.277
24. D. H. Auston, C. M. Surko, T. N. C. Venkatesan, R. E. Slusher, and J. A. Golovchenko, App. Phys. Lett 33, 437 (1978)
25. C. V. Shank, R. Yen, and C. Hirlimann, Phys. Rev. Lett. 50, 454 (1983)
26. C. P. Grigoropoulos and R. H. Buckholz, J. Appl. Phys. 59, 454 (1986)
27. C. A. MacDonald, A. M. Malvezzi, and F. Spaepen, J. Appl. Phys. 65, 129 (1989)
28. M. C. Lee, H. W. Lo, A. Aydinli, and A. Compaan, App. Phys. Lett 38, 499 (1981)
29. L. A. Lompre, J. M. Liu, H. Kurt, and N. Bloembergen, App. Phys. Lett 43, 168 (1983)
30. M. Von Allmen, Laser-Beam Interactions with Materials (Springer-Verlag Berlin Heidelberg, Germany 1987), Chapter 2
31. Y. Kanemitsu, Y. Ishida, I. Nakada, and H. Kuroda, App. Phys. Lett 48, 209 (1986)
32. P. L. Liu, R. Yen, N. Bloembergen, and R.T. Hodgson, App. Phys. Lett 34, 864 (1979)
33. K. Yoshii, M. Umeno, S. Murata, H. Kawabe, K. Yamada, I. Watanabe, and T. Kubo, J. Appl. Phys. 55, 223 (1984)
34. Y. Kanemitsu, I. Nakada, and H. Kuroda, J. Appl. Phys. 48, 209 (1986)

35. I. W. Boyd, S. C. Moss, T. F. Boggess, and A. L. Smirl, *App. Phys. Lett* **45**, 80 (1984)
36. A. L. Smirl, T. F. Boggess, S. C. Moss, and I. W. Boyd, *J. Lumin.* **30**, 272 (1985)
37. A. M. Bonch-Bruevich, Ya. A. Imas, G. S. Romanov, M. N. Liebenson, and L. M. Mal'tsev, *Sov. Phys.-Tech. Phys.* **13**, 640 (1968)
38. B. C. Larson, J. Z. Tischler, and D. M. Mills, *J. Mater. Res.* **1**, 144 (1986)
39. J. Z. Tischler, B. C. Larson, and D. M. Mills, *App. Phys. Lett* **52**, 1785 (1988)
40. H. C. Gerritsen, H. Van Brug, F. Bijkerk, K. Murakami and M. J. Van der Wiel, *J. Appl. Phys.* **60**, 1774 (1986)
41. G. Mourou and S. Williamson, *Appl. Phys. Lett.* **41**, 44 (1982)
42. S. Williamson, G. Mourou and J. C. M. Li, *Phys. Rev. Lett.* **52**, 2364 (1984)
43. D. Von Der Linde, G. Wartmann, M. Kemmler, and Z. H. Zhu in 1983 MRS Symposium Proceeding on Energy Beam-Solid Interactions and Transient Thermal Processing, ed J. C. C. Fan and N. M. Johnson (North-Holland, New York 1984), p.123
44. A. Compaan and H. J. Trodahl, *Phys. Rev.* **B29**, 793 (1984)
45. G. Wartmann, D. Von Der Linde, and A. Compaan, *App. Phys. Lett* **43**, 613 (1983)
46. G. E. Jellison, D. H. Lowndes, and R. F. Wood, *Phys. Rev.* **B28**, 3272 (1983)

47. A. Compaan, in 1985 MRS Symposium on Energy Beam-Solid Interactions and Transient Thermal Processing, ed. D. K. Biegelsen, G. A. Rozgonyi, and C. V. Shank (North-Holland, New York 1985), p.23
48. G. Wartmann, M. Kemmler, and D. Von Der Linde, Phys. Rev. **B30**, 4850 (1984)
49. J. M. Hicks, L. E. Urbach, E. W. Plummer, and H. L. Dai, Phys. Rev. Lett. **61**, 2588 (1988)
50. N. Bloembergen, R. K. Chang, S. S. Jha, and C. H. Lee, Phys. Rev. **174**, 813 (1968)
51. C. V. Shank, R. Yen, and C. Hirlimann, Phys. Rev. Lett. **51**, 900 (1983)
52. D. Guidatti, T. A. Driscoll, and H. J. Gerritsen, Solid State Commun. **46**, 337 (1983)
53. S. A. Akhmanov, M. F. Galyautdinov, N. I. Koroteev, G. A. Paityan, I. B. Khaibullin, E. I. Shtyrkov, and I. L. Shumal, Sov. J. Quantum Electron. **13**, 687 (1983)
54. J. Y. Tsao, S. T. Picraux, P. S. Peercy, and M. O. Thompson, App. Phys. Lett. **48**, 278 (1986)
55. G. J. Galvin, M. O. Thompson, J. W. Mayer, R. B. Hammond, N. Paulten, and P. S. Peercy, Phys. Rev. Lett. **48**, 33 (1982)
56. H. M. Milchberg, R. R. Freeman, S. C. Davey, and R. M. More, Phys. Rev. Lett. **61**, 2364 (1988)
57. J. E. E. Baglin, R. T. Hodgson, J. M. Neri, and R. Fastow, App. Phys. Lett. **43**, 299 (1983)

58. P. H. Fuoss, L. J. Norton, and S. Brennan, *Phys. Rev. Lett.* **60**, 2046 (1988)
59. R. S. Becker, G. S. Higashi, and J. A. Golovchenko in: 1983 MRS Proceedings, V.23, Energy Beam-Solid Interactions and Transient Thermal Processing, ed. J. C. C. Fan and N. M. Johnson (North-Holland, New York 1984), p.129
60. M. Jalochowski and E. Bauer, *J. Appl. Phys.* **63**, 4501 (1988)
61. H. Nakahara and A. Ichimiya, *J. of Cryst. Growth* **95**, 472 (1989)
62. J. M. Liu, H. Kurz, and N. Bloembergen, *App. Phys. Lett* **41**, 643 (1982)
63. H. E. Elsayed-Ali, T. B. Norris, M. A. Pessot, and G. A. Mourou, *Phys. Rev. Lett.* **58**, 1212 (1987)
64. A. Pospieszczyk, M. A. Harith, and B. Stritzker, *J. Appl. Phys.* **54**, 3176 (1983)
65. P. Debye, *Verh. Deut. Phys. Ges.* **15**, 678, 738, 857 (1913); *Ann. Phys.* **43**, 49 (1913-1914)
66. I. Waller, *Z. Phys.* **17**, 398 (1923), **51**, 213 (1928); Dissertation, University of Uppsala (1925); *Ann. Phys.* **79**, 261 (1926)
67. H. Faxen, *Z. Phys.* **17**, 266 (1923); *Ann. Phys.* **54**, 615 (1918)
68. H. P. Klug and L. E. Alexander, *X-ray Diffraction Procedures for Polycrystalline and Amorphous Materials*, 2nd ed. (John Wiley & Sons, New York 1974), pp144-148
69. R. M. Nicklow and R. A. Young, *Phys. Rev.* **152**, 591 (1966)

70. R. W. James, G. W. Brindley, and R. G. Wood, *Proc. R. Soc.* **A125**, 410 (1929)
71. P. A. Flinn and G. M. McManus, *Phys. Rev.* **132**, 2458 (1963)
72. R. E. Dingle and E. H. Medlin, *Acta Cryst.* **A28**, 22 (1972)
73. D. R. Chipman, *J. Appl. Phys.* **31**, 2012 (1960)
74. E. A. Owen and R. W. Williams, *Proc. R. Soc. (London)* **A188**, 509 (1947)
75. V. Synecek, H. Chessin, and M. Simerska, *Acta Cryst.* **A26**, 108 (1970)
76. O. P. Gupta, *J. of the Phys. Soc. Japan* **52**, 4237 (1983)
77. H. Boersch, O. Bostanjoglo, and H. Niedrig, *Z. Physik* **180**, 407 (1964)
78. W. Glaeser and H. Niedrig, *J. Appl. Phys.* **37**, 4303 (1966)
79. W. Albrecht and H. Niedrig, *J. Appl. Phys.* **39**, 3166 (1968)
80. A. MacRae and L. Germer, *Phys. Rev. Lett.* **8**, 489 (1962)
81. S. I. Kovalenko, N. V. Krainyukova, A. T. Pugachev, and N. P. Churakova, *Sov. Phys. Crystallogr.* **24**, 634 (1979)
82. V. N. Skokov, A. A. Dik, V. P. Koverda, and V. P. Skripov, *Phys. Met. Metall.* **56**, 125 (1983)
83. C. Solliard, *Solid State Comm.* **51**, 947 (1984)
84. C. Solliard, M. Flueli et J.-P. Borel, *Acta Phys.-Helvetica*, **61**, 730 (1988)
85. Ph. Buffat, *Solid State Comm.* **23**, 547 (1977)

86. M. Kostelitz and J. L. Domange, *Solid State Comm.* **13**, 241 (1977)
87. R. D. Heidenreich, *J. Appl. Phys.* **33**, 2321 (1962)
88. B. W. Batterman, *Phys. Rev.* **126**, 1461 (1962)
89. C. R. Hall and P. B. Hirsch, *Proc. R. Soc. (London)* **A286**, 158 (1964)
90. G. Hiller, T. Just, and H. Niedrig, *Phys. Lett.* **32A(4)**, 262 (1970)
91. A. Howie and M. J. Whelan, *Proc. R. Soc. (London)* **A263**, 217 (1961)
92. H. Hashimoto, A. Howie and M. J. Whelan, *Proc. R. Soc. (London)* **A269**, 80 (1962)
93. H. Boersch, G. Jesehke, and H. Raith, *Z. Physik* **181**, 436 (1964)
94. J. Hansen-Schmidt, *Z. Physik* **198**, 433 (1967)
95. I. N. Duling III, P. Bado, S. Williamson, G. Mourou, and T. Baer, in: *Digest of Conference on Lasers and Electro-Optics* (OSA, Washington, D. C. 1984), paper PD3
96. I. N. Duling III, T. Norris, T. Sizer II, P. Bado, and G. Mourou, *J. Opt. Soc. Am.* **B2**, 616 (1985)

References for Chapter 2

1. P. Debye, *Verh. Deut. Phys. Ges.* **15**, 678, 738, 857 (1913); *Ann. Phys.* **43**, 49 (1913-1914)
2. I. Waller, Dissertation, University of Uppsala (1925); *Ann. Phys.* **79**, 261 (1926); **83**, 154 (1927)
3. I. N. Duling III, P. Bado, S. Williamson, G. Mourou, and T. Baer, in: *Digest of Conference on Lasers and Electro-Optics* (OSA, Washington, D. C. 1984), paper PD3
4. I. N. Duling III, T. Norris, T. Sizer II, P. Bado, and G. Mourou, *J. Opt. Soc. Am.* **B2**, 616 (1985)
5. *Photoemission and The Electronic Properties of Surfaces*, ed. by B. Feuerbacher, B. Fitton, and R. F. Willis (John Wiley & Sons, New York 1978), p.481
6. *LLE Review* **16**, 54 (1983)
7. S. Williamson, G. Mourou, and S. Letzring, *Proc. 15th International Conference on High Speed Photography* **348**, 197 (1983)
8. G. Mourou and S. Williamson, *Appl. Phys. Lett.* **41**, 44 (1982)
9. C. Kittel, *Introduction to Solid State Physics*, 5th edition, (John Wiley & Sons, New York 1976), p.126
10. M. Von Allmen: *Laser and Electron Beam Processing of Materials*, ed. C. W. White and P. S. Peercy (Academic Press, New York 1980), p.6
11. M. Von Allmen: *Laser Annealing of Semiconductors*, ed. J. M. Poate and J. W. Mayer (Academic Press, New York 1982), p.43

12. A. Castaing, *Adv. Electr. Elec. Phys.* **13**, 317 (1960); and Thesis, Univ. of Paris, Paris, France (1951)
13. G. S. Almasi, J. Blair, R. E. Ogilvie, and R. J. Schwartz, *J. Appl. Phys.* **36**, 1848 (1965)
14. F. M. Wahl, *Digital Image Signal Processing* (Arthech House, Boston 1987), Chapter 2.
15. E. O. Brigham, *The Fast Fourier Transform* (Prentice Hall, 1974)
16. G. Thomas, *Transmission Electron Microscopy of Metals* (UC-Berkeley, 1966), p.174; also private communication with Professor Richard W. Vook of The Department of Physics, and The Solid State Science and Technology Program, Syracuse University.

References for Chapter 3

1. Shock Waves and High-Strain-Rate Phenomena in Metals, Concepts and Applications, ed. by M. A. Meyers and L. E. Murr (Plenum Press, New York 1981)
2. A. H. Clauer, J. H. Holbrook, and B. P. Fairand, p.675 of ref.1
3. G. A. Askaryon and E. M. Morez, Sov. Phys. JETP Lett. **16**, 1638 (1963)
4. N. C. Anderholm, App. Phys. Lett. **16**, 113 (1970)
5. J. O. O'Keefe, C. H. Skeen, and C. M. York, J. Appl. Phys. **44**, 4622 (1973)
6. B. P. Fairand and A. H. Clauer, Opt. Comm. **18**, 448 (1976)
7. R. M. White, J. Appl. Phys. **34**, 2123 (1963)
8. D. W. Gregg and S. J. Thomas, J. Appl. Phys. **37**, 2787 (1966)
9. C. H. Skeen and C. M. York, J. Appl. Phys. **12**, 369 (1968)
10. L. E. Kinsler and A. R. Frey, Fundamentals of Acoustics, 2nd. ed. (John Wiley & Sons, Inc., New York 1962) p.103
11. J. Q. Broughton and G. H. Gilmer, J. Chem. Phys. **79**, 5105 (1983)
12. H. M. Musal, Jr. in 1980 Laser Induced Damage in Optical Materials, NBS Special Publication, V. 620, ed. H. E. Bennett, A. J. Glass, A. H. Guenther, and B. E. Newnam (1981), p.227
13. C. J. Powell and J. B. Swan, Phys. Rev. **118**, 640 (1960)
14. R. H. Ritchie, Phys. Rev. **106**, 874 (1957)

15. T. Tsang and D. D. Smith, *Opt. Comm.* **70**, 115 (1989)
16. N. Bloembergen in 1979 *Laser-Solid Interactions and Laser Processing*, ed. S. D. Ferris, H. J. Leamy, and J. M. Poate (AIP, New York 1979) p.1
17. J. H. Bechtel, *J. App. Phys.* **46**, 1585 (1975)
18. R. D. Richtmyer and K. W. Morton, *Difference Methods for Initial-Value Problems*, 2nd edition (Wiley & Sons, Inc., New York 1967)
19. S. I. Kovalenko, N. V. Krainyukova, A. T. Pugachev, and N. P. Churakova, *Sov. Phys. Crystallogr.* **24**, 634 (1979)
20. C. Solliard, *Solid State Comm.* **51**, 947 (1984); C. Solliard, M. Flueli et J.-P. Borel, *Acta Phys.-Helvetica*, **61**, 730 (1988)
21. Ph. Buffat, *Solid State Comm.* **23**, 547 (1977)
22. E. A. Owen and R. W. Williams, *Proc. R. Soc. (London)* **A188**, 509 (1947)
23. O. P. Gupta, *J. of the Phys. Soc. Japan* **52**, 4237 (1983)
24. W. Albrecht and H. Niedrig, *J. Appl. Phys.* **39**, 3166 (1968)
25. H. Boersch, O. Bostanjoglo, and H. Niedrig, *Z. Physik* **180**, 407 (1964)
26. W. Glaeser and H. Niedrig, *J. Appl. Phys.* **37**, 4303 (1966)
27. H. Raether, *Surface Plasmons on Smooth and Rough Surfaces and on Gratings*, Springer Tracts in Modern Physics, V.111 (1988), p.25
28. J. A. Van Vechten, R. Tsu, and F. W. Saris, *Phys. Lett.* **74A**, 417 and 422 (1979)

APPENDIX A: THIN FILMS PREPARATION

The thin films prepared for electron diffraction studies should have the desired surface orientation and be reasonably uniform, and the region probed by the electron beam should be a representative area of the sample. Preparation methods for suitably thin samples from bulk samples for transmission electron diffraction studies, include electropolishing,¹ chemical etching,²⁻³ and ion bombardment.⁴ A jet-machining method⁵ can be used to reduce massive samples to a 100-200 μm thickness before applying the electropolishing technique. Many nonmetallic materials, such as rock salts, graphite, molybdenite, and mica, etc. can be cleaved easily⁶ to form thin flakes or layers for examination by transmission electron diffraction or microscopy.

It is also possible to prepare thin films directly by vacuum evaporation,⁷⁻⁹ particularly for the thin metal films. Pertinent physical data on the evaporation of metals can be found in Holland¹⁰ and also in Thomas.¹¹ Other techniques for the direct formation of thin films include distillation from the vapor in vacuum to form dislocation-free crystals,¹² deposition from a dilute solution,¹³ regrowth from a melt,¹⁴ shock-wave chilling of droplets of molten metal,¹⁵ and electrodeposition¹⁶ by epitaxial growth of electrodeposits. For soft metals, particularly for multiphased alloys, or biological sections, ultramicrotoming¹⁷ is an useful technique. In his book,

Transmission Electron Microscopy of Metals, Chapter 4, Thomas¹¹ describes several methods for the preparation of thin specimens.

A.1 Vacuum evaporation methods

The structures and properties of thin film prepared by vacuum evaporation method can be affected by the following factors:

(a) Evaporation conditions. The pressure and the nature of the residual gas in the vacuum chamber, the temperature and the material of the filament used to evaporate the material, and the deposition rate are variables that must be controlled to obtain the desired properties in the deposited film.

(b) Substrate. The crystal structure and the temperature of the substrate can affect the orientation of thin film. If metal film is deposited on a hot, crystalline substrate, the orientation of the film follows that of the substrate surface and thus grows epitaxially.

(c) Diffusion. The surface diffusion of substrate atoms into the film is a problem sometimes encountered. Chemical reactions or alloying between the atoms of the film and substrate changes both the structure and the properties of the film, but this can be avoided by choosing an appropriate substrate.

(d) Charged particle bombardment. Exposure of the substrate surface to the bombardment of charge particles, such as ions and electrons, may increase the density of surface defects which act as nucleation centers.¹⁸ The presence of these defects seems to enhance epitaxial growth and can result in a great improvement in the quality of single-crystal films.

Normally, films of materials with a cubic crystal structure can be formed in a [111] orientation by evaporation onto a cleaved mica substrate at about 270 C.⁷⁻⁹ If a cleaved salt crystal is used as substrate material then a [100] orientation can be produced at a higher temperature, around 400-450 C. By controlling the substrate temperature and the evaporation rate, a continuous thin film with a desired orientation can be obtained. In general, the higher the substrate temperature the more likely it is for the orientation to form. However, it is not so clear concerning the role of the deposition rate. Although a low deposition rate is favored for epitaxial growth, the formation of a continuous film is more likely with higher rate. Thus a compromise in the evaporation rate is necessary for a continuous oriented film to be formed. The typical deposition rate is 1 Å per second, which can produce reasonably continuous thin single-crystal. The metal film can be peeled off a mica substrate. In the case of a salt substrate, it may be removed from the film by dissolving in water and then catching the film on a holder, such as a grid or mesh.

Sometimes the high temperature requirement may be obstacle for the preparation of films of certain metal such as Pb and Rh or where the substrate tends to form a amorphous structure at a high temperature. In these cases, an intermediate metal film, such as silver, can be evaporated at a lower substrate temperature to form a thin layer (10 to 20 Å) with the desired orientation on the surface of the substrate.⁸⁻⁹ Oriented films of the desired metal may then be formed by depositing onto the silver layer. In this way, the substrate temperature required for the formation of single-crystal films can be as low as

250-300 C. The silver film can be removed by dissolving it in nitric acid.

If a cold (at room temperature) amorphous or polycrystalline substrate is used for evaporation, a film with polycrystalline structure is formed. A smooth polycrystalline substrate can be made by the evaporation of a thin film of formvar solution floating on top of water. The formvar can be subsequently removed by ethylene dichloride etching .

Sometimes, the prepared polycrystalline film requires post-growth treatment, i.e. annealing. A large crystallite can be formed by a dumbbell growth process¹⁸ which depends on the surface diffusion mobility and the interfacial energies associated with a grain boundary. The annealing temperature, heating rate, and the presence of gas can be controlled to achieve the desired result.

A.2 Polycrystalline thin films

Our free-standing aluminum and gold polycrystalline films were deposited onto a formvar substrate at room temperature. Formvar is soluble in ethylene dichloride. Ethylene dichloride is quite toxic, however, so the preparation of the formvar substrate should be done under a vent hood and surgical gloves should be worn. The typical concentration of the formvar solution, which can be prepared by dissolving calcium oxide (formvar resin) in redistilled ethylene dichloride, was 0.25%,. To produce a thin formvar substrate, a pipette was used to carefully drop some formvar solution into some water. The formvar spreads to form a thin plastic film on the water

surface. After the ethylene dichloride had evaporated, a specimen holder was inserted underneath the plastic film and lifted up to form a thin coating of formvar over the specimen holder. The coating should be examined to see that it is smooth and continuous over the holes in the specimen holder with good attachment at the edges. After drying, the formvar substrate was placed in the vacuum evaporator. A deposition rate of $5\text{\AA}/\text{s}$ was normally used to form a continuous thin film. The thickness of aluminum and gold films were 200-250 \AA . Since the formvar would interfere with diffraction of electrons, the formvar is dissolved by ethylene dichloride vapor etching. The process should be gentle because the sample surviving rate is quite low. Usually, only 50% of the samples were good enough for use in the electron diffraction experiments.

A.3 Single-crystal thin films

The single-crystal thin films of gold were prepared by vacuum evaporation. When vapor deposition is carried out with a hot crystalline substrate, the orientation of the film follows that of the substrate and grows epitaxially. For the substrate, we cleaved single crystal rock salt (NaCl) to form a smooth [100] orientation. This was placed on a hot plate in the evaporator. The temperature of the substrate was about 450 C and was carefully monitored. Using a slow deposition rate (less than 1 \AA per second), a continuous coherent thin single-crystal gold film with a [100] orientation can be produced. We required the thickness to be less than 30 nm for the

transmission electron diffraction experiment because of the short extinction length of gold. The extinction lengths for various electron energies of several metals that have a face-centered-cubic crystal structure are listed in Table A.1. The gold film was freed by dissolving the substrate in water. It was then lifted out of the water with a specimen holder with hole diameter of 0.5mm.

Table A.1 Extinction lengths for gold and aluminum (face-centered cubic) as a function of electron energy for several diffraction orders.

	E (keV)	Extinction Length (Å)							
		(111)	(200)	(220)	(311)	(400)	(440)		
Au	1	20	23	30	36	45	69		
	10	63	73	97	115	142	219		
	25.5	102	116	155	185	229	352		
	40	127	147	196	233	288	444		
	50	144	165	220	262	324	500		
	100	209	239	318	379	469	722		
Al	1	61	78	121	150	192	303		
	10	194	246	385	475	611	961		
	25.5	312	396	619	764	982	1545		
	40	394	500	781	964	1240	1950		
	50	443	561	877	1083	1392	2190		
	100	641	811	1270	1566	2014	3167		

APPENDIX B : TEMPERATURE EFFECTS IN ELECTRON DIFFRACTION

Debye¹ first realized the effects of small and random thermal displacements on the intensity of diffraction maxima. He later applied his theory of specific heat, i.e. modes of vibration for discontinuous solids, to the role of thermal vibrations of the atoms in diffraction phenomena. He found that such displacements diminished the intensity of diffraction maxima but left their sharpness unaltered. A complete expression for the temperature factor in terms of the normal modes of the lattice was first given by Waller² and subsequently Faxen³ gave a necessary modification to Debye's original time-averaging method. Faxen's treatment did not affect the intensity of diffraction maxima but introduced a correct expression for thermal diffuse scattering (TDS). The neglect of interatomic force in Debye's model was not correct in dealing with real crystals. The monotonic TDS curve predicted by Debye thus was corrected and replaced by a discrete function in Faxen's treatment. An interaction coefficient was introduced by Faxen to represent the interatomic force between any pair of atoms which is essential in predicting the actual shape of the TDS curve. The correct TDS function has broader and more diffuse maxima in the direction of the Bragg diffraction, see in Fig. 1.2, and increases with the diffraction orders. These diffuse maxima were neglected in earlier experimental photographs⁴ until they were definitely observed by Lavel⁵ in 1938.

The effect of heat is to introduce a factor $\exp(-2M)$ (see, e.g., ref. 6) into the diffraction intensity, where M was defined in Chapter 1. The Debye-Waller factor applies strictly only to the cubic crystals containing one kind of atom. Helmholtz⁷ developed an anisotropic temperature factor to describe a crystal without cubic symmetry. This was studied experimentally for various materials with less cubic symmetry and was found in good agreement with the calculated anisotropic temperature factor.⁸⁻⁹ Moreover, for a crystal containing different kinds of atoms which do not have identical vibration amplitudes, it is necessary to include the appropriate Debye-Waller factor for each atom in the unit cell. Other limitations of the theory are the following:

(a) Constant volume.

This assumption is not consistent since the volume of the crystal changes with temperature. The correction must be made by taking higher order corrections to the thermal displacement into account in the temperature factor. This is the anharmonic correction for high temperature. A qualitative investigation was made by Waller¹⁰ and a numerical work treating the Debye characteristic temperature as a function of the temperature was performed by Zena and Bilinsky.¹¹ The temperature dependence of the Debye temperature is a consequence of thermal expansion.

Owen and Williams¹² measured X-ray reflection intensities as a function of temperature for various metal (Al, Cu, and Au) powder specimens. A sharp fall in the intensity at very high temperature was observed and was

attributed to the temperature dependence of the Debye temperature. The reduction of the characteristic temperature with increasing temperature results in an increasing temperature factor. This anharmonic phenomena was studied theoretically for many metals by Gupta¹³ who analyzed various experimental results for the temperature dependence of X-ray diffraction intensity. Buffat¹⁴ observed a similiar result in electron diffraction intensity of gold by using 50 keV electrons. Although he attributed this to the size effect, some doubts have been raised concerning his interpretation.

(b) Single cutoff frequency.

This assumption basically treated the real crystal as isotropically continuous, and the actual discrete nature was considered by terminating the series of propagating waves with an upper cutoff limit. For the lattice of one kind of atom, Blackman¹⁵ had shown that there are several frequency maxima in the frequency spectrum and some of them, he found, were at a much lower frequency than the cut-off value used in Debye's theory. For diatomic crystals,¹⁶ Debye's theory must be modified.

(c) Surface effect

Surface effects have been studied by means of low energy electron diffraction (LEED)¹⁷⁻¹⁸ which is basically surface sensitive. Those results showed larger surface atomic vibrational amplitudes than those of the bulk material. A stronger than expected in the temperature effect for surface atoms

was observed. The reduction of the surface Debye-Waller factor from its bulk value was related to the decrease of the Debye temperature for surface atoms. The effective surface Debye temperature is found to be reduced by a factor of two from its bulk value.¹⁷⁻¹⁸ As the energy of the electron beam increases, the surface Debye temperature approaches the bulk value. This implies that the electron sees the bulk properties rather than those of the surface. It was shown that when the energy of electron beam is at or about 200 eV, the Debye temperature for Au[110] is near the bulk value.¹⁷

(d) Size effects

Large atomic vibrational amplitudes for small particles have been studied by using high energy electron diffraction (HEED).¹⁹⁻²² The connection of the size effect to the surface effect is that a larger fraction of surface atoms contribute to the effective atomic vibrational amplitudes in small particles. The effective temperature factor β (defined in Eq. (2.2)) increases with the decreasing particle size and results in a larger decrease in the observed electron diffraction intensity for small particles. Some experimental results have shown that gold particles exceeding 20 nm in diameter does not exhibit any size effects at a electron beam energy higher than 50 keV.²² It is clear that the critical size of crystal for size effect depends on the electron energy. This is consistent with what was found in LEED surface studies.

(e) Dynamical effect

As the mean crystal size increases, dynamical considerations grow more important because of the multiple scattering processes and appreciable interactions among the scattered waves. The dynamical effect is particularly significant in electron diffraction because of strong coupling between electrons and materials.

Several experimental studies of the temperature dependence of dynamical electron diffraction intensities in thick polycrystalline metal films have been carried out by Niedrig et al. (1963-1970).²³⁻²⁵ Their polycrystalline films were tempered so that the crystal grain size was larger than the film thickness which was then taken as the mean crystal size. They observed a larger than expected increase in electron diffraction intensity²³ when the thick sample was cooled from room temperature to liquid helium temperatures, particularly in strongly scattering metals. They attributed this strong temperature dependence to anomalous transmission.²⁴⁻²⁶ Albrecht and Niedrig²⁵ found the experimental β value to be $1.3 \times 10^{-3} \text{ K}^{-1}$ for (220) order of a 25 nm thick gold film, about three times as large as the Debye value of $4.58 \times 10^{-4} \text{ K}^{-1}$. The apparent absorption arising from dynamical processes can thus alter the temperature dependence of diffraction intensity considerably.

The two-beam approximation for the dynamical theory in electron diffraction was used by Boersch, Jeschke, and Raith (BJR)²⁷ to investigate the

strong temperature effects, observed by Niedrig et. al.,²³⁻²⁵ which can not be explained with Debye's kinematic theory. It was assumed that there are only two strong beams excited, that is, the transmitted (primary) and one reflected beam, and they form a two-beam system. The anomalous absorption was derived by considering interactions in the two-beam system. The temperature dependence of the imaginary part of the electron atomic scattering factor gives rise to the anomalous absorption coefficient. It is defined similarly to the Borrmann effect²⁸ in X-ray diffraction. This anomalous absorption adds an extra term to the total absorption coefficient. The total absorption was defined as

$$\bar{\mu} = \mu_0'' - \mu_g''$$

A.1

Here, μ_0'' is the mean absorption coefficient, and μ_g'' is the anomalous absorption coefficient. The coefficient μ_g'' is temperature dependent and is reduced according to the Debye-Waller effect. The temperature dependence of the electron diffraction intensity was thus suggested to be associated with the temperature dependence of μ_g'' . The decrease in μ_g'' cause an increase in the total absorption $\bar{\mu}$ and enhances the temperature effect on the electron diffraction intensity.

In BJR's theory, it was assumed that some of the electron energy loss

was due to the absorption by the weakly excited beams (i. e. higher diffraction orders). This will contribute to the mean absorption coefficient since it was assumed that they do not scatter back into the two-beam system. This is likely to overestimate the mean absorption coefficient μ_0'' . For the case of thick perfect crystals, it was believed that the absorption due to weak-beam absorption may be less important,²⁹ so the mean absorption coefficient may be smaller in this case when compared to the crystal with defects, such as polycrystalline films. Therefore, the total absorption coefficient is then smaller than what BJR theory may predict since the contribution by the weak-beam absorption was not considered. This implies a smaller temperature factor β than the BJR value. Therefore, it is reasonable to believe that under the influence of the dynamical effect, the β value is larger than the value given with the simple Debye theory but is smaller than that derived from BJR theory. The essential condition for the anomalous absorption to be important is that the material thickness δ has to be larger than the anomalous absorption length ξ''_{hkl} . When this criterion is satisfied, the effective β value is larger than the Debye value and increases with film thickness until inelastic scattering³⁰ becomes dominant for extremely thick films.

References for Appendix A

1. R. D. Heidenreich, *J. Appl. Phys.* **20**, 993 (1949)
2. P. B. Hirsch, A. Kelly, and J. W. Menter, in: 1954 Proc. 3rd Int. Conf. Electron Microscopy (Roy. Mic. Soc., London 1956), p.231
3. P. B. Hirsch, R. W. Horne, and M. J. Whelan, *Phil. Mag.* **1**, 677 (1956)
4. R. Castaing, *Rev. Met.* **52**, 669 (1955)
5. P. M. Kelly and J. Nutting, *J. Inst. Metals* **87**, 385 (1959)
6. G. K. Williamson, *Proc. Roy. Soc.* **A257**, 457 (1960)
7. G. A. Bassett, J. W. Menter, and D. W. Pashley, *Soc.* **A246**, 345 (1958)
8. G. A. Bassett and D. W. Pashley, *J. Inst. Metals* **87**, 449 (1959)
9. D. W. Pashley, *Proc. Roy. Soc.* **A255**, 218 (1960)
10. L. Holland, *The Vacuum Deposition of Thin Films* (John Wiley & Sons, New York 1958), p.345
11. G. Thomas, *Transmission Electron Microscopy of Metals* (UC-Berkeley, 1966), p.174-178; also private communication with Professor R. W. Vook of The Department of Physics, and The Solid State Science and

Technology Program, Syracuse University.

12. R. V. Coleman and G. W. Sears, *Acta Met.* **5**, 131 (1957)
13. E. Suito and N. Uyeda, 1964 Proc. 3rd International Conference Electron Microscopy (Roy. Mic. Soc., London 1956), p.223
14. N. Takahashi and K. Mlhama, *Acta Met.* **5**, 159 (1957)
15. P. Duwez, R. H. Willens, and W. Clement, *J. Appl. Phys.* **31**, pp. 1136, 1137, 1500 (1960)
16. R. Weil and H. J. Read, *J. Appl. Phys.* **21**, 1068 (1950)
17. H. B. Haanstra, *Phillips Tech. Rev.* **17**, 178 (1955)
18. O. S. Heavens, *Thin Film Physics* (Methuen, London 1970), p.46

References for Appendix B

1. P. Debye, *Verh. Deut. Phys. Ges.* **15**, 678, 738, 857 (1913); *Ann. Phys.* **43**, 49 (1913-14)
2. I. Waller, *Z. Phys.* **17**, 398 (1923), **51**, 213 (1928); Dissertation, University of Uppsala (1925); *Ann. Phys.* **79**, 261 (1926)
3. H. Faxen, *Z. Phys.* **17**, 266 (1923); *Ann. Phys.* **54**, 615 (1918)
4. M. V. Laue, *Ann. Phys.* **42**, 1561 (1913); **81**, 877 (1926)
5. J. Laval, *C. R. Acad. Sci. Paris* **207**, 169 (1938), **208**, 1512 (1939)
6. H. P. Klug and L. E. Alexander, *X-ray Diffraction Procedures for Polycrystalline and Amorphous Materials*, 2nd ed. (John Wiley & Sons, New York 1974), pp144-148
7. L. Helmholtz, *J. Chem. Phys.* **4**, 316 (1936)
8. E. W. Hughes, *J. Am. Chem. Soc.* **63**, 1737 (1941)
9. E. W. Hughes and W. N. Lipscomb, *J. Am. Chem. Soc.* **68**, 1970 (1946)
10. I. Waller, *Ann. Phys.* **83**, 153 (1927)
11. C. Zener and S. Bilinsky, *Phys. Rev.* **50**, 101 (1936)

12. E. A. Owen and R. W. Williams, Proc. R. Soc. (London) **A188**, 509 (1947)
13. O. P. Gupta, J. of the Phys. Soc. Japan **52**, 4237 (1983)
14. Ph. Buffat, Solid State Comm. **23**, 547 (1977)
15. M. Blackman, Proc. Roy. Soc. **A148**, 365, 384 (1935), **A149**, 117, 126 (1935); Rep. Prog. Phys. **8**, 11 (1941)
16. M. Born and T. V. Karman, Physikal. Zert. **13**, 297 (1912), **14**, 15 (1913)
17. M. Kostelitz and J. L. Domange, Solid State Comm. **13**, 241 (1977)
18. A. MacRae and L. Germer, Phys. Rev. Lett. **8**, 489 (1962)
19. S. I. Kovalenko, N. V. Krainyukova, A. T. Pugachev, and N. P. Churakova, Sov. Phys. Crystallogr. **24**, 634 (1979)
20. V. N. Skokov, A. A. Dik, V. P. Koverda, and V. P. Skripov, Phys. Met. Metall. **56**, 125 (1983)
21. C. Solliard, Solid State Comm. **51**, 947 (1984)
22. C. Solliard, M. Flueli et J.-P. Borel, Acta Phys.-Helvetica **61**, 730 (1988)
23. H. Boersch, O. Bostanjoglo, and H. Niedrig, Z. Physik **180**, 407 (1964)

24. W. Glaeser and H. Niedrig, *J. Appl. Phys.* **37**, 4303 (1966)
25. W. Albrecht and H. Niedrig, *J. Appl. Phys.* **39**, 3166 (1968)
26. G. Jesehke and H. Niedrig, *Acta Cryst.* **A26**, 114 (1970)
27. H. Boersch, G. Jesehke, and H. Raith, *Z. Physik* **181**, 436 (1964)
28. G. Borrmann, *Z. Phys.* **127**, 297 (1950)
29. C. R. Hall and P. B. Hirsch, *Proc. R. Soc. (London)* **A286**, 158 (1964)
30. G. Hiller, T. Just, and H. Niedrig, *Phys. Lett.* **32A**, 262 (1970)